Extensions of Shallow Water Equations
Erweiterungen der Flachwassergleichungen

Vorgelegt von
Dipl.-Math. techn. Michael Hilden

Acknowledgments

Contents

Chapter 1

Introduction

1.1 Floods in Urban Areas

The task of the sewer system in urban areas is to collect waste water from houses and industries and to pipe it to purification plants in order to treat it and re-integrate it into the hydrological cycle. Furthermore, the sewer system drains surface water in case of rain events in order to protect streets and houses from flooding.

Figure 1.1: Flood problem in the spring 2000 at Kindsbach, close to the city of Kaiserslautern (Photo by G. Kries, also title photo of thesis)

During heavy rain events in the past years, sewer system were frequently overloaded and floods in the streets caused high damage. Figure 1.1 gives an

example of a flood problem in the spring of 2000 at Kindsbach near Kaiserslautern. Climate changes are expected to increase the occurrence of heavy rain events in our region. The current natural disasters in the catchment area of the river Elbe and in the south of France are tragic, but probably only first and sad examples of increasing problems caused by heavy rainfall.

The dimensions of the sewer system (e.g. diameter of sewer pipes) limit the drainage capacities and thus the flood protection potential. The actual procedure of dimensioning sewer systems computes the required diameters to drain the surface for specified rain events. The estimation of potential damage for higher rainfall is not included. The construction and the maintenance of sewer systems are important, but also expensive duties for communities. Since most sewer systems were built decades ago, there is a costly demand for modernization in the next years. These maintenance costs as well as the construction costs for new development areas increase with the dimensions of the system debiting communities. Since communities and its inhabitants are in particular interested in preventing serious damages caused by floods in urban areas, the optimal design approach should minimize the sum of construction and maintenance costs and of potential flood damages. The assessment of these potential flood damages depends on the relations between rain events, surface topography, sewer dimensioning and flood risks. Insurance agencies are also interested in such estimations to get a dependable base for calculating their contributions.

Mathematical modeling and numerical simulations of the involved water flow processes are applied to estimate these relations reliably. Usually, the flow processes in the sewer system and on the surface are handled separately: The free surface flow in the street is considered in a pure mass balance approach to approximate water inputs into the sewer system. The flow in the sewer system is modeled hydro-dynamically. In case of an overload of the sewer system, the flow of water on the surface is not simulated. Instead, the water from the sewer system is stored virtually together with the mass input terms of the mass balance surface model at the manhole and re-integrated into the system after the flood. This approach can indicate potential flood regions but due to the simple model approach on the surface, reliable evaluations of potential damages for the connected houses are not possible.

Extending this approach, it is possible to model the interaction of the water flow between sewer and surface within a coupled sewer-system surface-runoff approach. For that purpose, a hydro-dynamical model approach is applied also to the free surface flow in the street. The hydro-dynamical models for the sewer system and the free surface flow in the flood regions (i.e. streets) and the model approach for the drainage of water from catchment areas are coupled by exchange nodes as illustrated in Figure 1.2 (on the right).
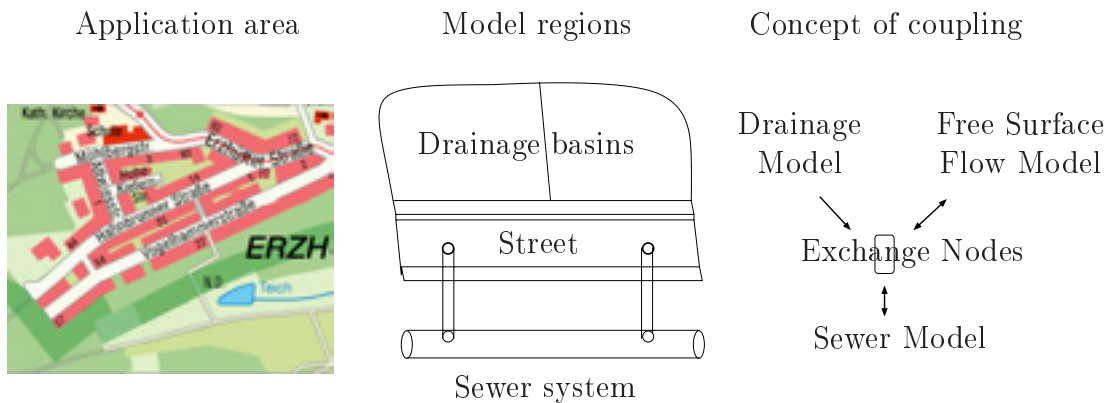
Figure 1.2: Example of an application area (map on the left), sketch of model regions (middle) and concept of model coupling (on the right)

Free surface flow of water within the simulation of flood events in streets can be modeled in different complex, but also computationally expensive ways from simple mass balances over Shallow Water Equations (SWE) up to Navier-Stokes Equations (NSE). Applying the 3D-NSE to flood simulations in computational domains with typical sizes of street sections (e.g. $40m \times 8m$) requires extremely high memory as well as CPU-times. Several calculations of flood scenarios with modified parameters for the purpose of optimization exceed present computer capacities. Therefore, the NSE approach cannot be applied practically to simulate the free surface flow in flood regions. In contrast, the SWE approach requires only fractions (factor $< 1/100$) of the computational efforts of the NSE, permitting practical application.

Since a dependable assessment of flood risks in urban areas requires reliable simulations, the accuracy of the SWE model approach is considered in detail. The task of this thesis is first to assess the accuracy of the SWE results for special flow problems typical for floods in urban areas, and second to derive suitable extensions of the SWE, thus increasing the accuracy of the results within reasonable computational effort.

1.2 Challenging Flow Problems *Manhole* and *Curb*

The 2D-SWE can be derived from the 3D-NSE by depth integration under the assumption of hydrostatic pressure distribution. They assume depth-averaged horizontal velocities but do not consider vertical velocities. Flood problems in urban areas, as illustrated in Figure 1.3, do not necessarily fulfill these assumptions und thus challenge the applicability of the SWE:
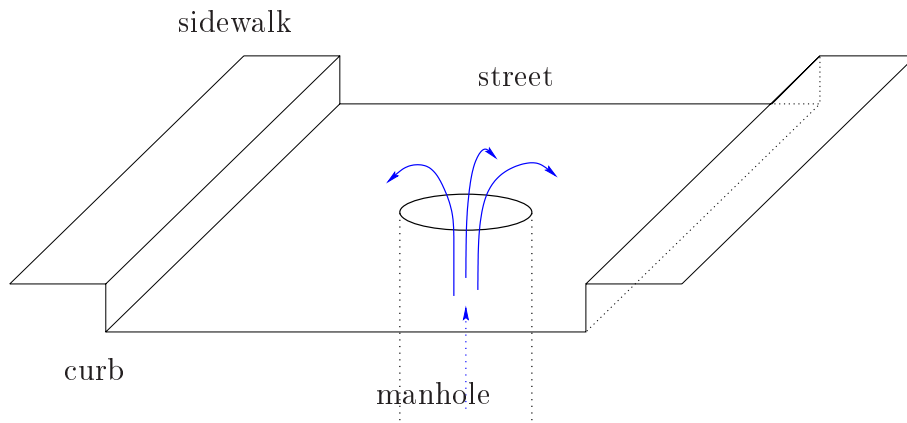
Figure 1.3: 3D-view of a typical flood problem in a street due to an overloaded sewer system
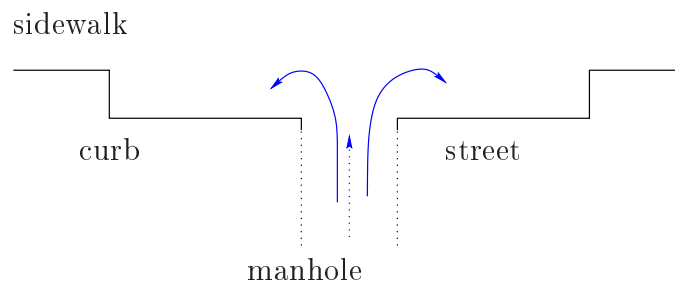
Figure 1.4: 2D-profile of a typical flood problem in a street due to an overloaded sewer system

When the sewer system is overloaded, water flows out of a manhole onto the street. Figure 1.3 demonstrates a 3D-view and Figure 1.4 a 2D-profile of this typical flood situation in a street. The applicability of the SWE is reviewed for two special flow problems involved in this flood situation:

1. The flow of water out of a manhole within the coupling of the flow in the sewer system and at the free surface due to an overload of the sewer system and

2. the flow over or against the curb of the sidewalk.

These two challenging flow problems are the starting point of this thesis and are denoted as the flow problems *manhole* (1.) and *curb* (2.).

The goal of this thesis is first to demonstrate the inaccuracy of the classical SWE for these flow problems and second to derive a new mathematical model, i.e. an extension of the SWE, describing the challenging flow problems accurately. In order to emphasize the difference to extended versions, the SWE are usually denoted as classical SWE.

1.3 Investigation of Literature

There exist enormous numbers of books and articles about NSE (e.g. [6], [13], [25], [42], [43], [53], [54]) and SWE (e.g. [1], [3],[35], [47], [51]) and about numerical schemes to solve them (e.g. [17], [18], [49], [26], [35] [51]), comparing numerical solution to analytic, or benchmark solutions for selected flow problems, e.g. driven cavity for NSE [12] or dam break problem for SWE [11].

The derivation of SWE within asymptotic expansions, depth integration and also heuristical approaches can be found in [3], [18], [19], [31], [16], [47].

The SWE are applied successfully to a wide range of applications, in particular in river hydraulics [1], [3], [35] [45], [51], but also in meteorology and for avalanche modeling [24].

In contrast to this high availability of literature for derivations, numerical schemes and applications of the classical SWE, works questioning the applicability of SWE for selected flow problems and seeking for extensions are rare in literature. Näf [31] included vertical velocities in the SWE yielding a set of 8 equations (most of them are PDE) for the 1D-SWE and a set of 10 equations for the 2D-SWE. But the numerical results, tested on the dam break problem on a coarse FEM grid are not convincing and suffer from oscillations.

Haasenritter [18] considered the flow problem *curb* as the flow over an obstacle in her diploma thesis and proposed an extension in the numerical treatment of the flux estimation at the curb.

Plenty of articles were found that treat the problem of obstacles in flows, but most of them in a closed channel [8], [44], [55], and some for free surface flows [15], [22], [34]. They are either derived for NSE, for potential flow, or they consider special numerical techniques to solve the classical SWE without any extensions that involve e.g. vertical velocities.

The demand for simulation of such flow problems within the flood risk assessment in urban areas on the one hand and the lack of research in this field on the other hand inspired this thesis.

1.4   Outline of the Thesis

The thesis is divided into two main parts:

In the first part, the Navier-Stokes Equations (NSE), the Euler Equations and the classical Shallow Water Equations (SWE) are presented as existing model approaches for the free surface flow of water in Chapter 2. The comparison of analytical solutions of the Euler Equations, numerical NSE solutions and SWE results for the challenging flow problems *manhole* and *curb*, introduced in Section 1.2, shows differences questioning the reliable applicability of the classical SWE for the considered flow problems in Chapter 3.

Thus, suitable extensions of the SWE are derived in the second part of the thesis and their results are compared to the NSE benchmark solutions. The Extension *Vortex Separation* introduces a fluid bottom layer as a separated vortex region defining a new bottom level for the main flow domain in Chapter 4. Approximations of vertical velocities yield the Extension *Pressure Correction* in Chapter 5, entailing additional terms in the momentum equation of the SWE.

The differences between NSE and the extended SWE are decreased. Thus, the developed extensions allow a more reliable simulation of the flow problems. The increased accuracy of results is achieved by moderate additional computational effort still requiring only fractions of the CPU times of the NSE solution.

Since the extensions are derived only for the 1D-SWE in Chapter 4 and 5, Chapter 6 presents the extensions also for the 2D-SWE.

Finally, Chapter 7 offers conclusions and an outlook to further work connected with the problems.

Since the Extension *Vortex Separation* of Chapter 4 and in particular the Extension *Pressure Correction* of Chapter 5 are based on modified assumptions in the derivation of the SWE, we present two derivations in detail in Chapter

2. Notations and some mathematical and physical background are excluded from the thesis into Appendix A.

Appendix B, containing portraits and data of famous mathematicians involved in the derivation of the mathematical background of the equations of motion in fluid dynamics, close out the appendix and the thesis. In particular the biography of Jean Claude de Saint-Venant is included since he was deeply involved in the derivation of the theoretical background.

Chapter 2

Models for Free Surface Flow of Water

The flow of water has always caused amazement in various fields of interest, reaching from the basic need of drinking water in order to survive over engineering and political questions of water transport and distribution, sustainable development of water resources up to fine arts. ¿From the physical point of view, the flow of the liquid water is described by conservation laws for mass, momentum and energy. These conservation laws are expressed mathematically as Partial Differential Equations (PDE). Most of the foundations of the mathematical models were derived already in the 19th century and earlier. The equations are often named in memory of their inventors, e.g. Newton, Euler, Navier, de Saint-Venant, Stokes or Reynolds. Appendix B provides further information about those mathematicians.

Due to the increase of powerful computer capacities and in particular due to the development of modern numerical solvers for PDE, many improvements were obtained in the last two decades in the field of Computational Fluid Dynamics (CFD). It is today possible to simulate fluid flow for many applications.

2.1 Mathematical Modeling

Historical Remark 2.1 *Galileo Galilei (born 1564 in Pisa, died 1642 in Arcetri, Florence) already mentioned that*
"the book of nature is written in the language of mathematics. "

In fact, mathematical modeling and in particular nowadays its numerical implementations are capable of describing physical properties for the simulation of processes. These simulations allow to understand processes in detail, sparking ideas for modifications and optimizations of the processes (e.g. in
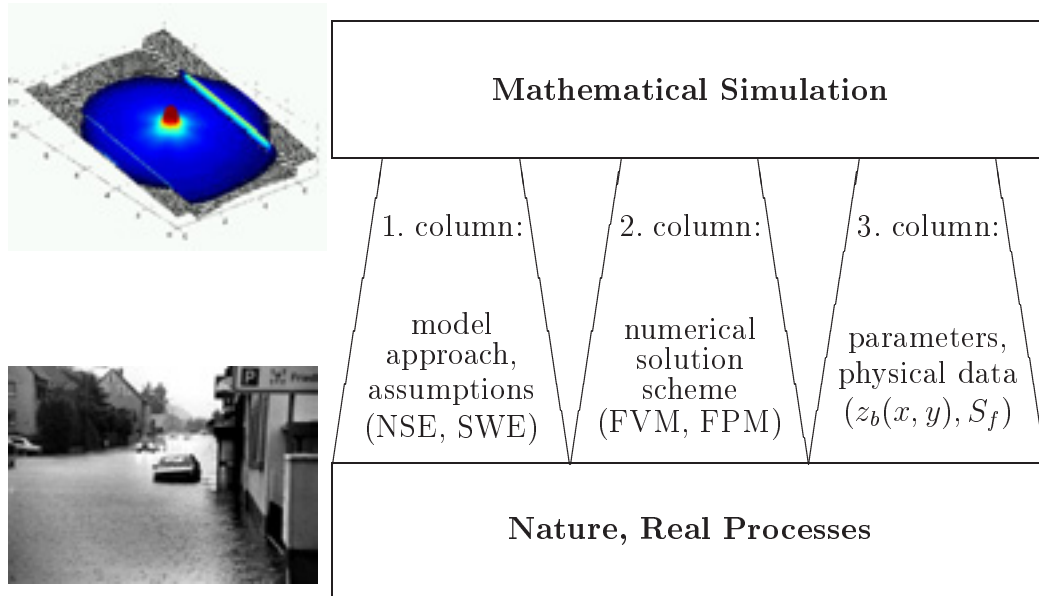
Figure 2.1: Columns of mathematical simulation: 1. mathematical modeling, 2. numerical scheme and 3. data and parameters. Example of real flood process and a mathematical simulation on the left hand side

industry) and yielding the economical prediction of processes in different scenarios. Thus, mathematical modeling is a sustainable key technology with growing importance.

The mathematical simulation of a process is usually based on the three columns as illustrated in Figure 2.1, where examples for the free surface flow of water are given in brackets:

1. mathematical model approach with its assumptions,

2. numerical solution scheme with its implementation and

3. parameters and physical data.

Departing from simplifying assumptions (e.g. water is incompressible), the model equations are derived. In fluid dynamics, these are usually conservation laws. There exist different model approaches varying in complexity and posed assumptions. This variability, indicated by the varying width of the 1.column of the figure, occurs also in the other columns, given e.g. by the choice of the numerical solution scheme or the grid resolution.

Explanation 2.2 *The first two columns for fluid flow are very general columns and the model approach and the numerical solution scheme are applicable to*

*many different flow problems. ¿From the mathematical point of view, the sim-
ulation of water flow in a river, oil flow in a pipe, break fluid in a tube or urine
flow in a diaper are similar. This generality of mathematical modeling implies
ingenuity.*

The application to a real problem requires data, e.g. the bottom elevation
$z_b(x,y)$ with different spatial resolutions. Depending on the choice of the
model, further parameters (e.g. bottom friction) are required. The left side
of Figure 2.1 gives an example for a real flood process and a mathematical
simulation of the process.

Explanation 2.3 *In this thesis, numerical results of different model approaches
are compared. Since the numerical schemes were applied already successfully,
differences in the results are effected by the choice of the model approach. Con-
centrating on the first column in Figure 2.1, the major purpose of the thesis
is the proper mathematical modeling of the free surface flow of water within
reasonable computational effort in order to enable the reliable application to
large flow problems.*

2.2 Overview over Model Approaches

The model approaches for the simulation of free surface flow of water are
introduced in the next sections of this chapter and summarized in Figure 2.2.
The most general equations of motion for free surface flow of the liquid water
are the 3D-Navier-Stokes Equations (3D-NSE). Assuming a channel of infinite
width, yields the neglect of the y-dimension and simplifies the 3D-NSE for the
real 3D flow problems (left hand side) to the 2D-NSE (right hand side) in a
2D-profile of the flow problems. Considering only these two dimensions x and
z, the horizontal velocity $v = 0$ and all y-derivatives $\partial/\partial y = 0$ are neglected.

Explanation 2.4 *The incompressible Euler Equations are the in-viscid NSE.
Instead of deriving the SWE from the NSE, we demonstrate their derivation
from the Euler Equations and obtain their frictionless form. The friction is
added in a separate section due to viscous considerations by an empirical ap-
proach. That derivation is chosen since the friction is small for the consid-
ered flow problems and an empirical friction parameter is required even in the
derivation from the NSE.*

The derivation of the Shallow Water Equations (SWE) departs from the
Euler Equations and the assumption of hydrostatic pressure p_{hy}. This sim-
plifies the 3D-NSE to the 3D-SWE and the 2D-NSE to the 2D-vertical-SWE
respectively. The integration over the water depth $h = H - z_b$ yields the
2D-SWE and the 1D-SWE respectively.
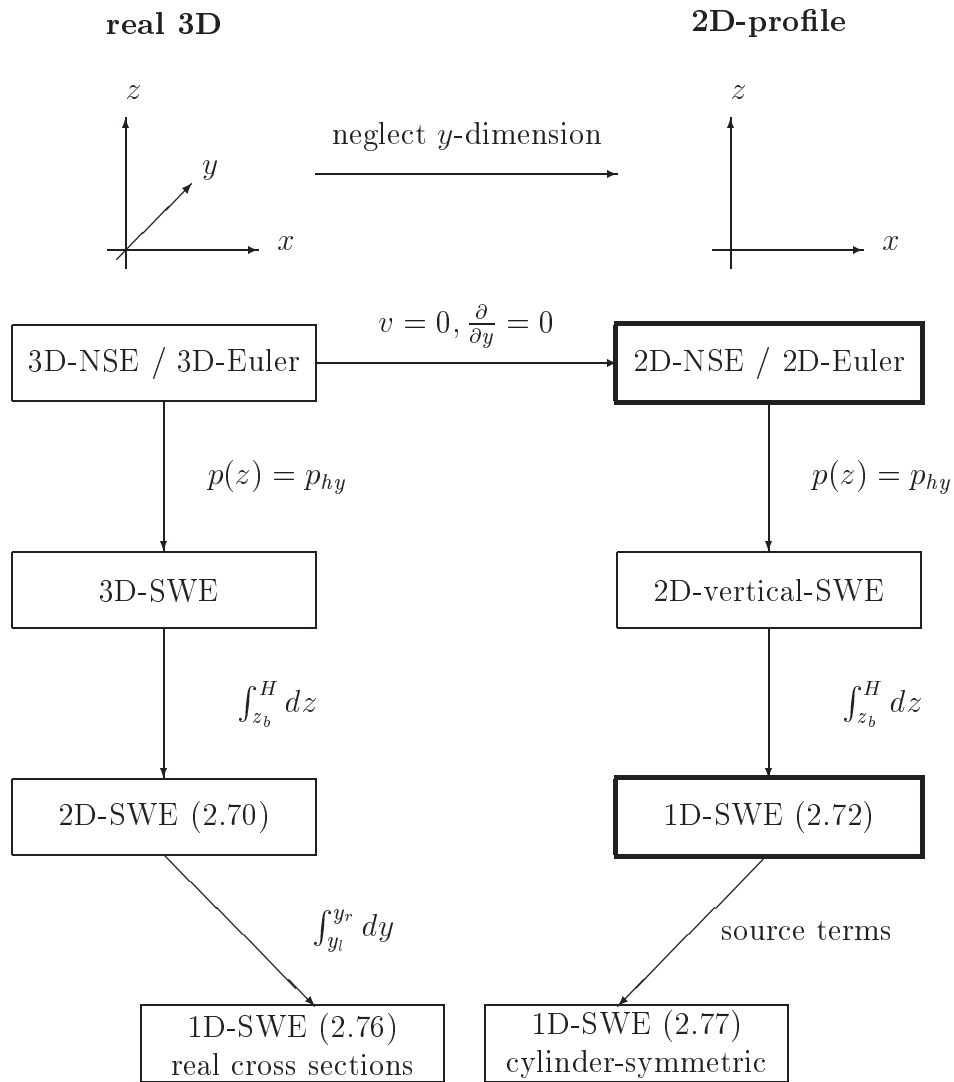
Figure 2.2: Overview of model approaches and their derivation for free surface flow of water in real 3D (left hand side) and simplified 2D-profile where the y-dimension is neglected (right hand side). Avoiding high computational effort, the results of the NSE (benchmark) and classical SWE model approaches are compared in the 2D-profile in Chapter 3.

Remark 2.5 *The 2D-SWE denote the depth integrated 2D-equations in the x-y plane. The considered flow problems in 2D-profiles in the x-z plane are solved by the 2D-NSE and the 2D-vertical-SWE.*

The 1D-SWE exist in different formulations: (2.72) for profiles, identical to infinite or rectangular channels, (2.76) for the application to natural rivers with real cross sections A. These cross sections A are given by the natural profile of the river bed and depend on the water level h causing additional terms in the 1D-SWE. Finally, there exist the cylinder-symmetrical formulation (2.77) with additional source terms.

The last section of this chapter presents the applied numerical solution schemes for these model approaches. Following Explanation 2.3, Section 2.5 is only an overview since the focus of the thesis is located on mathematical modeling.

2.3 Navier-Stokes Equations (NSE)

Historical Remark 2.6 *The Navier-Stokes Equations (NSE) were first derived by Claude Louis Marie Henri Navier (see Appendix B.1) in 1821. Not fully understanding all about shear stress in a fluid, he found the proper equations nevertheless.*

Although Adhémar Jean Claude Barré de Saint-Venant (see Appendix B.2) derived the equations properly in 1842, the NSE were named in memory of Navier and of George Gabriel Stokes (see Appendix B.1), who showed them independently two years later in 1844.

2.3.1 Model Assumptions

Remark 2.7 *To avoid misunderstandings, the applied notations are summarized in Appendix A.1. Some theoretical background for conservation laws is provided in Appendix A.2 and details concerning viscous flow behavior are presented in Appendix A.4.*

Figure 2.3 illustrates the notations for the free surface flow over a fixed bottom with $z_b(x, y)$ as elevation above datum. The free water surface is denoted with $H(x, y)$. The water depth is given by $h(x, y) = H(x, y) - z_b(x, y)$. The pressure at the free surface is assumed to be the constant atmospheric pressure $p_H(x, y) = p_H$ for the entire computational domain. Forces due to earth rotation (Coriolis force) or wind stresses on the water surface are neglected.

The density is a scalar field $\rho(\vec{x})$ and for the incompressible fluid water, $\rho(\vec{x}) = \rho = const$ is assumed for all points $\vec{x}$ in the fluid domain Ω. The
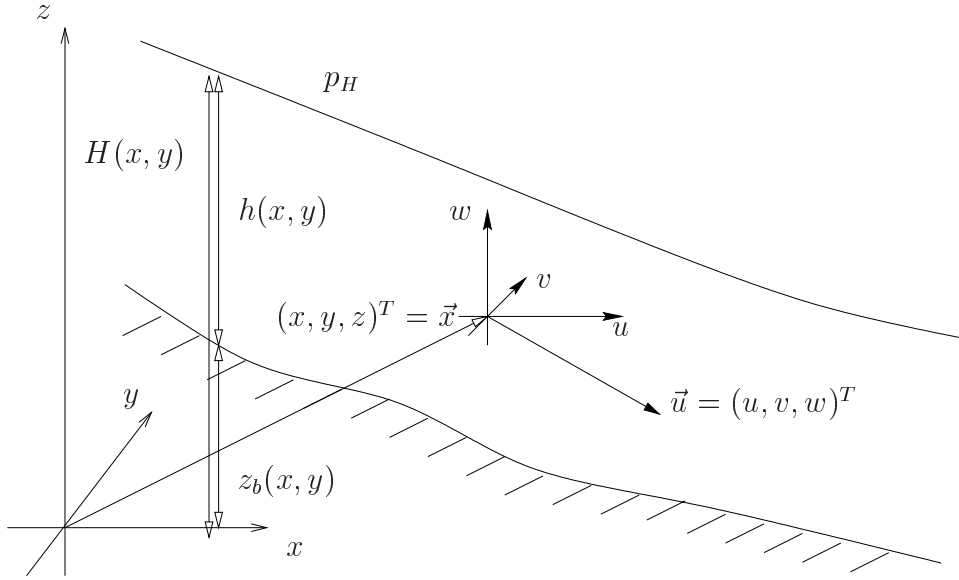
Figure 2.3: Sketch of fluid domain with bottom elevation $z_b(x, y)$ and free surface water level $H(x, y)$ and further notations

pressure $p(\vec{x})$ is assumed to be a differentiable scalar field in the fluid domain. The velocity field is a vector field $\vec{u}(\vec{x}) = (u, v, w)^T$ that is assumed to be differentiable and defines the motion of the fluid and the fluid domain $\Omega(t)$. The fluid domain is assumed to remain always simply connected, no drops of water are considered. Further assumptions for the boundary conditions (e.g free-slip or no-slip conditions) are given in Section 2.3.5.

Since water is assumed to be incompressible, we always mean the incompressible NSE and incompressible Euler Equations when dealing with NSE and Euler Equations respectively. Incompressible fluids are assumed to have a constant density, $\rho = const$. The notation 'incompressible' is slightly misleading since $\rho = const$ is in fact density conservative and thus not only incompressible but also independent of temperature effects. Assuming constant density ρ, temperature variations that usually affect the density and require the involvement of the conservation of energy are not considered in the equations of motion. Conservation of mass and momentum in 3 directions yields 4 equations for the 4 unknowns p and $\vec{u} = (u, v, w)^T$. For the simulation of free surface flow, further conditions for the determination of the free surface H are required as presented in Section 2.3.5.

Since several derivations of the NSE exist in literature (e.g. [6], [13] [38], [53], [54]), we demonstrate some basics of the derivation of the equations and

refer to literature for the details. Some theoretical background for conservation laws is presented in Appendix A.2.

2.3.2 Mass Conservation

The mass conservation in 3D reads

$$0 = \frac{d}{dt} \int\limits_{\Omega(t)} \rho \, dV = \int\limits_{\Omega(t)} \frac{\partial}{\partial t}\rho + div(\rho\vec{u}) \, dV.$$

For $\rho = const$ this equation is simplified to $0 = \int_{\Omega(t)} div(\vec{u}) \, dV$ holding for any choice of $\Omega(t)$ and thus yielding

$$div \, \vec{u} = \frac{\partial u}{\partial x} + \frac{\partial v}{\partial y} + \frac{\partial w}{\partial z} = 0. \tag{2.1}$$

For incompressible fluids, the mass conservation is identical to a volume conservation described by the continuity equation (2.1).

2.3.3 Momentum Conservation

Due to Newton's 2nd law of motion, generally known as $\vec{F} = m\vec{a}$, forces change the momentum due to acceleration. Denoting forces per unit mass with $\vec{f}$, Newton's law is re-written as

$$\vec{a} = \frac{d}{dt} \, \vec{u} = \dot{\vec{u}} = \vec{f}. \tag{2.2}$$

The equations of motion based on Newton's law (2.2) depend on the evaluation of the force on the right hand side. For special flow behaviors, dominant forces are selected and other forces are neglected, as summarized in Table 2.1 taken from [53].

flow behavior	$\vec{a} = \vec{f}$	Newton
hydrostatic	$\vec{0} = \vec{f_G} + \vec{f_P}$	Euler
in-viscid	$\vec{a} = \vec{f_G} + \vec{f_P}$	Euler, Bernoulli
viscid	$\vec{a} = \vec{f_G} + \vec{f_P} + \vec{f_V}$	Navier, Stokes
viscid, creeping	$\vec{0} = \vec{f_G} + \vec{f_P} + \vec{f_V}$	Stokes, Oseen

Table 2.1: Consideration of forces for different flow behaviors and the mathematicians involved in the derivation of the resulting equations of motion

Three forces are considered for the viscous, incompressible flow description with NSE:

- force due to earth gravitation $(\vec{f}_G = \vec{g} = (0, 0, -g)^T)$,

- force due to the pressure gradient $(\vec{f}_P = -1/\rho \ grad \ p)$ and

- friction force due to viscosity $(\vec{f}_V = 1/\rho \ div \ \boldsymbol{\tau} = \nu \Delta \vec{u})$

with the viscous friction (A.22) for Newtonian Fluids (A.21).

Historical Remark 2.8 *The names of the mathematicians involved in the derivation of the resulting equations of motion that were named in their memory are given also in Table 2.1. Further historical remarks are provided in Appendix B.*

Inserting the material derivative of the velocity $d/dt \ \vec{u} = \partial/\partial t \ \vec{u} + (\vec{u} \cdot grad)\vec{u}$ from (A.7) into (2.2) and considering the forces due to pressure, viscous friction and gravity yields the incompressible 3D-Navier-Stokes Equations (3D-NSE), describing the conservation of mass and momentum (2.3) in 3D with the variables and parameters listed in Table 2.2.

$$
\begin{aligned}
div \ \vec{u} &= 0, \\
\frac{\partial}{\partial t}\vec{u} + (\vec{u} \cdot grad) \ \vec{u} &= -\frac{1}{\rho} \ grad \ p + \nu \Delta \vec{u} + \vec{g}.
\end{aligned}
\tag{2.3}
$$

$\vec{u}$: velocity vector

p : pressure

ρ : constant density

ν : kinematic viscosity

$\vec{g}$: external force (i.e. gravity)

Table 2.2: Variables and parameters in the NSE

Particular solutions of the 3D-NSE can be obtained from the 2D-NSE. Assuming a channel of infinite width and no influence of the y-dimension allows to neglect this dimension. This is considering the flow in a 2D-profile across the channel and allows the simplification of the NSE to 2D. The problem in 2D is considered in the variables x, z and the velocities u, w (see Figure 2.2, right hand side).

2.3.4   Incompressible 3D-Euler Equations

The viscosity ν of water is very small $\nu = 10^{-6} m^2/s$ (see Remark A.13). Neglecting the viscous friction term $\nu \Delta \vec{u}$ in the 3D-NSE yields the incompressible 3D-Euler Equations. Since we present the derivation of the homogeneous SWE departing from these equations we present them in detailed form:

$$
\begin{aligned}
\frac{\partial}{\partial x} u + \frac{\partial}{\partial y} v + \frac{\partial}{\partial z} w &= 0, \\
\frac{\partial}{\partial t} u + u \frac{\partial}{\partial x} u + v \frac{\partial}{\partial y} u + w \frac{\partial}{\partial z} u &= -\frac{1}{\rho} \frac{\partial}{\partial x} p, \\
\frac{\partial}{\partial t} v + u \frac{\partial}{\partial x} v + v \frac{\partial}{\partial y} v + w \frac{\partial}{\partial z} v &= -\frac{1}{\rho} \frac{\partial}{\partial y} p, \\
\frac{\partial}{\partial t} w + u \frac{\partial}{\partial x} w + v \frac{\partial}{\partial y} w + w \frac{\partial}{\partial z} w &= -\frac{1}{\rho} \frac{\partial}{\partial z} p - g.
\end{aligned}
\tag{2.4}
$$

2.3.5   Boundary Conditions for Free Surface Flow

The equations of motion are PDE. Appropriate boundary conditions at the bottom and at the free surface are required to solve the PDE uniquely.

Kinematic Boundary Conditions usually assume no penetration of water into the ground or into the air. The condition of no flux through the fixed bottom is fulfilled by the so called free-slip condition

$$
\vec{n}_b \cdot \vec{u} = 0,
\tag{2.5}
$$

where $\vec{n}$ is the normal vector at the bottom. Since the normal velocity component is prescribed to be zero, the velocity is tangential to the ground and the condition is named 'free-slip' condition.

In case of a source of water at the ground, e.g. caused by an inflow of water from a manhole, the flux through the ground is given as the normal component of the inflow velocity q. (2.5) is thus extended to

$$
\vec{n}_b \cdot \vec{u} = q,
\tag{2.6}
$$

q has the dimension of a velocity and yields -integrated over an area- a volume flow in m^3/s.

The normal vector $\vec{n}_b$ at the ground is given via derivatives of the bottom elevation $z_b(x, y)$ as presented in Figure 2.4 by

$$
\vec{n}_b = \begin{pmatrix} -\frac{\partial z_b}{\partial x} \\ -\frac{\partial z_b}{\partial y} \\ 1 \end{pmatrix}.
\tag{2.7}
$$
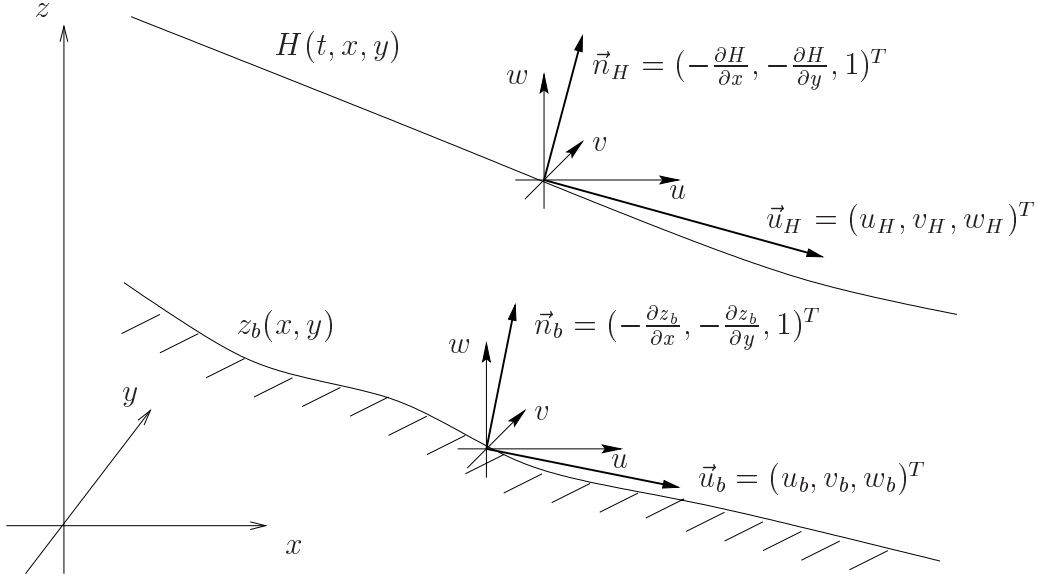
Figure 2.4: Illustration of free slip conditions at the free surface $H(t, x, y)$ and the bottom $z_b(x, y)$

Similarly as (2.5) is extended for an inflow of water from the ground to (2.6), the free-slip condition for the free surface has to be extended by the possible temporal changes of this interface. Any flux through the free surface H yields obviously a change of the position of the free surface in time

$$\vec{n}_H \cdot \vec{u} = \frac{\partial H}{\partial t}. \tag{2.8}$$

The normal vector $\vec{n}_H$ at the free surface is also given via derivatives of the free surface $H(t, x, y)$ as presented in Figure 2.4 by

$$\vec{n}_H = \begin{pmatrix} -\frac{\partial H}{\partial x} \\ -\frac{\partial H}{\partial y} \\ 1 \end{pmatrix}. \tag{2.9}$$

Figure 2.4 illustrates the free slip conditions at the free surface $H(x, y)$ and the bottom $z_b(x, y)$, finally yielding

$$w_H = \frac{\partial H}{\partial t} + u_H \frac{\partial H}{\partial x} + v_H \frac{\partial H}{\partial y}, \tag{2.10}$$

$$w_b = u_b \frac{\partial z_b}{\partial x} + v_b \frac{\partial z_b}{\partial y} + q. \tag{2.11}$$

These kinematic boundary conditions are appropriate for the frictionless Euler Equations (2.4) requiring only one boundary condition at the bottom and the

surface to be solvable uniquely.

The NSE are second order PDE due to the viscous term from (A.21). In addition to the kinematic boundary conditions sufficient for the Euler Equations, the NSE require further conditions for well-posedness.

Dynamic Boundary Conditions require further restrictions for the flow velocity or the pressure usually based on assumptions for forces. The viscous fluid is assumed not to move at the fixed bottom z_b. Thus the velocity at the bottom has to be zero as required by the no-slip condition

$$\vec{u} = \vec{0}. \tag{2.12}$$

Explanation 2.9 *The no-slip condition $\vec{u} = \vec{0}$ at the bottom for the fluid water with small viscosity ν usually results in a small viscid bottom layer. For free surface flow of viscous fluids over a plane wall, the size of this layer depends on the Reynolds-number Re from Definition A.15 with $1/\sqrt{Re}$. For water with $\nu = 10-6m^2/s$ and typical depth $h = 0.1m$ and velocity $u = 1m/s$, we obtain*

$$Re = \frac{uh}{\nu} \approx 10^5 \tag{2.13}$$

and thus a small bottom layer. Instead for the very viscid fluid oil, this layer can be large.

Historical Remark 2.10 *Nevertheless, the occurrence of this layer is important for the understanding of friction in viscid fluids. Prandtl [38] introduced this boundary layer theory and closed the gap between experiments and calculations for viscid fluids.*

The continuity of total stress $\boldsymbol{\tau} - p/\rho\boldsymbol{Id}$ at the free surface between the fluid and the air is assumed. We denote the jump between the values in water and air in normal direction $\vec{n}_H$ of the free surface H as $[\vec{n}_H^T(\boldsymbol{\tau} - p/\rho\boldsymbol{Id})]$. Continuity is given, if the inner product of this jump and the normal vector $\vec{n}_H$ vanishes

$$[\vec{n}_H^T(\boldsymbol{\tau} - \frac{p}{\rho}\boldsymbol{Id})] \cdot \vec{n}_H = 0. \tag{2.14}$$

Remark 2.11 *As presented in [16], it is possible to introduce a further equation for the free surface description using a function Ψ with the value one inside the fluid ($\Psi(x, y, z) = 1$ for $z_b(x, y) \leq z \leq H(x, y)$) and zero outside. Solving the transport equation of this function yields the description of the free surface. The applied numerical scheme for the NSE of Section 2.5.1 is a mesh-free particle method and contains this description automatically.*

2.4   Classical Shallow Water Equations (SWE)

Since numerical solutions of the 3D-NSE for large scale problems require high computational effort, simplifications were derived and applied to various flow problems. The flow of water in rivers, e.g. the Rhine river with more than 1000 km length, some 100 meters width and only a few meters depth, is usually dominated by the length scale. The width and in particular the depth dimensions are less important. The 2D-SWE and 1D-SWE require less computational effort than the NSE and are applied successfully to many river flow problems, e.g. to the operational water level prediction in the Rhine river [45].

There exist already presentations of the derivation of the SWE from the NSE in literature [47], [16], [18]. In oder to have a base for the derivation of extensions of the SWE, we present two derivations of the 2D-SWE in this thesis:

An asymptotic expansion of the 3D-Euler Equations for the small ratio between depth and length scales yields the frictionless 2D-SWE in Section 2.4.1. Assuming a hydrostatic pressure distribution, these equations are derived independently of any asymptotic in Section 2.4.2 by depth integration of the 3D-Euler equations.

Historical Remark 2.12 *In the French scientific community the SWE are named Saint-Venant equations in memorial of Adhémar Jean Claude Barré de Saint-Venant (see Appendix B.2).*

2.4.1   Derivation of SWE via Asymptotic Expansion

The asymptotic expansion presented in [47], [18] is based on a sufficiently small proportion between the typical depth and length scales of the water flow. We consider the incompressible Euler Equations (2.4)) with gravity force $-g$ in z-direction. Let the typical depth scale d be small compared to the horizontal length scales $k \gg d$. Rescaling the variables with these typical scales yields dimensionless independent variables $\hat{x}, \hat{y}, \hat{z}$

$$\hat{x} = \frac{1}{k}x, \qquad \hat{y} = \frac{1}{k}y, \qquad \hat{z} = \frac{1}{d}z. \qquad (2.15)$$

A scaling of time and velocity is also required to rescale the whole Euler Equations.

Definition 2.13 $c = \sqrt{gh}$ *is defined as characteristic velocity for free surface flow of water with water depth h.*

c is the typical travel velocity of a small disturbance (e.g. waves generated by a stone thrown into a lake) in the free surface of standing water with water

depth h. It can be understood as a kind of speed of sound for surface waves. Assuming $c = \sqrt{gh}$ to be the typical horizontal flow velocity, we apply $\sqrt{gd}$ as the typical scale of the horizontal velocity to rescale the velocities u and v.

$$\hat{u} = \frac{1}{\sqrt{gd}}u, \qquad \hat{v} = \frac{1}{\sqrt{gd}}v. \tag{2.16}$$

To be consistent, we rescale the time appropriately by the quotient of the scaling factors of velocity and length dimension

$$\hat{t} = \frac{\sqrt{gd}}{k}t, \tag{2.17}$$

yielding the following scaling for the vertical velocity

$$\hat{w} = \frac{d}{k\sqrt{gd}}w. \tag{2.18}$$

Since we rescaled the vertical dimension with $1/d$ we proceed similar with the water level and the water depth

$$\hat{H} = \frac{1}{d}H, \qquad \hat{h} = \frac{1}{d}h. \tag{2.19}$$

The scaling of the energy is given by the square of the velocity scaling and this yields the appropriate scaling for the pressure

$$\hat{p} = \frac{1}{\rho gd}p. \tag{2.20}$$

We rewrite the Euler Equations (2.4) in the rescaled variables by extracting the scaling factors, e.g.

$$\frac{\partial u}{\partial x} = \frac{\partial \sqrt{gd}\frac{1}{\sqrt{gd}}u}{\partial k\frac{1}{k}x} = \frac{\partial \sqrt{gd}}{\partial k}\frac{\hat{u}}{\hat{x}} = \frac{\sqrt{gd}}{k}\frac{\partial \hat{u}}{\partial \hat{x}}. \tag{2.21}$$

or

$$\frac{\partial w}{\partial z} = \frac{\partial \frac{k\sqrt{gd}}{d}\frac{d}{k\sqrt{gd}}w}{\partial d\frac{1}{d}z} = \frac{\partial \frac{k\sqrt{gd}}{d}}{\partial d}\frac{\hat{w}}{\hat{z}} = \frac{k\sqrt{gd}}{d^2}\frac{\partial \hat{w}}{\partial \hat{z}} \tag{2.22}$$

Dividing by $\sqrt{gd}$ and multiplying with $\frac{d^2}{k}$ yields the mass conservation equation in rescaled variables:

$$\frac{d^2}{k^2}\left(\frac{\partial \hat{u}}{\partial \hat{x}} + \frac{\partial \hat{v}}{\partial \hat{y}}\right) + \frac{\partial \hat{w}}{\partial \hat{z}} = 0. \tag{2.23}$$

Introducing the small parameter

$$\epsilon = \frac{d^2}{k^2} \ll 1, \tag{2.24}$$

the 3D-Euler Equations are re-written separated in orders of ϵ. For the sake of simplicity, the hats (e.g. $u = \hat{u}$) are omitted, yielding:

$$\epsilon \quad (\frac{\partial u}{\partial x} + \frac{\partial v}{\partial y}) \quad + \quad \frac{\partial w}{\partial z} = 0 \qquad (2.25)$$

$$\epsilon \quad (\frac{\partial u}{\partial t} + u\frac{\partial u}{\partial x} + v\frac{\partial u}{\partial y} + \frac{\partial p}{\partial x}) \quad + \quad w\frac{\partial u}{\partial z} = 0 \qquad (2.26)$$

$$\epsilon \quad (\frac{\partial v}{\partial t} + u\frac{\partial v}{\partial x} + v\frac{\partial v}{\partial y} + \frac{\partial p}{\partial y}) \quad + \quad w\frac{\partial v}{\partial z} = 0 \qquad (2.27)$$

$$\epsilon \quad (\frac{\partial w}{\partial t} + u\frac{\partial w}{\partial x} + v\frac{\partial w}{\partial y} + \frac{\partial p}{\partial z} + 1) \quad + \quad w\frac{\partial w}{\partial z} = 0 \qquad (2.28)$$

The kinematic boundary conditions at the free surface H and the bottom z_b read in rescaled variables

$$\epsilon \quad (\frac{\partial H}{\partial t} + u\frac{\partial H}{\partial x} + v\frac{\partial H}{\partial y}) \quad = \quad w \quad \text{at} \quad z = H, \qquad (2.29)$$

$$\epsilon \quad (u\frac{\partial z_b}{\partial x} + v\frac{\partial z_b}{\partial y}) \quad = \quad w \quad \text{at} \quad z = z_b. \qquad (2.30)$$

Within the asymptotic expansion, the dependent variables are developped in series of ϵ:

$$u \quad = \quad u^{(0)} + \epsilon u^{(1)} + \epsilon^2 u^{(2)} + \cdots, \qquad (2.31)$$

$$v \quad = \quad v^{(0)} + \epsilon v^{(1)} + \epsilon^2 v^{(2)} + \cdots, \qquad (2.32)$$

$$w \quad = \quad w^{(0)} + \epsilon w^{(1)} + \epsilon^2 w^{(2)} + \cdots, \qquad (2.33)$$

$$H \quad = \quad H^{(0)} + \epsilon H^{(1)} + \epsilon^2 H^{(2)} + \cdots, \qquad (2.34)$$

$$p \quad = \quad p^{(0)} + \epsilon p^{(1)} + \epsilon^2 p^{(2)} + \cdots. \qquad (2.35)$$

Inserting these series into the rescaled Euler Equations yields terms of different orders of ϵ in every conservation equation and in the boundary conditions. Since we assume ϵ to be small, the equations contain terms of different scales. Thus we separate the different orders of epsilon in the rescaled Euler Equations to own equations of the different orders. We concentrate first on the terms without ϵ, i.e. the zeroth order equations:

$$\frac{\partial w^{(0)}}{\partial z} = 0, \qquad (2.36)$$

$$w^{(0)}\frac{\partial u^{(0)}}{\partial z} = 0, \qquad (2.37)$$

$$w^{(0)}\frac{\partial v^{(0)}}{\partial z} = 0, \qquad (2.38)$$

$$w^{(0)}\frac{\partial w^{(0)}}{\partial z} = 0. \qquad (2.39)$$

Due to (2.36), $w^{(0)}(z)$ is constant over the water depth. This holds also for $u^{(0)}(z)$ and for $v^{(0)}(z)$. The zeroth order equations of the boundary conditions yield $w^{(0)}(H) = w^{(0)}(z_b) = 0$ and thus

$$w^{(0)} = 0, \tag{2.40}$$

$$u^{(0)} = u^{(0)}(t, x, y), \tag{2.41}$$

$$v^{(0)} = v^{(0)}(t, x, y). \tag{2.42}$$

The first order equations of the asymptotic expansion read

$$\frac{\partial u^{(0)}}{\partial x} + \frac{\partial w^{(1)}(z_b) v^{(0)}}{\partial y} + \frac{\partial w^{(1)}}{\partial z} = 0, \tag{2.43}$$

$$\frac{\partial u^{(0)}}{\partial t} + u^{(0)} \frac{\partial u^{(0)}}{\partial x} + v^{(0)} \frac{\partial u^{(0)}}{\partial y} + \frac{\partial p^{(0)}}{\partial x} = 0, \tag{2.44}$$

$$\frac{\partial v^{(0)}}{\partial t} + u^{(0)} \frac{\partial v^{(0)}}{\partial x} + v^{(0)} \frac{\partial v^{(0)}}{\partial y} + \frac{\partial p^{(0)}}{\partial y} = 0, \tag{2.45}$$

$$\frac{\partial p^{(0)}}{\partial z} + 1 = 0. \tag{2.46}$$

(2.46) is an ODE yielding a constant pressure gradient in z-direction and thus a linear pressure for $p^{(0)}$. Assuming the pressure to be the constant atmospheric pressure at the whole free surface and setting this pressure $p_H = p(H(t, x, y)) = 0$, we obtain the **Hydrostatic Pressure Distribution**

$$p^{(0)}(x, y, z, t) = H^{(0)}(x, y, t) - z. \tag{2.47}$$

The non-scaled pressure distribution with constant pressure p_H at the surface reads

$$p_{hy} = p_H + \rho g (H - z). \tag{2.48}$$

The only first order expression in the first order equations (2.43)-(2.46) is $w^{(1)}$. Due to (2.41) and (2.42), $u^{(0)}$ and $v^{(0)}$ are constant over the water depth and thus independent of z. Hence (2.43) can be integrated

$$w^{(1)}(z) = w^{(1)}(z_b) + \int_{z_b}^{z} \frac{\partial w^{(1)}}{\partial z} \, dz = w^{(1)}(z_b) - \int_{z_b}^{z} \frac{\partial u^{(0)}}{\partial x} + \frac{\partial v^{(0)}}{\partial y} \, dz \tag{2.49}$$

$w^{(1)}(z_b)$ as well as $w^{(1)}(H^{(0)})$ are given by the first order equations of the kinematic boundary conditions as

$$\frac{\partial H^{(0)}}{\partial t} + u^{(0)} \frac{\partial H^{(0)}}{\partial x} + v^{(0)} \frac{\partial H^{(0)}}{\partial y} = w^{(1)}(H^{(0)}), \tag{2.50}$$

$$u^{(0)} \frac{\partial z_b}{\partial x} + v^{(0)} \frac{\partial z_b}{\partial y} = w^{(1)}(z_b). \tag{2.51}$$

Replacing $w^{(1)}(z_b)$ in (2.49) by (2.51) yields

$$w^{(1)}(z) = -\left(\frac{\partial u^{(0)}}{\partial x} + \frac{\partial v^{(0)}}{\partial y}\right) z + \left(\frac{\partial (u^{(0)} z_b)}{\partial x} + \frac{\partial (v^{(0)} z_b)}{\partial y}\right) \qquad (2.52)$$

Obviously, (2.52) has to fulfill also (2.50). This condition together with (2.44) and (2.45) where the Hydrostatic Pressure Distribution is inserted yields the 2D-SWE in zeroth order terms:

$$\frac{\partial H^{(0)}}{\partial t} + \frac{\partial u^{(0)}(H^{(0)} - z_b)}{\partial x} + \frac{\partial v^{(0)}(H^{(0)} - z_b)}{\partial y} = 0, \qquad (2.53)$$

$$\frac{\partial u^{(0)}}{\partial t} + u^{(0)}\frac{\partial u^{(0)}}{\partial x} + v^{(0)}\frac{\partial u^{(0)}}{\partial y} + \frac{\partial H^{(0)}}{\partial x} = 0, \qquad (2.54)$$

$$\frac{\partial v^{(0)}}{\partial t} + u^{(0)}\frac{\partial v^{(0)}}{\partial x} + v^{(0)}\frac{\partial v^{(0)}}{\partial y} + \frac{\partial H^{(0)}}{\partial y} = 0. \qquad (2.55)$$

A derivation for the viscid case is given in [16].

2.4.2   Derivation of SWE via Depth Integration

This derivation of the 2D-SWE departs from the 3D-Euler Equations (2.4). Assuming a Hydrostatic Pressure Distribution and inserting (2.48) into the x- and y-momentum equations yields pressure gradient terms in the resulting frictionless 3D-Shallow Water Equations (3D-SWE):

$$\frac{\partial u}{\partial x} + \frac{\partial v}{\partial y} + \frac{\partial w}{\partial z} = 0, \qquad (2.56)$$

$$\frac{\partial}{\partial t}u + \left(u\frac{\partial}{\partial x} + v\frac{\partial}{\partial y} + w\frac{\partial}{\partial z}\right)u + \frac{1}{\rho}\frac{\partial}{\partial x}p_{hy} = 0, \qquad (2.57)$$

$$\frac{\partial}{\partial t}v + \left(u\frac{\partial}{\partial x} + v\frac{\partial}{\partial y} + w\frac{\partial}{\partial z}\right)v + \frac{1}{\rho}\frac{\partial}{\partial y}p_{hy} = 0. \qquad (2.58)$$

Depth-Averaging

The next step in the derivation of the 2D-SWE is the averaging over the water depth by integrating the 3D-SWE from the bottom z_b to the free surface H as done e.g. in [3], [18] or [31].

The 2D-SWE involve only depth-averaged quantities. A scalar function $f(x, y, z)$ is considered as a depth-averaged function $\bar{f}(x, y)$, only depending on x and y by averaging over the water depth $h = H - z_b$.

Definition 2.14

$$\bar{f}(x, y) = \frac{1}{h(x, y)} \int_{z_b}^{H} f(x, y, z) \, dz \qquad (2.59)$$

is defined as the depth-average of the scalar function $f(x, y, z)$.

Depth Integration of Continuity Equation

The integration of the continuity equation (2.56) of the frictionless 3D-SWE

$$0 = \int\limits_{z_b}^{H} \frac{\partial u}{\partial x} + \frac{\partial v}{\partial y} + \frac{\partial w}{\partial z}\ dz = \int\limits_{z_b}^{H} \frac{\partial u}{\partial x}\ dz + \int\limits_{z_b}^{H} \frac{\partial v}{\partial y}\ dz + \int\limits_{z_b}^{H} \frac{\partial w}{\partial z}\ dz.$$

is evaluated by considering the three terms separately. The first term can be evaluated due to the transport theorem (A.8)

$$\int\limits_{z_b(x)}^{H(x)} \frac{\partial u}{\partial x}\ dz = \frac{\partial}{\partial x}\int\limits_{z_b}^{H} u\ dz - u_H \frac{\partial H}{\partial x} + u_b \frac{\partial z_b}{\partial x} = \frac{\partial \bar{u}h}{\partial x} - u_H \frac{\partial H}{\partial x} + u_b \frac{\partial z_b}{\partial x},$$

where

$$\bar{u} = \frac{1}{h}\int\limits_{z_b}^{H} u\ dz \qquad\qquad (2.60)$$

is the depth-averaged velocity in x direction according to Definition 2.14. Similarly, the second term (again $\bar{v}h = h\ 1/h \int_{z_b}^{H} v\ dz = \int_{z_b}^{H} v\ dz$) reads

$$\int\limits_{z_b(y)}^{H(y)} \frac{\partial v}{\partial y}\ dz = \frac{\partial}{\partial y}\int\limits_{z_b}^{H} v\ dz - v_H \frac{\partial H}{\partial y} + v_b \frac{\partial z_b}{\partial y} = \frac{\partial \bar{v}h}{\partial y} - v_H \frac{\partial H}{\partial y} + v_b \frac{\partial z_b}{\partial y}.$$

The integration of the third term is trivial and can be evaluated by applying the Kinematic Boundary Conditions from (2.11)

$$\int\limits_{z_b}^{H} \frac{\partial w}{\partial z}\ dz = w_H - w_b \stackrel{(2.11)}{=} \frac{\partial H}{\partial t} + u_H \frac{\partial H}{\partial x} + v_H \frac{\partial H}{\partial y} - u_b \frac{\partial z_b}{\partial x} - v_b \frac{\partial z_b}{\partial y} - q$$

Since the bottom z_b is assumed to be fixed for all times t, we obtain

$$\frac{\partial H}{\partial t} = \frac{\partial h + z_b}{\partial t} = \frac{\partial h}{\partial t}. \qquad\qquad (2.61)$$

Adding the three terms, most terms cancel and the depth integrated continuity equation of SWE is obtained:

$$\frac{\partial h}{\partial t} + \frac{\partial \bar{u}h}{\partial x} + \frac{\partial \bar{v}h}{\partial y} = q. \qquad\qquad (2.62)$$

Equation (2.62) describes the conservation of mass with possible inflow of water (e.g. in the flow problem *manhole*) given by the source term q.

Depth Integration of Momentum Equations - conservative parts

We proceed similarly with the momentum equations, i.e. we obtain for the depth integration of the conservative part of the x-momentum equation

$$\int_{z_b}^{H} (\frac{\partial u}{\partial t} + u\frac{\partial u}{\partial x} + v\frac{\partial u}{\partial y} + w\frac{\partial u}{\partial z})\ dz \tag{2.63}$$

$$\overset{div\ \vec{u}=0}{=} \int_{z_b}^{H} (\frac{\partial u}{\partial t} + \frac{\partial u^2}{\partial x} + \frac{\partial uv}{\partial y} + \frac{\partial uw}{\partial z})\ dz \tag{2.64}$$

$$= \frac{\partial(h\bar{u})}{\partial t} + \frac{\partial(h\overline{uu})}{\partial x} + \frac{\partial(h\overline{uv})}{\partial y}. \tag{2.65}$$

The detailed integration is given in [31], where again most terms cancel due to the kinematic boundary conditions. In general $\overline{uu} \neq \bar{u}\bar{u}$, and since we do not want to proceed with mixed depth-averages $\overline{uu}$, we compute

$$\frac{\partial(h\overline{uu})}{\partial x} = \frac{\partial(h\bar{u}\bar{u})}{\partial x} + \frac{\partial}{\partial x}\int_{z_b}^{H} (\bar{u} - u(z))^2\ dz \tag{2.66}$$

and for the mixed term

$$\frac{\partial(h\overline{uv})}{\partial y} = \frac{\partial(h\bar{u}\bar{v})}{\partial y} + \frac{\partial}{\partial y}\int_{z_b}^{H} (\bar{u} - u(z))(\bar{v} - v(z))\ dz \tag{2.67}$$

with so-called dispersion terms depending on the depth-profiles $u(z)$, $v(z)$.

Depth Integration of Pressure Gradients

The depth integration of the hydrostatic pressure distribution yields

$$\int_{z_b}^{H} \frac{1}{\rho}\frac{\partial}{\partial x}p(z)\ dz = \int_{z_b}^{H} \frac{\partial}{\partial x}g(H - z)\ dz = \int_{z_b}^{H} g\frac{\partial H}{\partial x}\ dz$$

$$= g\frac{\partial H}{\partial x}(H - z_b) = g\frac{\partial(z_b + h)}{\partial x}h = g\frac{\partial z_b}{\partial x}h + g\frac{\partial h}{\partial x}h$$

$$= \frac{\partial}{\partial x}(\frac{1}{2}gh^2) + gh\frac{\partial z_b}{\partial x} = \frac{\partial}{\partial x}(\frac{1}{2}gh^2) - ghS_{bx}, \tag{2.68}$$

where $S_{bx} = -\partial z_b/\partial x$ is the negative bottom slope in x-direction. Similarly, the integrated pressure gradient for the y-momentum equation reads

$$\int_{z_b}^{H} \frac{1}{\rho}\frac{\partial}{\partial y}p(z)\ dz = \frac{\partial}{\partial y}(\frac{1}{2}gh^2) - ghS_{by}. \tag{2.69}$$

The terms discussed separately above are added for the depth integrated momentum equations: the conservative parts from (2.65) and the depth integrated pressure gradients from (2.68) and (2.69). Neglecting the dispersion terms (or better skipping them into an empirical friction term as described in the next section) yields the frictionless **2D-SWE:**

$$
\frac{\partial}{\partial t}\begin{pmatrix} h \\ uh \\ vh \end{pmatrix} + \frac{\partial}{\partial x}\begin{pmatrix} uh \\ u^2 h + \frac{1}{2}gh^2 \\ uvh \end{pmatrix} + \frac{\partial}{\partial y}\begin{pmatrix} vh \\ uvh \\ v^2 h + \frac{1}{2}gh^2 \end{pmatrix} = \begin{pmatrix} q \\ ghS_{bx} \\ ghS_{by} \end{pmatrix},
$$

$$(2.70)$$

with the variables and parameters listed in Table 2.3.

h	$=$	$H - z_b$	: water depth
u	$=$	$\bar{u} = \frac{1}{h}\int_{z_b}^{H} u\,dz$	: depth-averaged velocity in x-direction
v	$=$	$\bar{v} = \frac{1}{h}\int_{z_b}^{H} v\,dz$	: depth-averaged velocity in y-direction
q			: inflow velocity for water sources $\frac{m}{s}$
g	$=$	$9.81\frac{m}{s^2}$	: earth acceleration
S_{bx}	$=$	$-\frac{\partial z_b}{\partial x}$	: negative bottom slope in x-direction.
S_{by}	$=$	$-\frac{\partial z_b}{\partial y}$	: negative bottom slope in y-direction.

Table 2.3: Variables and parameters in the frictionless 2D-SWE

Explanation 2.15 *Identifying the depth-averaged flow velocities (e.g. $\bar{u}$) from above with the zeroth order flow velocities (e.g. $u^{(0)}$) from the asymptotic expansion, the two formulations of the 2D-SWE (2.70) and (2.53)-(2.55) can be transferred into each other.*

Thus, we have presented two different paths from the Euler Equations to the frictionless SWE.

2.4.3   Friction Approach for SWE

The frictionless SWE are derived from the Euler Equations that do not consider viscous friction. Since the fluid water has a small viscosity of $\nu \approx 10^{-6} m^2/s$, the friction seems to be not important in particular for small scale problems. Thus, the frictionless SWE describe most features of small scale water flow realistically. Since the viscosity of water is not really zero, the flow of water is always connected with small friction. This viscous friction can become important in particular for large scale flow problems.

We consider the flow of water down a hill with constant bottom slope. Applying the frictionless SWE to this flow problem yields increasing momentum due to the bottom slope. Thus the momentum would increase and the water level would decrease on the whole hill. Observations are in contrast to this considerations. The water flow reaches a maximal momentum and a minimal water depth. This is due to the friction acting as a force against the motion, not considered in the frictionless SWE.

Empirical friction formulas were introduced according to observation, that the friction terms depend on the square of the velocity, the water depth and the structure of the bottom. The terms ghS_{fx} and ghS_{fy} are introduced as negative source terms on the right hand side of the SWE (2.70). They are assumed to subsume up the effects of the dominant bottom friction and other internal stresses due to viscous friction and the dispersion terms from (2.66) and (2.67). Due to the dominance of the bottom friction they are called empirical bottom friction terms S_f. The estimation of the friction terms S_f involves an empirical friction parameter, e.g. Manning-Strickler [20] $\vec{u}$

$$\begin{pmatrix} S_{fx} \\ S_{fy} \end{pmatrix} = \frac{n^2 |\vec{u}|}{h^{\frac{4}{3}}} \; \vec{u}. \qquad (2.71)$$

Remark 2.16 *The empirical friction parameter n depends on the type of the bottom and varies from 0 for frictionless bottoms over 0.03 for a street and 0.1 for typical river beds and can reach even higher values. Also other friction laws exist for the SWE (e.g. Chezy-Brahms [31]). These laws differ in the computation of the friction term, but all laws require an empirical friction coefficient.*

2.4.4   1D-SWE

Neglecting the y-dimension in the 2D-SWE yields the 1D-SWE

$$\frac{\partial}{\partial t} \begin{pmatrix} h \\ uh \end{pmatrix} + \frac{\partial}{\partial x} \begin{pmatrix} uh \\ u^2h + \frac{1}{2}gh^2 \end{pmatrix} = \begin{pmatrix} q \\ gh(S_{bx} - S_{fx}) \end{pmatrix}. \qquad (2.72)$$

Historical Remark 2.17 *The 1D-SWE were first derived by Adhémar Jean Claude Barré de Saint-Venant (see Appendix B.2) at the age of 74 in 1871. Generally they are called Saint-Venant equations. In order to use a uniform notation, the name 1D-SWE is applied, but the origin of the equations is emphasized.*

It is also possible to derive these equations via asymptotic expansion or depth integration from the 2D-Euler equations as presented in the previous

section for the 2D case. The friction approach presented in 2.4.3 is also applied to the 1D case. Furthermore (2.72) can be derived heuristically as done in [19]. As remarked in the overview, there exist different formulations of the 1D-SWE. Formulation (2.72) is valid for the flow in a rectangular channel with constant width.

The 1D-SWE are applied very often in literature [1], [18], [20], [26], [31], [45], [51] containing details about the derivation and the properties of the SWE as typical nonlinear hyperbolic PDE.

The nonlinear PDE can be written in quasi-linear form

$$\frac{\partial}{\partial t} \begin{pmatrix} h \\ uh \end{pmatrix} + \begin{pmatrix} 0 & 1 \\ gh - u^2 & 2u \end{pmatrix} \frac{\partial}{\partial x} \begin{pmatrix} h \\ uh \end{pmatrix} = \begin{pmatrix} q \\ gh(S_{bx} - S_{fx}) \end{pmatrix}. \quad (2.73)$$

The eigenvalues of the matrix $\begin{pmatrix} 0 & 1 \\ gh - u^2 & 2u \end{pmatrix}$ are

$$\lambda_1 = u + \sqrt{gh} = u + c, \quad (2.74)$$
$$\lambda_2 = u - \sqrt{gh} = u - c. \quad (2.75)$$

applying the characteristic velocity c from Definition 2.13.

Depending on the relation between the size of u and h, the eigenvalues λ_1 and λ_2 have different or same (usually both positive) signs. This property is important for the characteristics and implies the choice of suitable boundary conditions. In order to differentiate between the two cases,

Definition 2.18 $Fr = \frac{u}{c} = \frac{u}{\sqrt{gh}}$ is defined as the Froude number.

The square of the Froude number gives the ratio between inertia and gravity force $Fr^2 = u^2/gh$. For $Fr < 1$ the flow is called sub-critical and for $Fr > 1$ the flow is called super-critical.

Boundary Conditions
Without loss of generality, we assume a 1D flow oriented in positive x-direction with $u > 0$ in the computational domain $\Omega = [x_l, x_r]$. Illustrating the flow variables in a graph, the inflow boundary x_l is at the left and called left boundary, the outflow boundary x_r is at the right, called the right boundary. The bottom elevation $z_b(x) = 0$ is assumed to be plane yielding $H = h$. No source of water form the ground is assumed with $q = 0$.

The boundary conditions at the free surface and the bottom (in particular the kinematic ones) are already incorporated in the SWE. Thus, only the boundary conditions at the border of the computational domain Ω and initial conditions $h(t = 0, x)$ and $u(t = 0, x)$ for $x \in \Omega$ are required to solve the 1D-SWE uniquely.

Depending on the flow case, different kinds of boundary conditions are required at the left and right boundary: Sub-critical flow with $\lambda_2 < 0 < \lambda_1$ and characteristics in positive and negative x-direction requires one inflow and one outflow boundary condition. The flux $u(t, x_l)h(t, x_l)$ is usually prescribed at the inflow boundary in the sub-critical flow case.

The boundary condition at the outflow for the sub-critical is usually a more difficult choice. In contrast to the inflow boundary, the flux uh is not always given there, but is determined by the flow behavior in the model domain. There exist different possibilities for that boundary condition:

- A wall at the outflow position is assumed with $u(x_r)h(x_r) = 0$.

- The water level $h(t, x_r)$ is prescribed when e.g. a weir is located at the outflow boundary defining a maximum water level.

- A known relation between water level $h(x_r)$ and flux $u(x_r)h(x_r)$ is assumed in free flowing river sections. This relation can be determined by measurements and is applied e.g. for the forecast model of the Rhine river [45]

- A free outflow can be allowed also as boundary condition. For the flow problems handled in this thesis, this outflow boundary condition is usually chosen.

Super-critical flow with $0 < \lambda_2 < \lambda_1$ and characteristics only in positive x-direction requires two inflow $h(t, x_l)$ and $u(t, x_l)$ and no outflow boundary condition.

Since it is possible that the flow case changes in the computational domain causing shocks in the solution, combinations of the types of boundary conditions are possible. An sub-critical inflow can become supercritical due to high bottom slopes. This flow requires only one inflow and no outflow boundary condition. If a supercritical inflow becomes sub-critical two inflow and one outflow boundary conditions are required. The numerical resolution of the shocks occurring in the changing regime has been a hard challenge and has been solved by different suitable techniques [51], [19], [18].

Application to Rivers

The 1D-SWE are usually applied to simulation of open channel flow. In particular for simulation in rivers and their application in forecast systems the 1D-SWE obtain reliable results [45]. For these applications, the natural profiles of the cross sections in the rivers have to be included and the conserved variables are usually changed from h and uh into A and $Q = Au$. Thus, the cross section area A is applied instead of the water depth h and the discharge Q instead of the momentum uh.

Furthermore, $\partial A/\partial h$ occurs in the quasi-linear formulation of the generalized 1D-SWE for real cross sections. The relation between the change of cross section area A in dependence of the water depth h has to be estimated. In the rectangular channel $\partial A/\partial h = b$ is the constant width of the channel. For general cross sections, the size of this term has to be computed from measurements of the cross section profile.

The empirical friction coefficients n are usually fitted to obtain best agreement between model results and measurements [45]. [19] gives a detailed heuristic derivation for the 1D-SWE in that formulation

$$\frac{\partial}{\partial t} \begin{pmatrix} A \\ Q \end{pmatrix} + \frac{\partial}{\partial x} \begin{pmatrix} Q \\ \frac{Q^2}{A} + \frac{1}{2}gA^2 \end{pmatrix} = \begin{pmatrix} q \\ gA(S_{bx} - S_{fx}) \end{pmatrix}. \qquad (2.76)$$

Cylinder-Symmetric Flow Problems
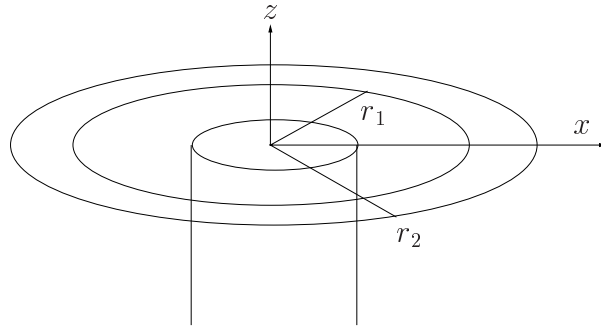
Figure 2.5: Sketch for illustration of cylinder-symmetric flow problem *manhole*

The flow problem *manhole* has a cylinder-symmetry illustrated in Figure 2.5. Thus, polar coordinates are more useful in the description

$$\begin{pmatrix} x \\ y \end{pmatrix} = r \begin{pmatrix} \cos\phi \\ \sin\phi \end{pmatrix}$$

with the velocities
$$\begin{pmatrix} u \\ v \end{pmatrix} = u_r \begin{pmatrix} \cos\phi \\ \sin\phi \end{pmatrix}.$$

The cylinder-symmetrical 1D-SWE (2.77) contain additional source terms on the right hand side due the cylinder-symmetric coordinates as presented in [28]:

$$\frac{\partial}{\partial t} \begin{pmatrix} h \\ u_r h \end{pmatrix} + \frac{\partial}{\partial x} \begin{pmatrix} u_r h \\ u_r^2 h + \frac{1}{2}gh^2 \end{pmatrix} = \begin{pmatrix} q - \frac{hu_r}{r} \\ gh(S_{bx} - S_{fx}) - \frac{hu_r^2}{r} \end{pmatrix}. \qquad (2.77)$$

For stationary solutions of the outflow of water from a manhole as illustrated in Figure 2.5, the flux from the manhole Q_0 is equal to the integral of the flux

hu_r over each circle with radius r around the manhole:

$$Q_0 = Q_r = \int\limits_0^{2\pi} hu_r \, d\phi = 2\pi \, r \, hu_r.$$

Comparing the fluxes Q_{r_1} and Q_{r_2} over two circles with radius r_1 and r_2 yields

$$hu_{r_1} = \frac{hu_{r_2}}{\frac{r_1}{r_2}},$$

leading to the mass source term $-hu_r/r$ in (2.77).

2.5 Numerical Solution Schemes

Since analytical solutions for the NSE and the SWE exist only for some idealized and restricted applications (e.g. frictionless dam break problem for SWE), numerical solution schemes are usually applied to solve the equations of motion.

There exist plenty of literature about numerical schemes for NSE and SWE (e.g. [17], [18], [49], [26], [35] [51]) with a wide variety of different approaches: Finite Differences Schemes, Finite Element Methods, Finite Volume Schemes as well as mesh-free Particles Schemes have been applied already successfully to the equations. This section is restricted to a short overview of the numerical methods applied to the calculation of the results presented in Chapter 3.

2.5.1 Numerical Solution Scheme for NSE

The Finite Pointset Method FPM developed by Kuhnert and Tiwari [23], [48] [49] is applied to solve the NSE for the free surface flow of water. The FPM is a mesh-free particle (i.e. Lagrangian) method where numerical particles carry the fluid information and are moved with the fluid velocity within a particle projection method.

Instead of using a fixed and regular computational grid as in Finite Difference or Finite Volume schemes, the set of particles is considered as the computational grid. The NSE are discretized directly on each particle. Therefore, spatial derivatives of fluid quantities (e.g. pressure) have to be estimated by considering the particles in the vicinity.

Since the particles are moved with the fluid flow, the computational grid and also the vicinity relations change during the calculation. That increases the difficulty of the mesh-free approach, but enables the handling of complex geometries, in particular free surfaces.

Projection method

As proposed in [7], an explicit projection method of first order accuracy in time is used, consisting of two steps: First, the new particle position $\vec{x}^{n+1}$ at time t^{n+1} and the intermediate velocity $\vec{u}^*$ are computed explicitly from the value at time t^n (time step $t^{n+1} - t^n = \delta t$):

$$\vec{x}^{n+1} = \vec{x}^n + \delta t \ \vec{u}^n \tag{2.78}$$

$$\vec{u}^* = \vec{u}^n + \delta t \ \nu \Delta \vec{u}^n + \delta t \ \vec{g} \tag{2.79}$$

In the second step, $\vec{u}^*$ is corrected by solving the equations

$$\vec{u}^{n+1} = \vec{u}^* - \delta t \ grad \ p^{n+1} \tag{2.80}$$

with the incompressible constraint

$$div \ \vec{u}^{n+1} = 0. \tag{2.81}$$

By taking the divergence of (2.80) and involving (2.81) we obtain a Poisson equation for the pressure

$$\Delta p^{n+1} = \frac{div \ \vec{u}^*}{\delta t}. \tag{2.82}$$

For further details (e.g. boundary conditions) we refer to [48].

Weighted Least Square Method WLS

Within the projection method, numerical approximation of derivatives are required. A weighted least square method is applied to the finite point set:

The function values $f(\vec{x})$ are given on a finite number of discrete points $\vec{x}_i$ for $i = 1, 2, ..., N$. For the computation of a derivative the value at the point $\vec{x}_i$ is compared to the values of the points in the vicinity of $\vec{x}_i$, given e.g. by a ball with a radius r. Since the distribution of the points in the ball around $\vec{x}_i$ is not regular, the distances between the particle on $\vec{x}_i$ and the particles on $\vec{x}_j$ vary in the interval $(0, r]$ and also within time.

These distances are applied to define a weighting function $\varphi(\vec{x}_i - \vec{x}, r)$ with compact support (i.e. the ball). Following [49],

$$\varphi(\vec{x}_i - \vec{x}, r) = \begin{cases} exp(-\alpha \frac{\|\vec{x}_i - \vec{x}\|^2}{r^2}) - exp(-\alpha) & , \ \text{if } \|\vec{x}_i - \vec{x}\| \leq r \\ 0 & , \ \text{else} \end{cases} \tag{2.83}$$

is a possible choice for the weighting function with a real constant $\alpha \in \mathbb{R}^+, \alpha \approx$ 6. The smaller the size of r the finer the resolution of the scheme and the higher the number of particles.

The derivatives can be computed using a Taylor series expansion and a least square approximation on the neighboring points, where the weighting

function φ is involved as presented in detail in [49].

The computational effort for the approximation of a derivative is higher than within a grid-based approach, where the vicinity relations on the fixed computational grid can be used for efficient calculations. On the other hand, approaches with a fixed mesh do not have the flexibility of the presented particle scheme. In particular simulations with complex or moving flow geometries such as free surfaces are more efficient in the particle method framework.

2.5.2   Numerical Solution Scheme for SWE

A Finite Volume Scheme is applied to the 2D-SWE as well as for the 1D-SWE first derived by Toro [51]. Finite Volume schemes are based on the integral form of conservation laws and are thus also valid for weak solutions enabling the application also to discontinuous solutions as e.g. for dam break simulations.

The high resolution Godunov-type method is second order accurate and uses MUSCL (Monotonic Upstream Schemes for Conservation Laws) reconstruction and a simple but robust approximative Riemann solver. Haasenritter [18] extended the scheme, originally constructed only for homogeneous SWE, to the inhomogeneous equations opening the applicability to simulations over non-horizontal ground with varying roughness. Special attention has to be given in order to balance the discretizations of the conservative part and the inhomogeneous part of the pressure gradient terms from (2.68) and (2.69) [15].

Furthermore, the scheme is adapted to problems with dry bottom. Most numerical schemes for SWE are not capable of simulating situations where the water depth h is zero.

For further details of the numerical scheme we refer to the diploma thesis of Haasenritter [18] where different test calculations demonstrate the applicability and accuracy of the scheme.

Chapter 3

Results: 2D-NSE vs Classical 1D-SWE

We restrict this and the next two chapters to flow problems only in 2D-profiles and proceed to 3D-problems in Chapter 6. This simplification reduces the computational effort enormously whereby nevertheless the potential to compare the results of the different model approaches and to develop extensions of the classical SWE is conserved.

The two challenging flow problems *manhole* and *curb* were already introduced in Section 1.2. We first present the numerical solutions of the 2-NSE. These numerical results are then confirmed by analytical solutions derived from stationary considerations with the in-viscid 2D-Euler Equations. We proceed presenting the solutions of the classical 1D-SWE.

Relying on the confirmed numerical results of the NSE, we define them as benchmark solutions since no experimental data are available. Following Explanation 2.3, the discrepancies of the classical SWE to the benchmark solution are interpreted as an impreciseness of the SWE model approach demonstrating the need for extensions.

3.1 Flow Problem *Manhole*

The flow problem *manhole* -already introduced in Section 1.2- is a special flow problem in flood simulations in urban areas. We simulate a constant inflow $q(t) = q$ of water from the manhole onto the initially dry street. Bottom structures in the street are neglected ($z_b = 0$ everywhere) to focus on the outflow problem.

As illustrated in Figure 3.1, we assume the problem in a 2D-profile with symmetry to the center line of the manhole at $x = 0$. At the inflow interval

35
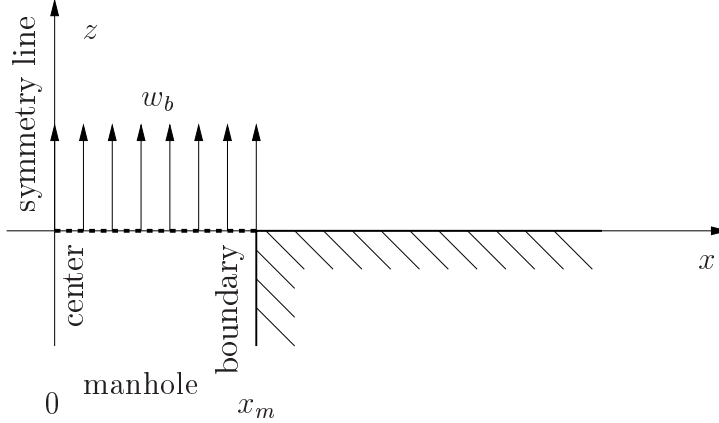
Figure 3.1: Sketch of the flow problem *manhole* in a 2D-profile

$[0, x_m]$ between the center ($x = 0$) and the boundary x_m of the manhole, a constant vertical inflow velocity $w_b = q$ is assumed. We choose the manhole radius to be $x_m = 0.3m$ for all simulations and compute solutions for different inflow velocities w_b, in particular for $w_b = 1m/s$, $w_b = 2m/s$ and $w_b = 3m/s$. We choose the computational domain $\Omega = [x_l, x_r] = [0m, 2m]$ large enough to include all effects in the vicinity of the manhole.

3.1.1 Solutions with 2D-NSE

The 2D-NSE solutions calculated with the FPM-Code of Kuhnert and Tiwari [49] -presented in Section 2.5.1- are illustrated in Figure 3.2. The inflow velocity is chosen as $w_b = 1m/s$ for the presentation of in-stationary results. The velocity vectors of the fluid particles at the time steps $t = 0.6s, 0.7s, 0.8s$ and $2.0s$ are presented as blue arrows.

Due to the inflow condition at the manhole $[0, x_m]$, a water column is rising above this interval. The vertical velocities decrease with their distance to the bottom owing to gravity force. The flow is also distributed in the horizontal direction and floods the street. Due to the vertical inflow velocities w_b, the region of the street directly beside the manhole remains dry initially, but is finally filled with water and a vortex region develops. Far away from the manhole, the flow becomes uniform with constant water level h and flow velocity u_0 above a small bottom layer.

Figure 3.3 illustrates three stationary solutions for the inflow velocities $w_b = 1m/s$ (top), $w_b = 2m/s$ (middle) and $w_b = 3m/s$ (bottom). The water level of the free surface H is the upper border of the fluid domain.

Remark 3.1 *The water level H_{NSE} is not given explicitly by the applied NSE solution scheme. A function is fitted to the locations of the particles at the*
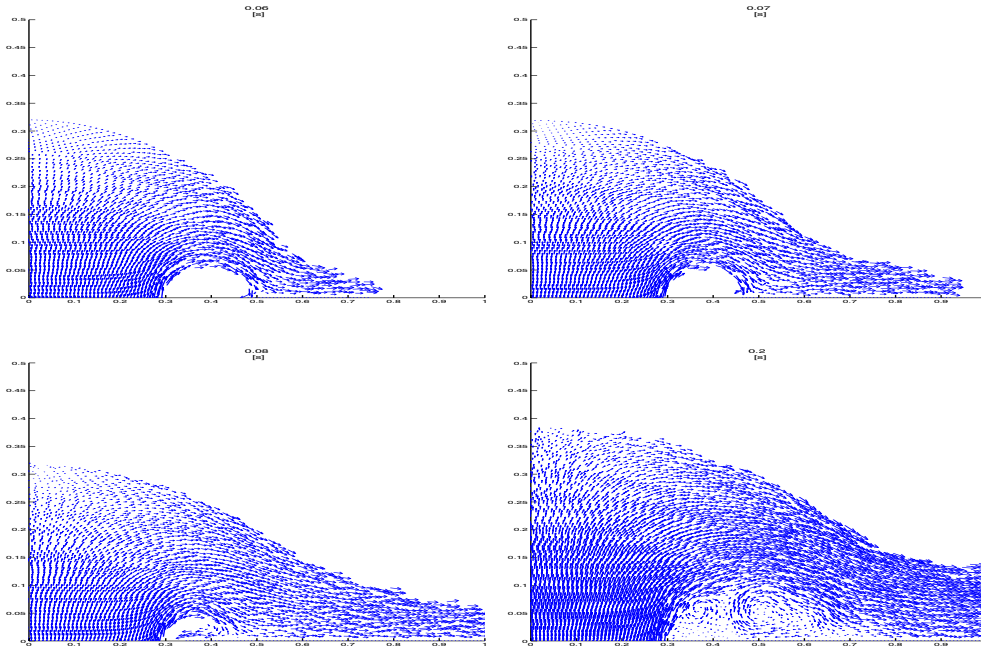
Figure 3.2: 2D-NSE solutions for the flow problem *manhole* as velocity vectors in the fluid domain at the time steps $t = 0.6s, 0.7s, 0.8s$ and $2.0s$ (from top left to right bottom)

surface at the upper limit of the flow domain. The FPM-code marks these surface particles for the required evaluation of the water level H_{NSE}.

We consider two selected points of the free surface:

- The height of the water column above the manhole -denoted with H_c

- and the water depth at the outflow boundary x_r -denoted with h_o

H_c and h_o increase with the vertical inflow velocity w_b. Their dependencies will be compared to those of other model approaches.

The size of the vortex region also increases with w_b. Furthermore it is obvious that the vortex region usually dominated by one big vortex contain several smaller vortices. Vortices can be separated from the region and travel with the flow out of the computational domain. The dynamics of these vortices inhibit a really stationary solution yielding only quasi-stationary solutions. We select one solution that appears to be close to the average of different quasi-stationary solutions and define this solution to be the stationary benchmark solution for comparison to the results of other model approaches.
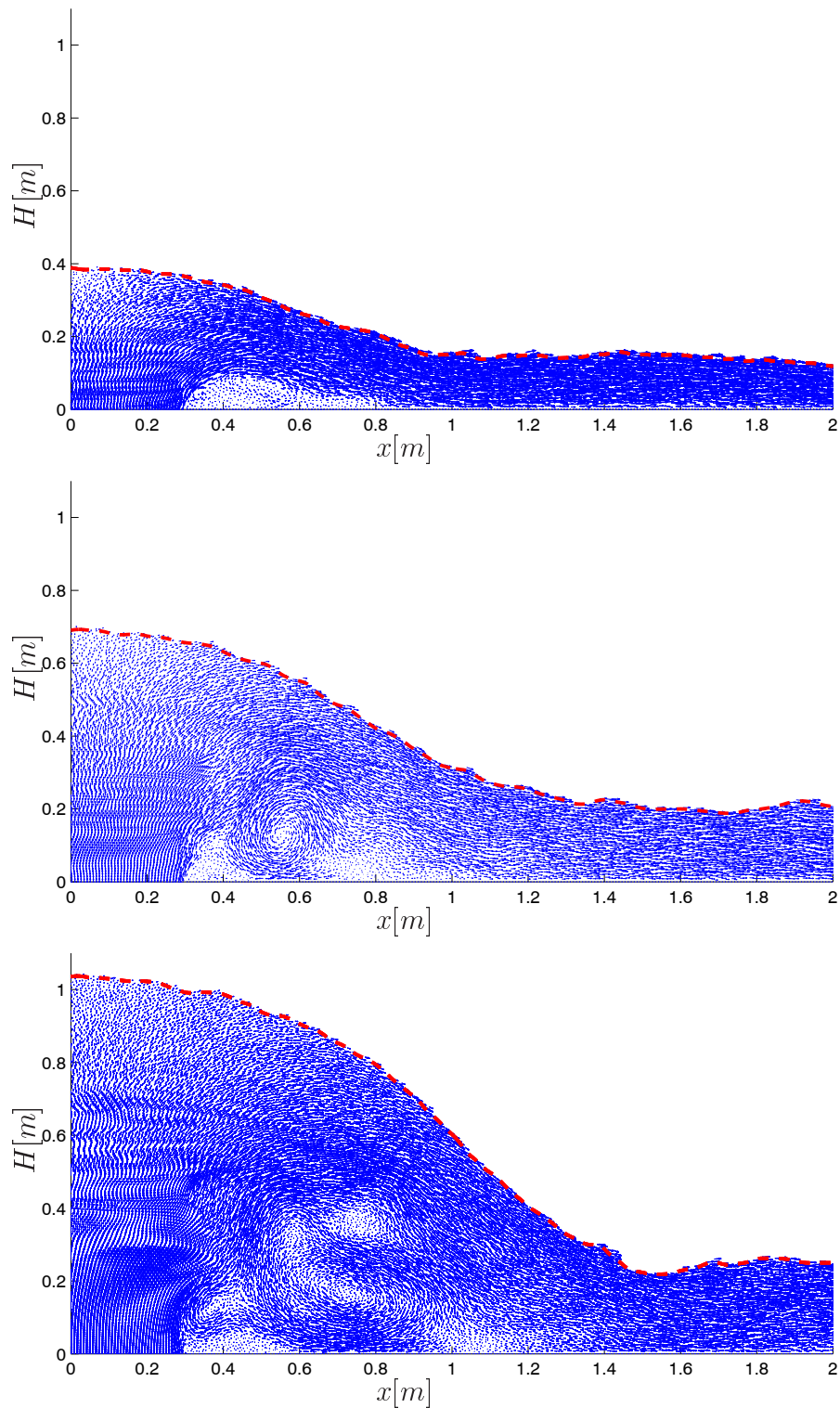
Figure 3.3: Selected stationary benchmark solutions of 2D-NSE for the flow problem *manhole* for the inflow velocities $w_b = 1m/s$ (top), $w_b = 2m/s$ (middle) and $w_b = 3m/s$ (bottom) as velocity arrows and water level H_{NSE} (as red dashed line)

3.1.2 Analytical Solutions with Stationary 2D-Euler

Neglecting viscous friction, the flow is described by the 2D-Euler Equations instead of the 2D-NSE. Instead of solving these equations numerically -as done for the NSE in the previous section- we present a stationary analytical solution obtained by considerations of continuity equation, momentum conservation and Bernoulli's law on streamlines.

Point	variable	value
1	p	p_0
	u	0
	w	w_b
2	p	0
	u	0
	w	0
3	p	p_0
	u	0
	w	w_b
4	p	$\rho g h_o$
	u	u_o
	w	0
5	p	0
	u	u_o
	w	0
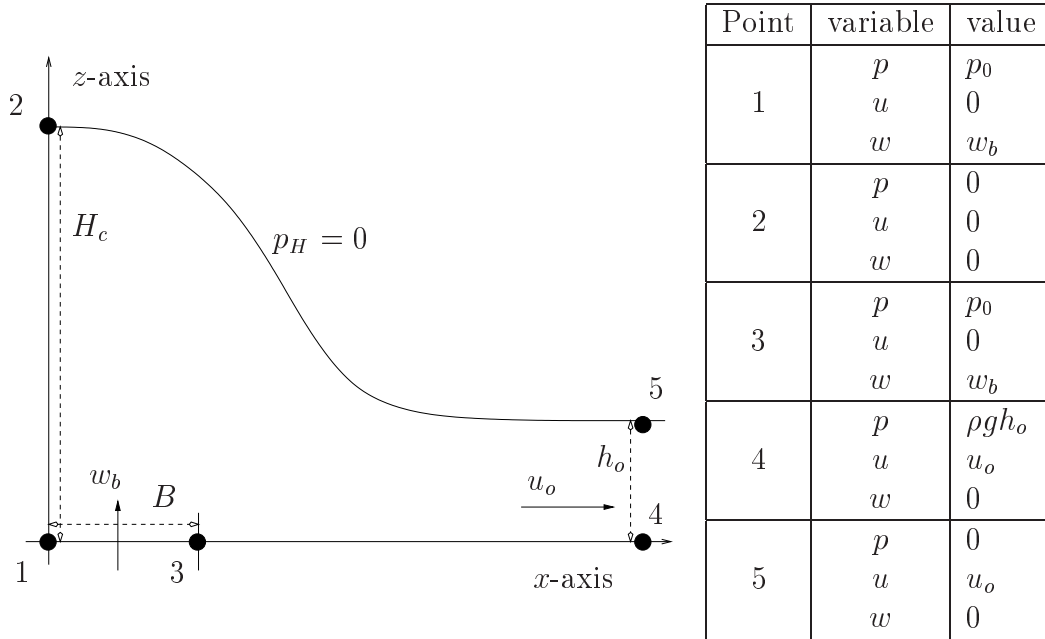
Figure 3.4: Sketch of the stationary solution of the flow problem *manhole* with assumptions to derive an analytical solution

Figure 3.4 sketches the stationary solution comparable to the stationary benchmark solutions in Figure 3.3. We assume the constant atmospheric pressure at the free surface to be zero $p_H = 0$. We denote $B = x_m$ as the radius of the manhole and thus the length of the inflow interval $[0, x_m]$. The height of the water column above the manhole is denoted with H_c as done in the previous section.

We further assume that the flow becomes uniform with the flow velocity u_o and the water depth h_o at the outflow cross section in between the selected points 4 and 5 in Figure 3.4. A hydrostatic pressure distribution is assumed in between points 4 and 5.

An overview of the assumptions for the velocities u and w and pressure p at the selected points 1-5 is given in the table beside the figure. For a given inflow velocity w_b, we seek 4 unknowns H_c, p_0, h_o and u_o requiring 4 equations.

Continuity equation

For stationary flow, the inflow flux between the points 1 and 3 is identical to the outflow flux between the points 4 and 5, yielding

$$w_b B = u_o h_o. \tag{3.1}$$

Bernoulli

Due to Bernoulli's law, the energy

$$\frac{1}{2}\vec{u}^2 + \frac{p}{\rho} + gh = const. \tag{3.2}$$

remains constant on streamlines. We consider the two streamlines from point 1 to 2 and from point 2 to 5 and obtain

$$\frac{1}{2}w_b^2 + \frac{p}{\rho} = gH_c, \tag{3.3}$$

$$gH_c = \frac{1}{2}u_o^2 + gh_o. \tag{3.4}$$

(3.1), (3.3) and (3.4) are 3 equations for the 4 unknowns. Bernoulli's law on streamline $(3, 4)$ and any further energy consideration (even integrated ones) do not result in a new independent equation.

Departing from the vertical momentum equation, we develop a formula for the pressure on the streamline $(1, 2)$ to obtain the 4th equation for the analytical solution. We assume w to decrease linearly on the streamline $(1, 2)$ from the vertical inflow velocity w_b to zero

$$w(z) = w_b \frac{H_c - z}{H_c}$$

and consider a 2nd oder ansatz function for the pressure distribution

$$p(z) = Az^2 + Bz + C.$$

The vertical momentum equation of the 2D-Euler Equations reads:

$$u\frac{\partial w}{\partial x} + w\frac{\partial w}{\partial z} = -\frac{1}{\rho}\frac{\partial p}{\partial z} - g.$$

Since $u = 0$ on this streamline, we obtain

$$\frac{\partial}{\partial z}\left(\frac{1}{2}w^2 + \frac{p}{\rho}\right) = -g$$

Comparing the coefficients and inserting $p(H) = 0$, we obtain:

$$\frac{p(z)}{\rho} = -\frac{w_0^2}{2H_c^2}z^2 + \left(\frac{w_0^2}{H_c} - g\right)z + gH_c - \frac{w_0^2}{2}. \tag{3.5}$$

Remark 3.2 $p(0) = p_0$ *is equivalent to (3.3)*

The integrated momentum conservation equation reads

$$\oint \vec{u}(\vec{u} \cdot \vec{n}) \, dA + \oint \frac{p}{\rho} \vec{n} \, dA = 0. \qquad (3.6)$$

Applying this to the horizontal momentum conservation for the whole flow domain (1,2,5,4) yields the 4th equation required for the analytical solution

$$u_o^2 h_o = \int\limits_0^{H_c} \frac{p(z)}{\rho} \, dz - \int\limits_0^{h_o} g h_o \, dz = \frac{1}{2} g H_c^2 - \frac{1}{2} g h_o^2 - \frac{1}{6} w_b^2 H_c. \qquad (3.7)$$

We obtain a set of 4 nonlinear equations (3.1), (3.3), (3.4) and (3.7) for the 4 unknowns H_c, p_0, h_o and u_o. This set has only one real solution with positive values for u_o. Instead of presenting the elaborated analytical form of the solution, we compare the dependencies of H_c and h_o on the inflow velocity w_b from this analytical solution with the results from 2D-NSE and 1D-SWE in Figure 3.7 in Section 3.1.4.

3.1.3 Results with 1D-SWE

In the SWE model approach, the mass source term $q = w_b$ is prescribed at the inflow interval $[0, x_m]$. At the left boundary $x = 0$, the symmetry line, a reflecting boundary condition is assumed and at the right boundary a free outflow of is allowed (see Section 2.4.4). We apply the 1D-SWE with the friction approach of Manning and Strickler as described in Section 2.4.3 and set $n = 0.03$ typical for streets.

Figure 3.5 illustrates the SWE results of the flow problem *manhole*. The water level H_{SWE} (solid green line) and the (scaled) velocity $1/10 \, u_{SWE}$ (dashed red line) at the time steps $t = 0.2s$, $0.4s$, $0.6s$, $0.8s$, $2.0s$ and $5.0s$ are presented. The principle flow behavior with SWE is similar to that of the NSE benchmark solution: Above the manhole a water column rises and the water floods the street. The distributions of water in the street are different. In the SWE results, water flows immediately in the x-direction and the street is flooded quicker. A comparison between the solutions at $0.6s$ of the NSE (Figure 3.2 top left) and of the SWE (Figure 3.5 middle left) demonstrates this difference. Another difference to the NSE solution is that neither the dry region at the boundary of the manhole nor the developed vortex region can be re-produced in the SWE results.
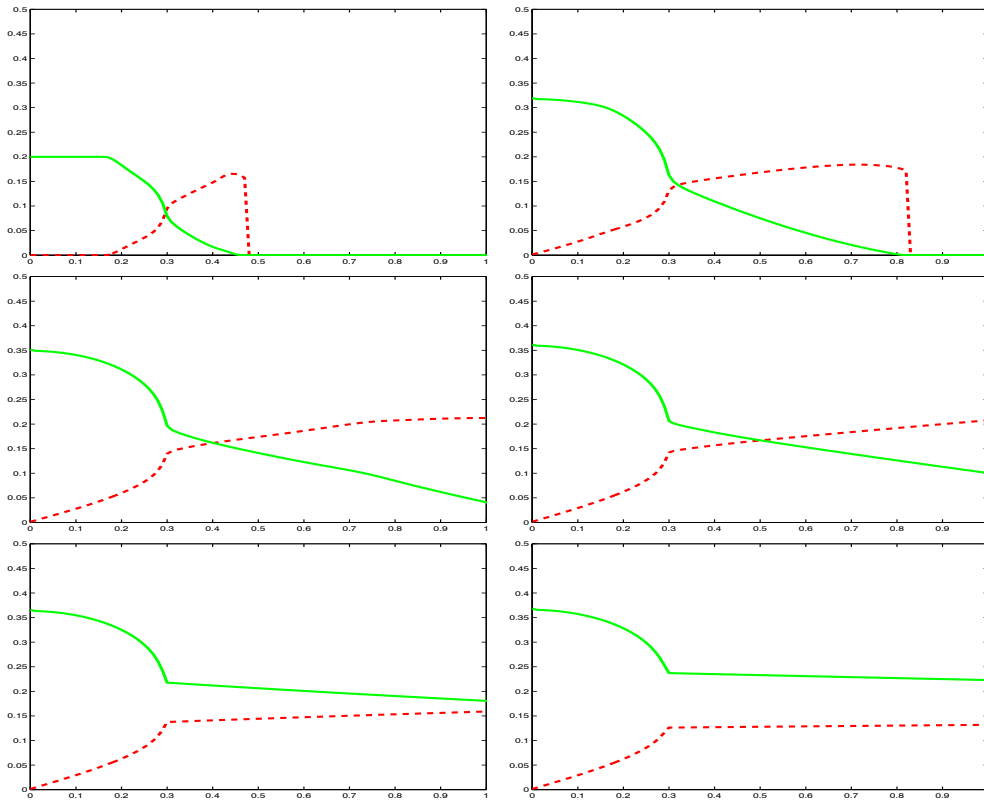
Figure 3.5: SWE results: water level H_{SWE} (solid green line) and the velocity $1/10$ u_{SWE} (scaled as dashed red line) at the time steps $t = 0.2s, 0.4s, 0.6s, 0.8s, 2.0s$ and $5.0s$ (from top left to right bottom)
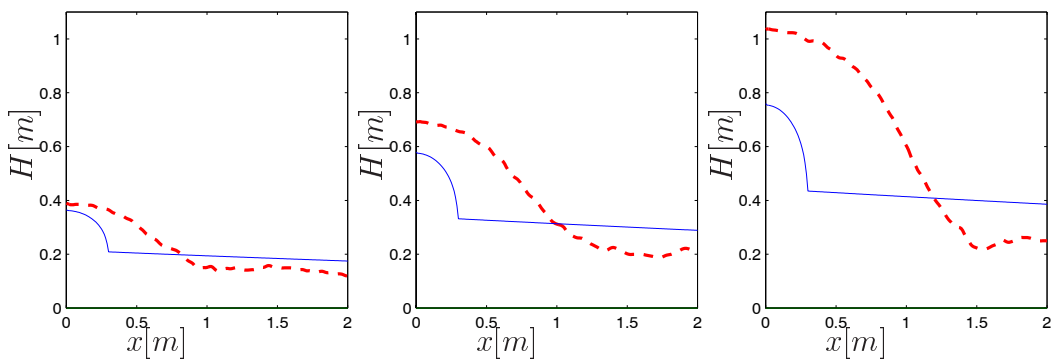
Figure 3.6: Comparison of stationary solutions of water levels for the flow problem *manhole*. H_{NSE} as dashed red line, H_{SWE} as solid blue line for the inflow velocities $w_b = 1m/s$ (left) $w_b = 2m/s$ (middle) and $w_b = 3m/s$ (right)

3.1.4 Comparison of Results

The SWE solution becomes really stationary. Figure 3.6 compares the water levels H_{SWE} of the stationary solutions from SWE to the NSE benchmark water levels H_{NSE} for the inflow velocities $w_b = 1m/s$ (left), $w_b = 2m/s$ (middle) and $w_b = 3m/s$ (right). Serious local as well as global differences in the water levels are obvious.

We focus the comparison to the two selected points in the free surface H_c (height of water column) and h_o (outflow water depth) as announced in the previous sections.
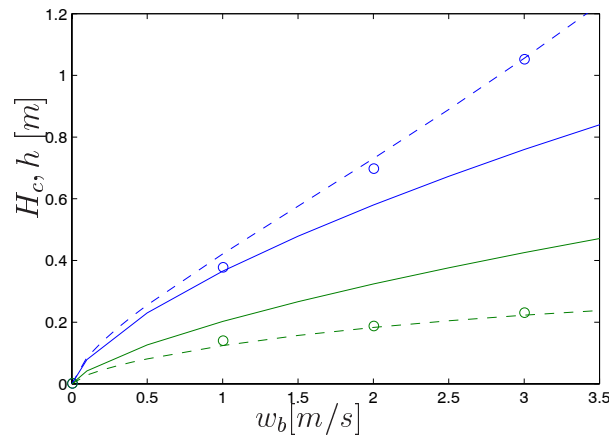
Figure 3.7: Comparison of dependencies of H_c (blue) and h_o (green) on the inflow velocity w_b from analytical considerations (dashed line), from classical SWE (solid line) and from the NSE benchmark solutions (circles)

Figure 3.7 compares of dependencies of H_c (blue) and h_o (green) on the inflow velocity w_b. The numerical NSE benchmark solutions (circles) are confirmed by the analytical in-viscid solution (dashed line). This approves the assumption that the friction has no dominant effect on the local flow behavior.

The solutions of the classical SWE (solid line) are rather far away from the NSE benchmark solutions in particular for high inflow velocities w_b. H_c is too low and h_o is too high. Thus the Froude number Fr at the outflow boundary x_r is computed too low with the classical SWE approach. For $w_b = 3m/s$ the difference is approximately a factor 5. These differences are truly crucial for the assessment of flood risks.

3.2   Flow Problem *Curb*

The challenging flow problem *curb* introduced in Section 1.2 is another special flood situation in urban areas. In contrast to the assumption of a plane street in the flow problem *manhole*, the street is usually bordered by sidewalks with curbs of some centimeters height. The reliable simulation of this flow problem *curb* is crucial to assess the flood risk of the houses connected to the street. Instead of coupling the flow problems *manhole* and *curb* as they occur in the real applications, the problems are considered isolated in order to examine them separated.
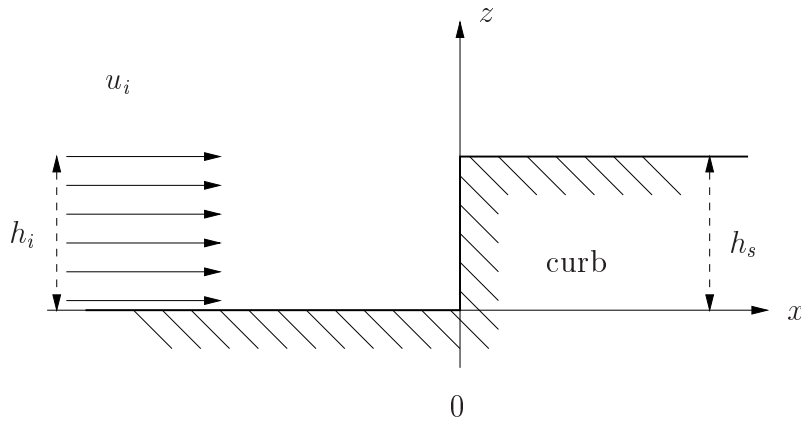
Figure 3.8: Sketch of the flow problem *curb*

Figure 3.8 illustrates the plane topography of the street and of the sidewalk with a single jump of size h_s in the bottom elevation at the curb located at $x = 0m$. Choosing the height of the curb $h_s = 0.1m$ defines the entire bottom elevations in the computational domain $\Omega = [x_l, x_r] = [-1m, 1m]$

$$z_b(x) = \left\{ \begin{array}{ll} 0 & , x < 0, \\ h_s & , x \geq 0. \end{array} \right. \tag{3.8}$$

We assume an initially dry street and prescribe the inflow at the left.

3.2.1   Benchmark Solutions with NSE

Sub-critical case

For sub-critical inflows Q with small velocities u_i the flow is reflected at the curb and the water floods back to the symmetry line and is reflected again. Figure 3.9 illustrates the stationary solution for the sub-critical case with $Q = 0.1m^2/s$ in the vicinity of the curb.
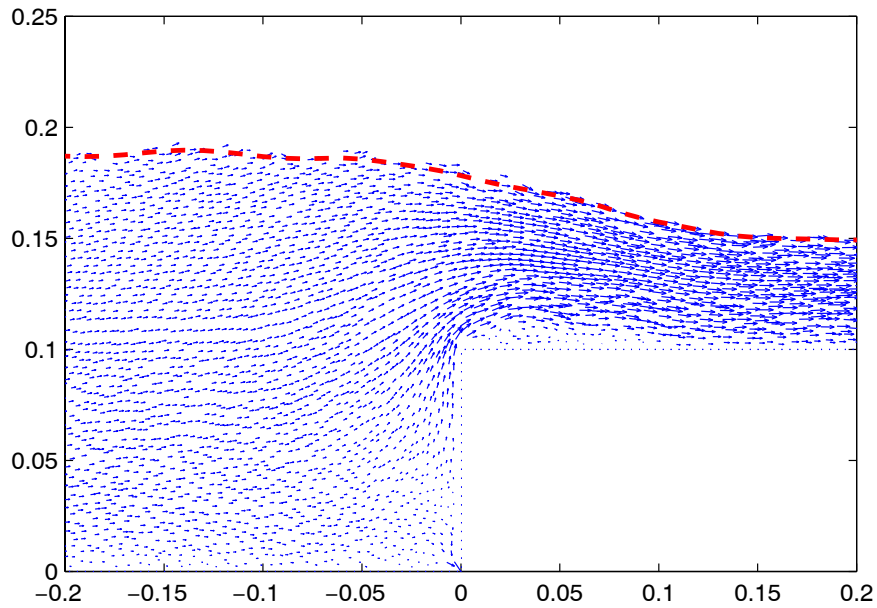
Figure 3.9: Selected stationary NSE benchmark solution for the flow problem *curb* in the sub-critical case: Velocity arrows in blue and water level H_{NSE} as red dashed line
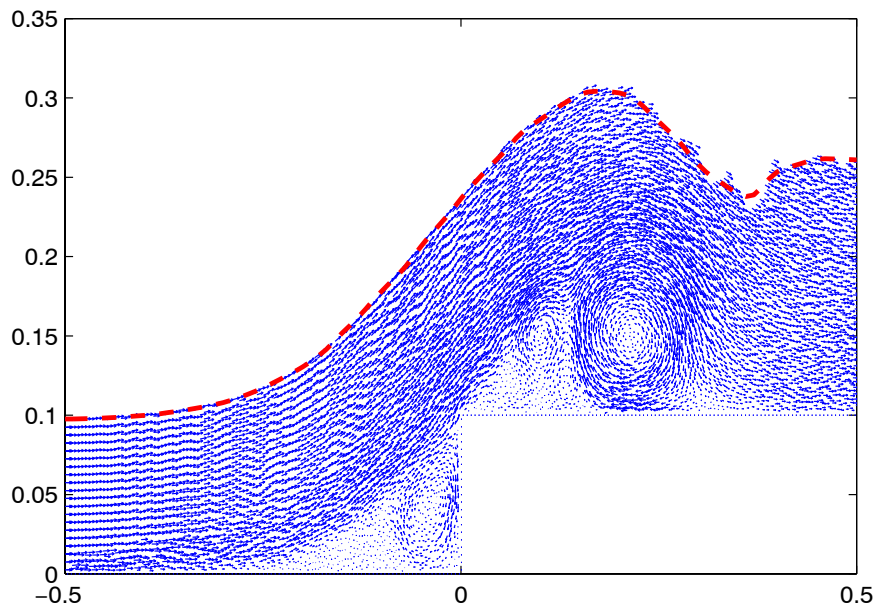
Figure 3.10: Selected stationary NSE benchmark solution for the flow problem *curb* in the super-critical case: Velocity arrows in blue and water level H_{NSE} as red dashed line

In front of the curb, the water level h_i is higher than the water level h_o behind the curb. The inertia of the inflow is not sufficient to flow over the curb. Instead, the water level in front of the curb raises and the gravity force finally yields to the flow over the curb.

Super-critical case

For high Froude numbers (e.g. $Fr = 3$), there is no reflection at the curb and the water flows over the curb establishing dynamic vortex regions in front and behind the curb as illustrated in Figure 3.10. The solution behind the curb is dynamic and vorticies separate from the vortex regions and are transported through the flow domain.

The inertia of the inflowing water is high enough to let the water jump over the curb. The water level H behind the curb is higher than in front of the curb. Same holds even for the water depth h. The surface structure behind the curb is influenced by the vortex motions.

3.2.2   Analytical Solutions with Stationary 2D-Euler

Analogously to the flow problem *manhole*, we assume in-viscid stationary flow described by the 2D-Euler Equations.
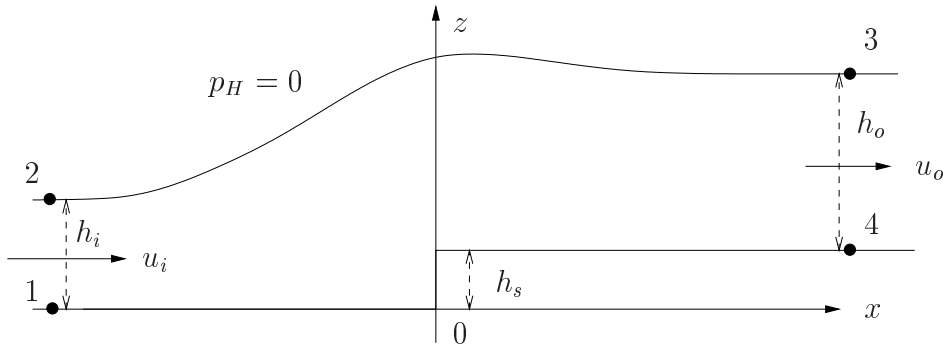
Figure 3.11: Sketch of the stationary solution for the flow problem *curb* with assumptions to derive an analytical solution

Figure 3.11 illustrates the flow behavior of the flow problem *curb* in the super-critical case. Nevertheless, the following derivations are valid for all stationary flow cases.

Again, we assume the constant atmospheric pressure to be zero pressure at the surface $p_H = 0$. At the left inflow boundary we assume a homogeneous horizontal inflow velocity u_i with the water depth h_i. At the outflow boundary on the right hand side, we assume a constant horizontal outflow velocity u_o with a water depth h_o.

Furthermore, a uniform horizontal flow with $w = 0$ and a hydrostatic pressure distribution is assumed at the inflow and outflow boundary (all selected points 1-4).

We are interested in the relations between the unknowns u_i, h_i, u_o and h_o.

Continuity equation

For stationary flow, the flux through the inflow line between point 1 and 2 is equal to the outflow flux between the points 3 and 4

$$u_i h_i = u_o h_o. \tag{3.9}$$

Bernoulli

Applying Bernoulli's law (3.2) to the streamlines 2 to 3 and 1 to 4 yields identically

$$u_i^2 + 2gh_i = u_o^2 + 2g(h_o + h_s). \tag{3.10}$$

Inserting (3.9) into (3.10) yields

$$u_o^3 + (2gh_s - 2gh_i - u_i^2)u_o + 2gu_i h_i = 0. \tag{3.11}$$

Assuming that h_s, h_i and u_i are given, the analytical solution for the unknowns h_o and u_o can thus be evaluated. (3.11) is a third order algebraic equation yielding three solutions $u_o \in \mathbb{C}$. Since only $u_o \in \mathbb{R}^+$ is physically relevant, we choose the appropriate solutions derived by MAPLE.
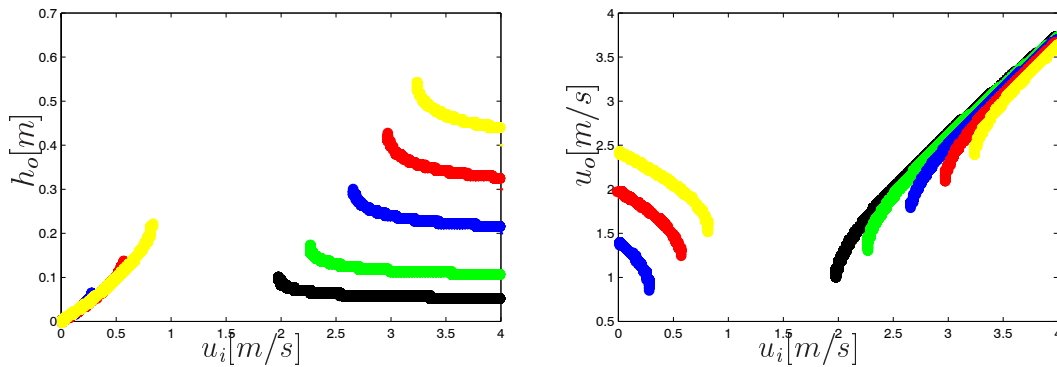
Figure 3.12: Dependency of the outflow water depth h_0 (left hand side) and the outflow velocity u_o (right hand side) on the inflow velocity u_i for different inflow heights $h_i = 0.5h_s$ (black), h_s (green), $2h_s$ (blue), $3h_s$ (red), $4h_s$ (yellow) with $h_s = 0.1m$ from analytical solution

Figure 3.12 illustrates the dependencies of $h_o(u_i)$ (left) and $u_o(u_i)$ (right) for different choices of $h_i = 0.5h_s, h_s, 2h_s, 3h_s, 4h_s$ (colors) for $h_s = 0.1m$.

Two separated sets of solutions for the sub-critical and the super-critical flow case are visible. On the right hand sides of the two figures, the super-critical solutions are visible. These solutions require a minimal inflow velocity u_i with enough inertia to flow over the curb. The water depth h_o is always higher than the inflow water depth $h_i < h_o$. h_i is illustrated as a small colored dot on the right boundary of the left figure. This is due to the loss of momentum to lift over the curb. This loss of momentum is also visible for the velocities u_o in the right figure since $u_o < u_i$.

On the left hand sides of the two figures, the sub-critical solutions are visible. The water levels in front of the curb are always higher than behind the curb and $h_i + h_s > h_o$ holds.

For the inflow heights $h_i = 0.5h_s$ (black) and $h_i = h_s$ (green) there are no sub-critical stationary solutions, since the flow is reflected and a water height $h_i > h_s$ is established.

The major difference between the two sets of solution is that the sub-critical flow over the curb is only possible due to the slack flow caused by reflection and not -as in the super-critical case- due to the inertia of the flow itself.

In the gap between the sub-critical and super-critical stationary solutions there exist no stationary solution.

3.2.3 Comparison with 1D-SWE Results

The curb is not modeled as a real step of infinite slope in the classical SWE, but considered as a jump h_s within one grid cell with size dx yielding the slope h_s/dx.

For the different flow cases, appropriate boundary conditions are required for the SWE solution as described in Section 2.4.4.

For sub-critical flow ($Fr < 1$), one inflow and one outflow boundary condition are required. We prescribe the inflow flux at the left boundary x_l as the constant flux $Q_i(x_l)_i = u_i h_i$. We allow a free outflow at the right boundary x_r.

For super-critical flow ($Fr > 1$), two inflow and no outflow boundary conditions are required. The inflow flux Q_i is prescribed by setting the water depth h_i as well as the velocity u_i.

Sub-critical case

Similar to the NSE solution, the sub-critical flow is reflected at the curb, before a stationary solution is obtained.

Figure 3.13 compares the stationary water levels H_{SWE} and H_{NSE} for the sub-critical flow at the left hand side. H_{SWE} is close to H_{NSE} in the vicinity of the curb. The principle flow behavior is similar to the NSE and the analytical solution. For the stationary sub-critical flow, the SWE approach is applicable. The discrepancy between the numerical SWE results and the NSE solutions is caused in particular by the implementation of the curb as a jump in one computational grid cell. Haasenritter [18] suggested a special numerical treatment of the flux at discontinuities in the bottom leading to even more accurate results for sub-critical flows.
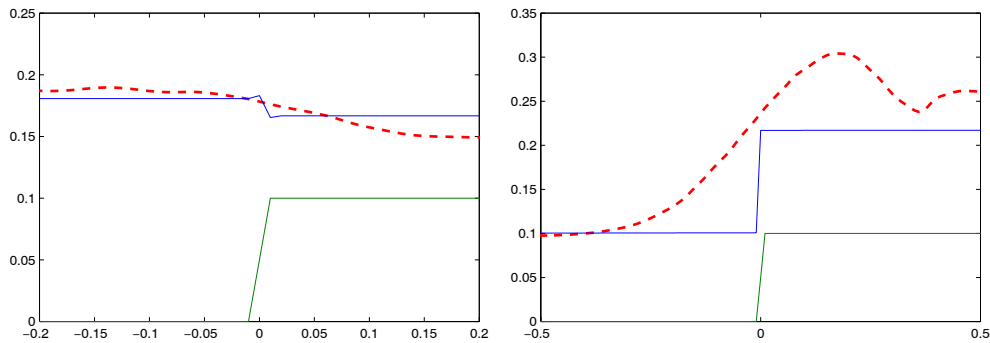
Figure 3.13: Comparison of stationary solutions of water levels for the flow problem *curb*: H_{NSE} as dashed red line, H_{SWE} as solid blue line and bottom z_b as green line for sub-critical flow (left hand side, $Q_i = u_i \cdot h_i = 0.1 m^2/s$) and for super-critical flow (right hand side, $u_i = 3m/s h_i = 0.1m$)

Super-critical case

The right hand side of the figure compares the water levels for the super-critical flow illustrating local differences in front and behind the curb. The water level H_{SWE} is constant h_i in front and constant h_o behind the curb, similar to structure of the the bottom elevation z_b. Due to the loss of momentum caused by the bottom slope h_s/dx at the curb, the water depth behind the curb is higher $h_o > h_i$. The SWE register the curb in fact only as a locally restricted negative source term in the momentum equation in the super-critical flow case.

The high local differences in the water level are visible in Figure 3.13 (right hand side). The height of the water in the vicinity of the curb is too low with SWE in the super-critical flow case. That is because the vortices in front and behind the curb are not considered. In the 3D application, the local flow behavior is crucial for the assessment of flood risks.

3.3   Need for Extensions

Summarizing the differences between the SWE results and the NSE benchmark solutions for the flow problems *manhole* and *curb* demonstrates the need for extensions:

Flow Problem *Manhole*

There are serious differences between the SWE results and the NSE benchmark solution due to the simplified assumptions of the SWE. In particular the neglect of the vertical momentum from the inflow at the manhole causes too low heights of water column H_c and too low Fr-numbers at x_o. The higher the vertical inflow velocity w_b, the higher are the differences. Such differences can be crucial when assessing the flood risks (e.g. if we have to assess whether the water has enough momentum to jump over a curb or not).

Flow Problem *Curb*

The differences of the water levels for the flow problem *curb* are concentrated to the vicinity of the curb. For the sub-critical flow case, the differences are small and the SWE are applicable in this context. This is different for the super-critical case, where the local behavior at the curb can also be crucial when assessing the flood risks.

Need for Extensions

In particular the flow problem *manhole* can **not** be simulated reliably with the SWE. Vortices and non-zero vertical velocities prevent the applicability when dependable results are required. Thus, there is a demand to derive extensions including flow effects not considered in the classical SWE. Such extensions should

$$\qquad - \text{ be justified physically,} \qquad\qquad\qquad\qquad\qquad (3.12)$$

$$\qquad - \text{ be applicable within the SWE framework,} \qquad\qquad (3.13)$$

$$\qquad - \text{ increase the computational effort only moderately and} \quad (3.14)$$

$$\qquad - \text{ clearly reduce the differences between SWE and NSE results.} \quad (3.15)$$

Studying the NSE benchmark solutions in detail to detect effects influencing the flow behavior not considered in the classical SWE yields in particular

1. the appearance of vortex regions and

2. non-zero material derivatives of the vertical velocity w

Appropriate extensions are derived based on the incorporation of these effects in the next chapters.

Chapter 4

Extension *Vortex Separation*

The comparison between the NSE benchmark solution and the results of the classical SWE in Chapter 3 demonstrates the need for extensions of the SWE. These extensions should fulfill the properties (3.12)-(3.15) discussed in the previous section.

The NSE benchmark solutions for the flow problems *manhole* (Figure 4.1, left) and *curb* (Figure 4.2, left) contain vortices in the flow domain. The Extension *Vortex Separation* assumes that these vortex regions are dead zones not participating in the main flow above. The circulating flow of water inside these regions involves no exchange of water with the main flow in the stationary case. Nevertheless, the vortex regions influence the main flow since the bottom for the main flow above is represented by them. We pose two important questions:

1. How to design the separation line between the vortex region and the main flow domain above ?

2. What are the effects of the separation of the vortex region on the main flow description with SWE ?

Question 1 is answered in Section 4.1 by an empirical design approach based on the availability of the NSE-benchmark solution. This empirical approach is required to assess the quality of the physical design approach derived in Section 4.2. Obviously, the high computational effort of the NSE-solutions can only be avoided by a physical design approach. Section 4.3 describes how to include in-stationary considerations into the stationary design approach of the vortex regions.

The effects of the Extension *Vortex Separation* on the friction approach of the SWE are discussed in Section 4.4. Further answers to Question 2 are presented given within the Extension *Pressure Correction* in Chapter 5.
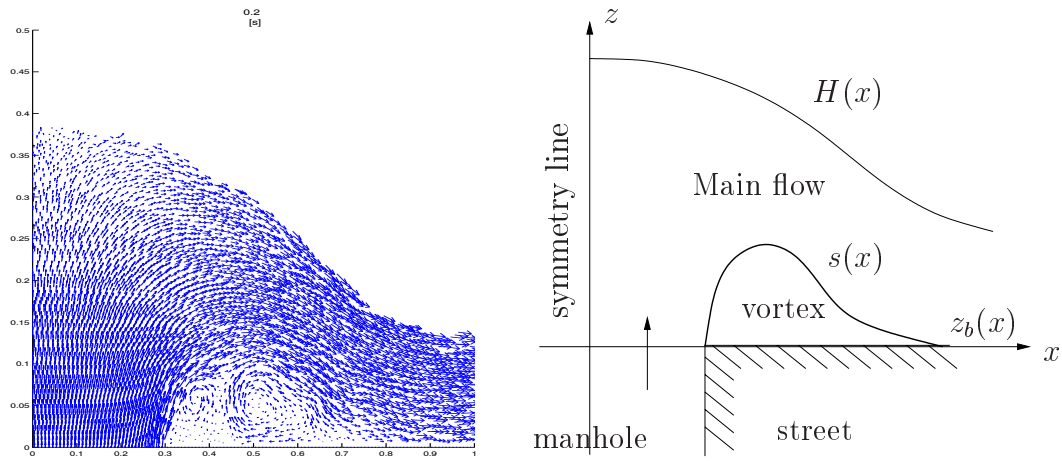
Figure 4.1: NSE benchmark solution and concept of Extension *Vortex Separation* for the flow problem *manhole*
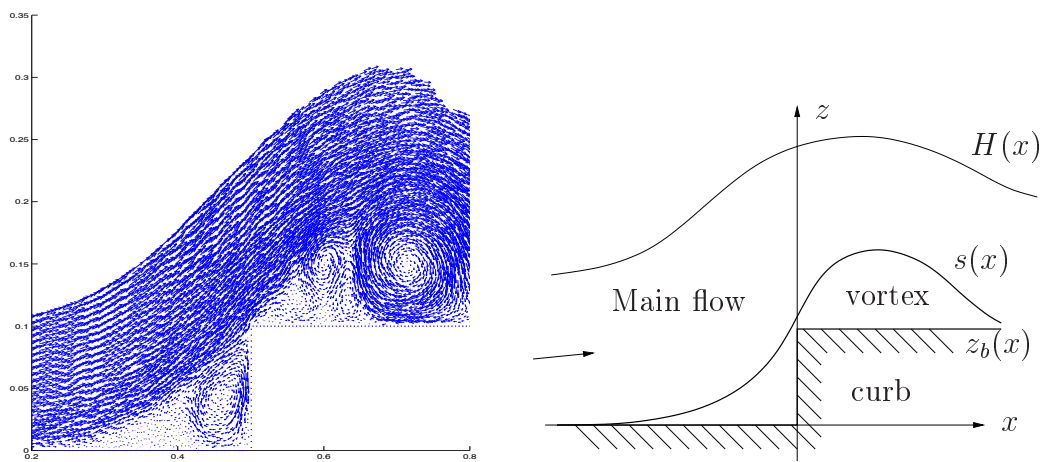

Figure 4.2: NSE benchmark solution and concept of Extension *Vortex Separation* for the flow problem *curb*

4.1 Empirical Design Approach

The concept of separating vortex regions at the bottom near the manhole and the curb is illustrated on the right hand side of Figures 4.1 and 4.2 respectively. The NSE benchmark solutions illustrated on the left hand side of the figures contain vortices in those regions.

The empirical design of the vortex region fits a flow separation line to the NSE solution. The separation line, approximated by a function $s(x)$, represents the upper boundary of the vortex region as well as the new bottom for the main flow above.

The design of the separation line is restricted to smooth fit functions $s(x) \in C^1$ in order to obtain a smooth bottom elevation z_b for the SWE flow above. Furthermore, constraints for the fit function $s(x)$ are postulated due to the observed flow behavior of the NSE solution. The class of possible fit functions $s(x) \in S$ is chosen as polynomials of minimum order fulfilling these constraints.

The separation line $s(x)$ is finally fitted to the NSE result by minimizing a functional $F(s)$ that measures the "quality" (see Definition 4.7) of the parameterized fit function $s(x)$.

4.1.1 Constraints for the Fit Function $s(x)$

Since the vortex regions consist of water, they are obviously located above the given bottom elevation z_b. Thus,

$$s(x) \geq z_b(x) \tag{4.1}$$

is the first constraint for the separation line $s(x)$. The separation line is identical to the bottom $s(x) = z_b(x)$ for regions without vortices. Vortex regions only occur for $s(x) > z_b(x)$ in the "support of the vortex region".

Definition 4.1 (Support of the vortex region) *The set $supp(s - z_b) := \{x \in \mathbb{R} \mid s(x) - z_b(x) > 0\}$ is the support of the nonnegative function of the height of the vortex region $s(x) - z_b(x)$. The smallest closed interval containing this set*

$$[x_s, x_e] := \{\cap_{x,y \in \mathbb{R}}[x, y] | [x, y] \supset supp(s - z_b)\} \tag{4.2}$$

is defined as the "Support of the vortex region".

Considerations of the flow behavior of the NSE benchmark solution yield assumptions for selected points on the separation line $s(x)$ or its slope at selected points.

Flow Problem *Manhole*

As in Chapter 3, we assume the center of the manhole to be located at $x = 0$ and the z-axis to be the symmetry line of the flow. The boundary of the manhole is located at $x = x_m$. The velocity vectors of the NSE benchmark solution on the left hand side of Figure 4.1 allow an estimation of the behavior of the separation line $s(x)$:
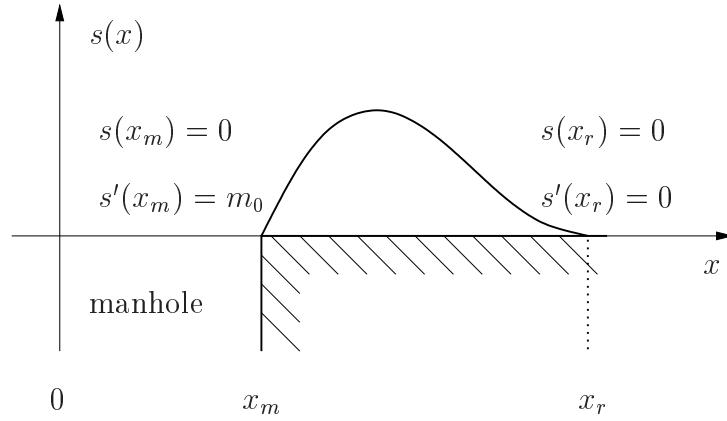
Figure 4.3: Constraints for the empirical design of the separation line for the flow problem *manhole*

The separation line $s(x)$ starts at the boundary of the manhole in $(x_m, 0)$ with a given slope $s'(x_m) = m_0 > 0$ due to the inflow condition. The separation line reaches a maximum at the top of the vortex and decreases until it re-attaches the bottom in the re-attachment point x_r. We assume a zero slope in x_r in order to obtain $s(x) \in C^1$ in x_r. Obviously, the support of the vortex region is $[x_m, x_r]$ and the design of $s(x)$ is restricted to this interval.

These constraints for $s(x)$ illustrated in Figure 4.3 are summarized as:

$$
\begin{array}{lll}
\text{Separation point at } x_m & s(x_m) = 0 & \\
\text{Slope at } x_m \text{ is } m_0 & s'(x_m) = m_0 & \\
\text{Re-attachment point at } x_r & s(x_r) = 0 & (4.3) \\
\text{Slope at } x_r \text{ is } 0 & s'(x_r) = 0 &
\end{array}
$$

The constraints (4.3) pose 4 conditions for $s(x) \geq 0$ for $x \in [x_m, x_r]$ fulfilled by a unique third order polynomial $s(x) = a_3 x^3 + a_2 x^2 + a_1 x + a_0$. The

coefficients a_3, a_2, a_1 and a_0 depend on the values of x_m, x_r and m_0 by:

$$a_3 = \frac{m_0}{(x_m - x_r)^2} \tag{4.4}$$

$$a_2 = \frac{-m_0(2x_r + x_m)}{(x_m - x_r)^2} \tag{4.5}$$

$$a_1 = \frac{m_0 x_r(x_r + 2x_m)}{(x_m - x_r)^2} \tag{4.6}$$

$$a_0 = \frac{-m_0 x_r^2 x_m}{(x_m - x_r)^2} \tag{4.7}$$

Thus, the class of fit functions S is chosen as the set of third order polynomials $s(x) \in \mathbb{P}^3$ fulfilling (4.3), i.e. with the coefficients a_3, a_2, a_1 and a_0 from (4.4) to (4.7).

$$S := \left\{ s(x) | s(x) \begin{cases} \in \mathbb{P}^3 \text{ fulfilling (4.3)} & : & x \in [x_m, x_r] \\ = z_b(x) & : & x \notin [x_m, x_r] \end{cases} \right\} \tag{4.8}$$

Explanation 4.2 *$s(x) \notin C^1$ at the boundary of the manhole in x_m, since $s'(x_m) = m_0 > 0$ and $s(x) = 0 = z_b$ for $x \in [0, x_m]$, the plane manhole area. $S \not\subset C^1$ is accepted for the special point x_m yielding a continuous estimation of vertical velocity w in Chapter 5.*

Remark 4.3 *There exist of course other functions $s(x) \notin S$ but $s(x) \in C^1$ and fulfilling (4.3). For the sake of simplicity the choice of S is reduced to the third order polynomials. Results with this restriction are satisfactory.*

Flow Problem *Curb*

The curb with the step size h_s is located at $x = 0$ with the bottom elevation $z_b = 0$ for $x < 0$ and $z_b = h_s$ for $x > 0$ as illustrated in Figure 4.4. Analogously to the flow problem manhole, constraints for $x \geq 0$ are postulated by an offset of the constraints (4.3) from 0 to h_s:

$$
\begin{array}{lll}
\text{Top of the curb } (0, h_s) \in s(x) & s(0) = h_s & \\
\text{Slope at 0 is } m_0 & s'(0) = m_0 & \\
\text{Re-attachment point at } x_r & s(x_r) = h_s & \\
\text{Slope at } x_r \text{ is } 0 & s'(x_r) = 0 &
\end{array} \tag{4.9}
$$

Again, 4 conditions for $s(x) \geq h_s$ for $x \in [0, x_r]$ determine a unique third order polynomial.

The constraints of $s(x)$ for $x < 0$ are postulated by assuming $s(x) \in C^1$ in $x = 0$ (yielding 2 conditions) and choosing a separation point at x_l as illustrated in Figure 4.4:
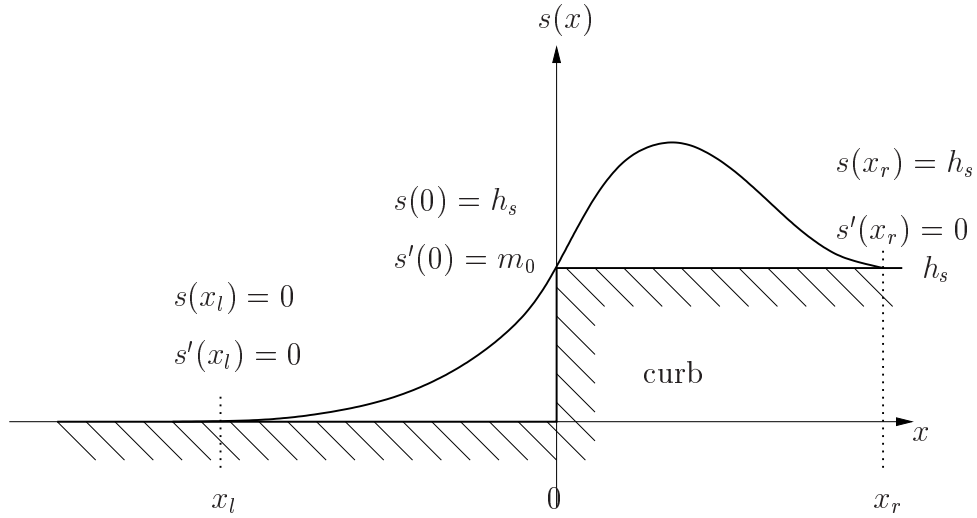
Figure 4.4: Constraints for the empirical design of the separation line for the flow problem *curb*

$$
\begin{array}{ll}
\text{Top of the curb } (0, h_s) \in s(x) & s(0) = h_s \\
\text{Slope at 0 is } m_0 & s'(0) = m_0 \\
\text{Separation point at } x_l & s(x_l) = 0 \\
\text{Slope at } x_l \text{ is 0} & s'(0) = m_0
\end{array}
\tag{4.10}
$$

The unique third order polynomial fulfilling the 4 conditions (4.10) for $x \in [x_l, 0]$ does at times not satisfy (4.1) yielding negative values for $s(x)$. Instead of applying more complicated functions (e.g. $s(x) = \alpha_1 \, cosh(\alpha_2(x + \alpha_3) + \alpha_4, x \in [x_l, 0])$, we reduce $s(x)$ to a 2nd order polynomial for $x \in [x_l, 0]$. This assures (4.1), but a degree of freedom is abandoned by coupling the slope m_0 and the separation point x_l:

$s(x_l) = 0$ and $s'(x_l) = 0$ yields $s(x) = \alpha(x - x_l)^2, \alpha \in \mathbb{R}^+$ for a 2nd order polynomial on $[x_l, 0]$. The other constraints from (4.10) read $s(0) = h_s = \alpha x_l^2$ and $s'(0) = m_0 = -2\alpha x_l$, satisfactory if

$$
m_0 x_l = -2 h_s
\tag{4.11}
$$

is fulfilled.

Explanation 4.4 *The restriction (4.11) reduces the design of $s(x)$ for $x < 0$ to the choice of only one physical parameter m_0 or x_l.*

The physical design approach in Section 4.2 is restricted to $x \geq 0$. The estimation of m_0 entails thus the design for $x < 0$ without any further assumptions. Hence, the following presentation is based on the choice of the slope m_0 as the physical design parameter.

Remark 4.5 *Within the physical design approach in Section 4.2 we consider the separation line $s(x)$ as a trajectory of a water particle. Assuming a constant force acting on the motion of the water particle on the separation line for $x < 0$ yields the parabola form for $s(x) \in \mathbb{P}^2$.*

The design of the vortex region is determined uniquely by the choice of the two parameters x_r and m_0 (respectively x_l, see Explanation 4.4) yielding the class $S \subset C^1$ of fit function $s(x)$:

$$
S := \left\{ s(x) \in C^1(\mathbb{R}) \mid s(x) \begin{cases} \in \mathbb{P}^2 \text{ fulfilling } (4.10) & : \quad x \in [x_l, 0] \\ \in \mathbb{P}^3 \text{ fulfilling } (4.9) & : \quad x \in [0, x_r] \\ = z_b(x) & : \quad \text{else} \end{cases} \right\}
$$
(4.12)

The polynomial coefficients of $s(x) = b_2 x^2 + b_1 x + b_0$ on $[x_l, 0]$ and $s(x) = a_3 x^3 + a_2 x^2 + a_1 x + a_0$ on $[0, x_r]$ depend on the choice of m_0 and x_r due to the postulated constraints in (4.9) and (4.10):

$$
a_3 = \frac{m_0}{x_r^2}, \quad a_2 = \frac{-2m_0}{x_r}, \quad a_1 = m_0, \quad a_0 = h_s \tag{4.13}
$$

$$
b_2 = \frac{m_0^2}{4h_s}, \quad b_1 = m_0, \quad b_0 = h_s \tag{4.14}
$$

The setting of the fit parameters x_r and m_0 entails the determination of the unique separation line $s(x)$.

4.1.2   Fit Procedure

In the previous section we have presented physical constraints for the separation line $s(x)$. These constraints (4.3) for the flow problem *manhole* and (4.9), (4.10) for the flow problem *curb* employ the physical parameters x_r and m_0 describing a re-attachment point and a flow direction observed in the NSE benchmark solution.

To determine its exact values from the NSE solution admits subjective freedoms and is not unique. But it is possible to restrict the parameters to physically relevant intervals and exclude choices far away from the reasonable values. This is done manually yielding, $x_r \in [x_{rl}, x_{rr}]$ and $m_0 \in [m_{0l}, m_{0r}]$.

The assumed constraints are idealizations based on the examination of the NSE benchmark solution. In particular the restriction of the separation line to polynomial fit functions $s(x) \in S$ is physically not necessary and done to avoid complicated computations. Thus, even inserting the correct values from the NSE solution may produce a fit function $s(x)$ not describing the separation line perfectly.

Seeking the best choice of the parameters x_r and m_0 to fit the flow separation line $s(x)$ to the NSE results, an approach of minimizing an error functional $F(s)$ can be applied. $F(s)$ measures the "quality" of the separation line $s(x)$ compared to the NSE solution. Therefore we define "quality" of the separation line $s(x)$ and its quantification. The separation line $s(x)$ is assumed to separate the vortex region from the main flow domain without exchange of water in the stationary solution. $F(s)$ measures the flux across the separation line that is minimal if $s(x)$ is tangential to the velocities $\vec{u}_{NSE}$.

The tangential vector of $s(x)$ is obtained by the slope $s'(x)$ as

$$\vec{t}_{s(x)} = \begin{pmatrix} 1 \\ s'(x) \end{pmatrix}, \tag{4.15}$$

determining also the unit normal vector $\vec{n}_{s(x)}$ perpendicular to $\vec{t}_{s(x)}$

$$\vec{n}_{s(x)} = \frac{1}{\sqrt{1 + (s'(x))^2}} \begin{pmatrix} -s'(x) \\ 1 \end{pmatrix} \tag{4.16}$$

as illustrated in Figure 4.5.
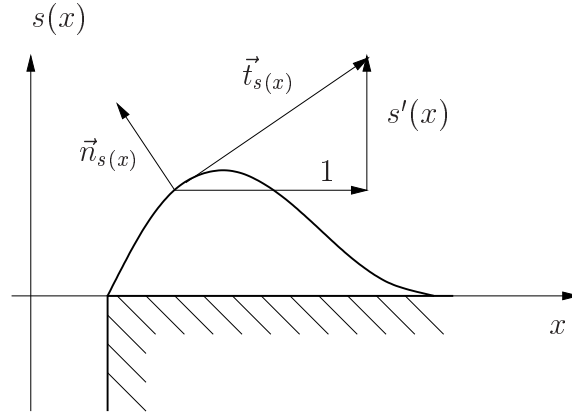
Figure 4.5: Tangential vector $\vec{t}_{s(x)}$ and normal vector $\vec{n}_{s(x)}$ on $s(x)$

The inner product $\vec{n}_{s(x)} \cdot \vec{u}_{NSE}(x)$ quantifies the flux of the NSE flow across the separation line $s(x)$ at x. Integrating the norm of that flux across the separation line $s(x)$ yields the total flux $flux(s)$ across the line:

$$flux(s) = \int_{\mathbb{R}} |\vec{n}_{s(x)} \cdot \vec{u}_{NSE}| \, dx \tag{4.17}$$

For $s(x) = z_b(x)$ there is no contribution to $flux(s)$ due to the assumption of no penetration of water in the bottom as kinematic boundary condition. Thus, the integration over $\mathbb{R}$ can be reduced to an integration over the support of the vortex region $[x_s, x_e]$ (see Definition 4.1).

Remark 4.6 *A minimization approach for $flux(s)$ results in $s(x) = z_b(x)$ everywhere without any vortex region and $flux(s) = 0$.*

The suitable quality measure $F(s)$ determines the flux across $s(x)$ per unit length. $flux(s)$ from (4.17) is divided by the length of $s(x)$ in the support of the vortex region assumed to be nonempty.

Definition 4.7 *Let $\vec{u}_{NSE}(x, z)$ be the given velocity vectors of the NSE benchmark solution. The "quality" of a separation line $s(x)$ is defined by the flux across $s(x)$ per unit length on the support of the vortex region $[x_s, x_e] \neq \{\}$:*

$$F(s) = \frac{1}{\int_{x_s}^{x_e} \sqrt{1 + (s'(x))^2}\ dx} \int_{x_s}^{x_e} |\vec{n}_{s(x)} \cdot \vec{u}_{NSE}(x, s(x))|\ dx \qquad (4.18)$$

$s(x)$ can be determined by minimizing $F(s)$ within a multi-parameter minimization under constraints

$$\min_{\substack{x_r \in [x_{rl}, x_{rr}] \\ m_0 \in [m_{0l}, m_{0r}]}} \{F(s)|s(x) \in S\}. \qquad (4.19)$$

Remark 4.8 *Since the empirical design is only needed for the assessment of the results of the physical design, the efforts of such a minimization process are avoided. Instead, the allowed intervals for the fit parameters are restricted to small intervals and finally chosen by comparing $F(s)$ obtained by several test calculations.*

4.1.3   Results with Empirical Design Approach

The results of the empirical design approach are illustrated in Figures 4.6 (three figures for three inflow velocities) and 4.7 for the flow problem manhole and curb respectively. The fitted separation line $s(x)$ is plotted in green and the resulting water level from the stationary SWE-solution above the separated vortex region is plotted in red. The NSE velocity vectors, illustrated as arrows in the background, allow an assessment of the separation qualities of $s(x)$. This yields reasonable agreements although $\min F(s) > 0$.

Figure 4.6: Results of the empirical design approach for $s(x)$ (green line) with stationary SWE water level H (red line) and NSE velocities in the background for the flow problem *manhole* with different inflow velocities (from top to bottom: $w_b = 1m/s$, $w_b = 2m/s$, and $w_b = 3m/s$)
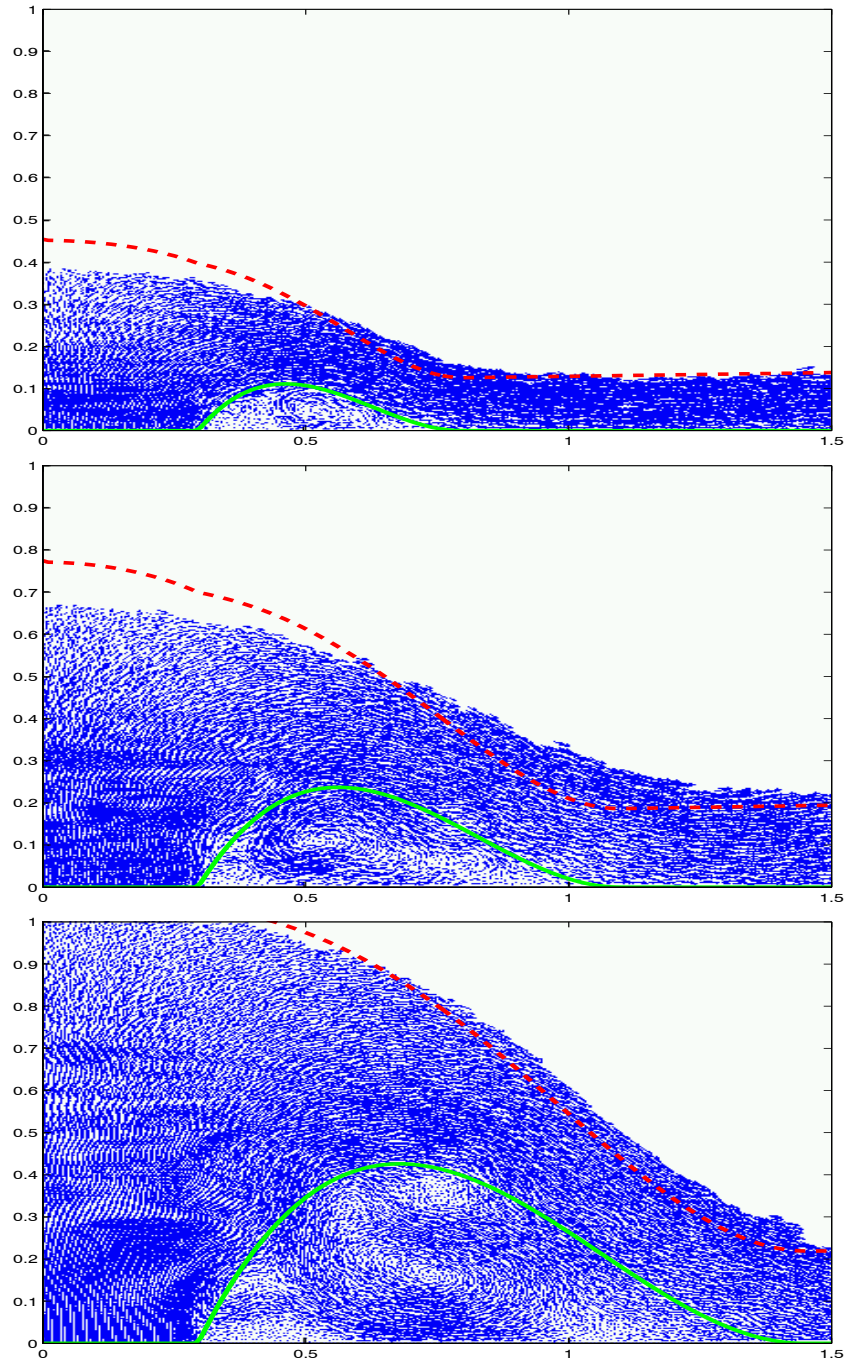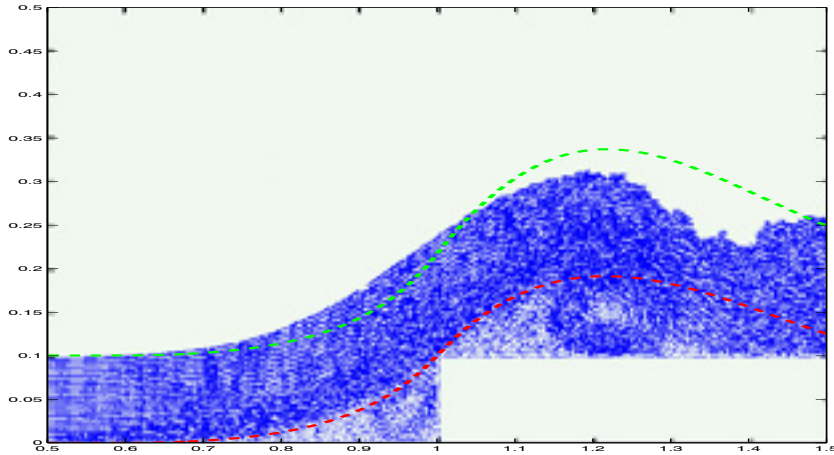
Figure 4.7: Results of the empirical design approach for $s(x)$ (green line) with stationary SWE water level H (red line) and NSE velocities in the background for the flow problem *curb* with inflow velocity $u_0 = 3m/s$

4.2 Physical Design Approach

There are two severe disadvantages in the empirical design approach for $s(x)$:

1. The computational effort is not reduced since the computation of the NSE solution is still required.

2. The design approach is restricted to polynomials performing special constraints.

We derive a physical design approach finally executable without these disadvantages. This approach departs from the concept of a minimum flux across the separation line.

4.2.1 Concept of Trajectory

The functional $F(s)$ (4.18) quantifies the flux of the NSE flow across the separation line $s(x)$ per unit length. $F(s)$ is applied as a quality measure since $s(x)$ is expected to separate the vortex region and the main flow. The separation line $s(x)$ obtained with this approach is locally almost tangential to the velocity vectors $\vec{u}_{NSE}$ in the vicinity, as shown in Figures 4.6 and 4.7.

Applying the trajectory of one water particle in the NSE flow as the separation line $s(x)$ assures that $\vec{u}_{NSE}(x)$ is collinear to $\vec{t}_{s(x)}$ and thus perpendicular to $\vec{n}_{s(x)}$. This yields a zero flux across $s(x)$ with $F(s) = 0$. This holds for every trajectory in a stationary flow. $s(x)$ is chosen as the particular trajectory of a selected water particle to be defined below for each flow problems.

The 2D-NSE solution contains $u_{NSE}(x,z)$ and $w_{NSE}(x,z)$ for all (x,z) in the flow domain. A water particle in the stationary flow moves due to the ODE system

$$\begin{pmatrix} \dot{x} \\ \dot{z} \end{pmatrix} = \begin{pmatrix} u_{NSE} \\ w_{NSE} \end{pmatrix}. \tag{4.20}$$

The initial conditions for the first order ODE system are given by the selected water particle defining the appropriate trajectory

$$(x(\tau = 0), z(\tau = 0)) = (x_0, z_0). \tag{4.21}$$

Remark 4.9 *We design $s(x)$ for stationary solutions. The ODE system (4.20) describes a time-dependent motion of a water particle on streamlines in the stationary solution. Since the variable t is reserved for the time in the flow description with NSE, we define a new time variable τ for the solution of the ODE (4.20). τ denotes the time within the motion of a water particle in the stationary NSE solution.*

For the flow problem *manhole*, we choose the water particle at the boundary of the manhole. For the flow problem *curb*, we choose the water particle touching the top of the curb:

$$(x_0, z_0) = (x_m, 0) \quad , \text{flow problem } \textit{manhole} \tag{4.22}$$
$$(x_0, z_0) = (0, h_s) \quad , \text{flow problem } \textit{curb} \tag{4.23}$$
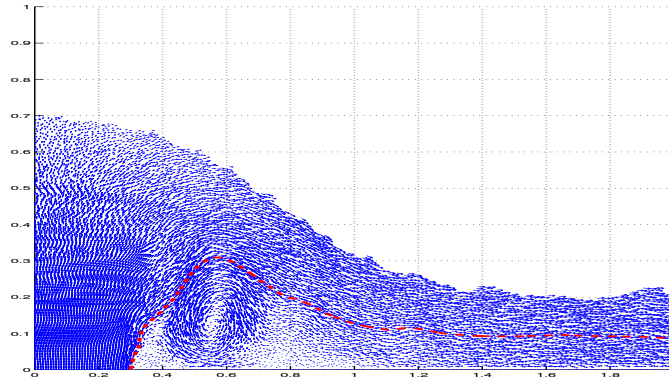

Figure 4.8: Design of $s(x)$ as a trajectory of a selected water particle in the stationary NSE-benchmark solution for the flow problem *manhole*

The trajectory $s(x)$ from that design approach is the pathline $(x(\tau), z(\tau))$ obtained as solution of (4.20) with the initial conditions (4.23). For the flow problem *manhole*, $s(x)$ is illustrated in Figure 4.8.

The trajectory is not as smooth as obtained by the empirical design, where the fit polynomials assure the smoothness and regularity of $s(x)$. That is due to the fact that the NSE solution is not really stationary and we have selected a particular solution as stationary solution. Thus, $s(x)$ varies for different selected NSE solutions. Furthermore, the vortex region is reproduced only poorly since the flow is not re-attached to the bottom.

For the flow problem *curb*, this design approach fails since the NSE velocity $\vec{u}_{NSE}(0, h_s) = \vec{0}$ due to the no-slip condition at the bottom.

Thus, the results of this physical design approach are neither convincing nor possible without the NSE solution. We simplify the approach below.

4.2.2 Simplified Equations of Motion

Instead of considering the flow velocities $\vec{u}_{NSE}$ from the NSE solution, the equations of motion of the water particle (4.20) are simplified. $u_{NSE}(x, z)$ is replaced by the depth-averaged horizontal velocity $u_{SWE}(x)$ from the SWE in each cross section x

$$u(x, z) = u_{SWE}(x) \quad \text{for all } z \in [z_b(x), H(x)]. \tag{4.24}$$

This yields

$$\begin{pmatrix} \dot{x} \\ \dot{z} \end{pmatrix} = \begin{pmatrix} u_{SWE}(x) \\ w \end{pmatrix}. \tag{4.25}$$

Since the vertical velocity w is not considered in SWE, we approximate w by solving a further ODE of the equations of motion. Newton's second law of motion for the vertical z-direction reads

$$\ddot{z} = \dot{w} = f_z, \tag{4.26}$$

claiming that the vertical acceleration is identical to the sum of all forces in vertical direction per unit mass f_z. We consider the gravity force $-g$ as the dominant force the z-direction and neglect all other forces, and obtain

$$\dot{w} = -g. \tag{4.27}$$

(4.25) and (4.27) are the idealized equations of motion for the trajectory of the water particle

$$\begin{pmatrix} \dot{x} \\ \dot{z} \\ \dot{w} \end{pmatrix} = \begin{pmatrix} u_{SWE} \\ w \\ -g \end{pmatrix}. \tag{4.28}$$

The initial conditions (x_0, z_0) from (4.23) have to be completed by an initial condition for w.

4.2.3   Initial Conditions for the Trajectory

The initial conditions for the flow problems *manhole* and *curb* for the first two equations of (4.28) are already given in (4.22) and (4.23) respectively. w_0 denotes the initial vertical velocity at the initial point (x_0, z_0).

For the **flow problem *manhole***, this vertical velocity w_0 is simply given by the inflow condition from the manhole

$$w_0 = q. \tag{4.29}$$

Figure 4.9: Initial conditions for physical design of the separation line for the vortex region as a trajectory for the flow problem *manhole*

Figure 4.9 illustrates the initial conditions for the trajectory of the flow problem *manhole*.

Since no initial vertical velocity is given explicitly for the **flow problem *curb***, w_0 is estimated by considering the energy conservation. The kinetic energy of a water particle approaching the curb with the horizontal velocity u_0 is $u_0^2/2$. That holds also for a water particle close to the bottom above the small viscous bottom layer.

We assume that this water particle is lifted up the curb from $z = \delta z \approx 0$ to $z = h_s$ and a part of the kinetic energy turns into potential energy. Assuming energy conservation yields the absolute velocity $|\vec{u}|$ at the top of the curb in $(0, h_s)$ as

$$|\vec{u}| = \sqrt{u_0^2 - 2gh_s}. \tag{4.30}$$

Since $|\vec{u}| = |(u,w)^T| = \sqrt{u^2 + w^2} = \sqrt{u_{SWE}(0)^2 + w_0^2}$, we obtain

$$w_0 = \sqrt{(u_0^2 - 2gh_s)^2 - u_{SWE}(0)^2}. \tag{4.31}$$

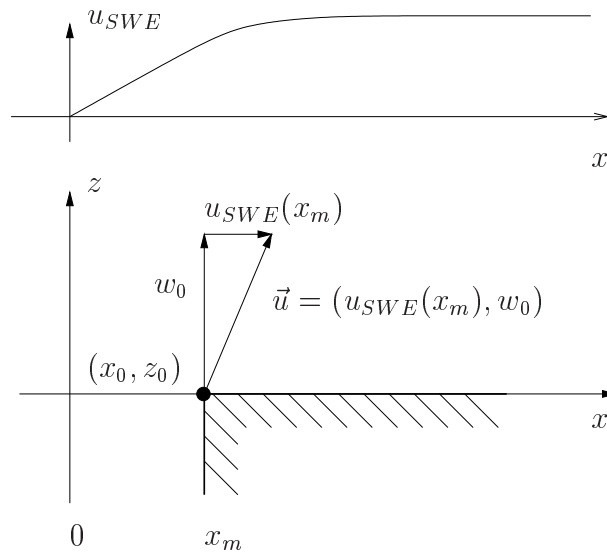Figure 4.10 illustrates the initial conditions for the trajectory of the flow problem *curb*.
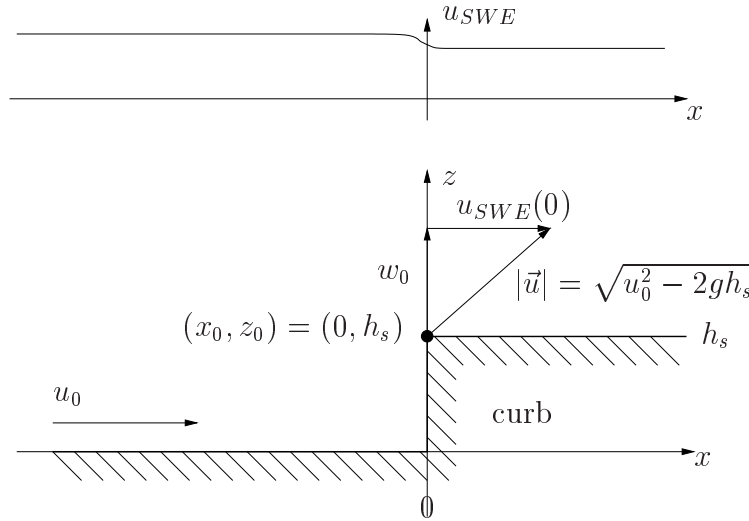
Figure 4.10: Initial conditions for physical design of the separation line for the vortex region as a trajectory for the flow problem *curb*

Following the trajectory of the water particle back in time for the design of $s(x)$ for $x < 0$ requires also an ODE for w similar to (4.27). Obviously, the forces due to pressure are higher than the gravity force yielding a lift of the water particle. In order to avoid the difficult task to approximate the pressure and its gradient in front of the curb and possibly further forces, we apply parts of the empirical design approach from the previous section.

The initial condition $w_0 = w(\tau = 0)$ together with the horizontal velocity $u_{SWE}(x = 0) = u(\tau = 0)$ from the SWE solution yields a velocity vector

$$\vec{u}(x = 0) = \begin{pmatrix} u_{SWE}(0) \\ w_0 \end{pmatrix} \tag{4.32}$$

in the starting point of the trajectory $(x_0, z_0) = (0, h_s)$. For the slope of the trajectory in that point, we obtain

$$m_0 = w_0 / u_{SWE}(0). \tag{4.33}$$

We insert this slope in (4.11) from the empirical design approach for $x < 0$ and obtain the separation point $x_l = -2h_s/m_0$ and a uniquely determined $s(x) \in \mathbb{P}^2$.

4.2.4   Iteration Process

$u_{SWE}(x)$ in (4.28) is considered the stationary horizontal flow velocity over the already separated vortex region. Since the design of the vortex region influences the stationary SWE solution and in particular u_{SWE}, the problem is implicit, and solved by a fix-point iteration process.

Start of Iteration

We start the iteration without any vortex region setting $s^{(0)}(x) = z_b(x)$.

Iteration Step 1

We solve the stationary 1D-SWE flow problem for $s^{(0)}(x) = z_b(x)$:

$$\frac{\partial}{\partial x} \begin{pmatrix} u^{(0)} h^{(0)} \\ (u^{(0)})^2 h^{(0)} + \frac{1}{2} g (h^{(0)})^2 \end{pmatrix} = \begin{pmatrix} q \\ g h^{(0)} \left(\frac{-\partial s^{(0)}(x)}{\partial x} - S_{fx} \right) \end{pmatrix}. \qquad (4.34)$$

This yields $(u^{(0)}_{SWE} = u^{(0)}, h^{(0)}_{SWE} = h^{(0)})$, the stationary results from the classical SWE presented in Chapter 3.

The second stage in the first iteration step is the evaluation of $s^{(1)}(x)$ by solving (4.28) with $u^{(0)} = u^{(0)}_{SWE}$ from above.

$$\begin{pmatrix} \dot{x}^{(1)} \\ \dot{z}^{(1)} \\ \dot{w} \end{pmatrix} = \begin{pmatrix} u^{(0)} \\ w \\ -g \end{pmatrix}. \qquad (4.35)$$

We note, that not only the first component on the right hand side of (4.35) is influenced by $u^{(0)} = u^{(0)}_{SWE}$, but also the initial conditions due to (4.31).

The integration (e.g. numerically with an explicit Euler scheme) yields a time (τ) parameterized trajectory $(x^{(1)}(\tau), z^{(1)}(\tau))^T$. Since $s^{(1)}(x)$ is a function defined for $x \in \Omega \subset \mathbb{R}$ and not for τ, a transformation between x and τ is required. Assuming $u^{(0)} > 0$ for all x, the mapping

$$T : [0, \tau_e] \to [x(0), x(\tau_e)], \quad T(\tau) = x^{(1)}(\tau) \qquad (4.36)$$

is bijective and the inversion

$$T^{-1} : [x(0), x(\tau_e)] \to [0, \tau_e], \quad T^{-1}(x^{(1)}(\tau)) = \tau \qquad (4.37)$$

exists uniquely. $s^{(1)}(x)$ can be evaluated for $x \in [x(0), x(\tau_e)]$ by applying T^{-1}

$$s^{(1)}(x) = z^{(1)}(T^{-1}(x)).$$

Due to the constraint (4.1), $s(x)$ is cut by the bottom z_b

$$s^{(1)}(x) = max(z^{(1)}(T^{-1}(x)), z_b(x)) \tag{4.38}$$

and a first iteration $s^{(1)}(x)$ of the separation line $s(x)$ is obtained.

Iteration Step n

For a given separation line $s^{(n)}(x)$, the suitable 1D-SWE flow solution $u^{(n)}_{SWE}$ is computed by solving

$$\frac{\partial}{\partial x} \begin{pmatrix} u^{(n)} h^{(n)} \\ (u^{(n)})^2 h^{(n)} + \frac{1}{2} g (h^{(n)})^2 \end{pmatrix} = \begin{pmatrix} q \\ gh^{(n)}(\frac{-\partial s^{(n)}(x)}{\partial x} - S_{fx}) \end{pmatrix}. \tag{4.39}$$

As in the first iteration step for $n = 0$, we estimate the new trajectory as the solution of

$$\begin{pmatrix} \dot{x}^{(n+1)} \\ \dot{z}^{(n+1)} \\ \dot{w} \end{pmatrix} = \begin{pmatrix} u^{(n)} \\ w \\ -g \end{pmatrix}. \tag{4.40}$$

with the initial conditions

$$\begin{pmatrix} x(\tau = 0) \\ z(\tau = 0) \\ w(\tau = 0) \end{pmatrix} = \begin{pmatrix} x_m \\ 0 \\ q \end{pmatrix}, \tag{4.41}$$

for the flow problem *manhole*, and

$$\begin{pmatrix} x(\tau = 0) \\ z(\tau = 0) \\ w(\tau = 0) \end{pmatrix} = \begin{pmatrix} 0 \\ h_s \\ \sqrt{(u_0^2 - 2gh_s)^2 - (u^{(n)}(0))^2} \end{pmatrix} \tag{4.42}$$

for the flow problem *curb*.

Remark 4.10 *There exist $x \in \Omega$ with $s^{(n+1)}(x) < s^{(n)}(x)$ within the iteration process, i.e. when the design of the separation line $s^{(n+1)}$ is below $s^{(n)}$. Since the computed horizontal velocity $u^{(n)}_{SWE}$ is the average velocity in the cross section $s^{(n)}(x) \leq z \leq H^{(n)}(x)$, a horizontal velocity u for $z_b(x) \leq z \leq s^{(n)}(x)$ is required. According to (4.24), we apply also $u^{(n)}_{SWE}(x)$.*

As in the first iteration step, we have to re-parameterize the trajectory from time to space by the inversion T^{-1} of the bijective mapping T.

$s^{(n+1)}(x)$ is finally obtained by cutting it with the given bottom elevation $z_b(x)$ as done in (4.38).

Thus, the iteration process contains two stages:

1. Solving the stationary 1D-SWE for a given bottom $s^{(n)}(x)$.

2. Determination of the trajectory $s^{(n+1)}(x)$ by solving (4.40).

Convergence of the Iteration Process

Flow Problem *Manhole*

Applying this iteration process to the flow problem *manhole*, the trajectory $s(x) = \lim_{n \to \infty} s^{(n)}(x)$ lead to numerical convergence after only a few iteration steps. Figure 4.11 illustrates the first steps of the iteration process for $w_b = 2m/s$.
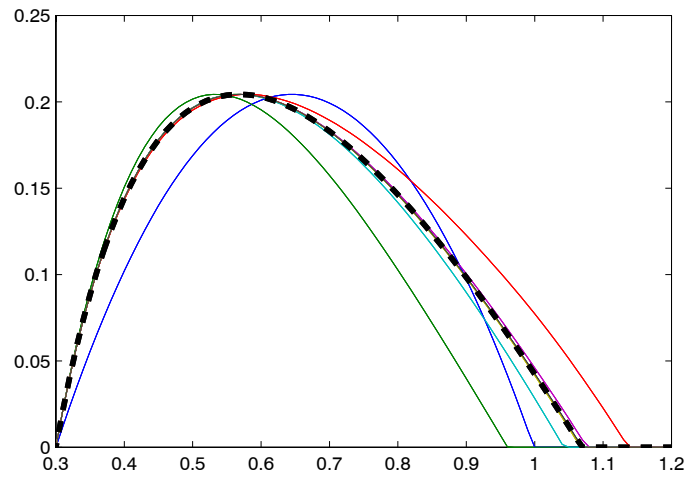
Figure 4.11: First iteration steps $s^{(n)}(x), n = 1$ (blue), 2 (green), 3 (red), 4 (cyan), 5 (magenta), 6 (yellow), 7 (black) and converged separation line $s(x)$ (black dashed line) for the flow problem *manhole*

We consider $s(x)$ as a time-parameterized curve

$$\begin{pmatrix} x \\ s(x) \end{pmatrix} = \begin{pmatrix} s_x(\tau) \\ s_z(\tau) \end{pmatrix} = \begin{pmatrix} x(\tau) \\ z(\tau) \end{pmatrix}. \tag{4.43}$$

For the flow problem *manhole*, $s_z(\tau)$ is independent of the iteration. We consider only the last two components of (4.40), yielding

$$\begin{pmatrix} \dot{z}^{(n+1)} \\ \dot{w} \end{pmatrix} = \begin{pmatrix} w \\ -g \end{pmatrix}, \tag{4.44}$$

with the initial conditions

$$\begin{pmatrix} z^{(n+1)}(\tau = 0) \\ w(\tau = 0) \end{pmatrix} = \begin{pmatrix} 0 \\ q \end{pmatrix}. \tag{4.45}$$

Obviously, (4.44) and (4.45) are independent of the iteration process and can be solved explicitly, yielding

$$\begin{pmatrix} z(\tau) \\ w(\tau) \end{pmatrix} = \begin{pmatrix} w_b\tau - \frac{1}{2}g\tau^2 \\ w_b - g\tau \end{pmatrix} \qquad (4.46)$$

for all iteration steps n.

This represents a parabola form of $s_z(\tau)$ with the maximum s_{max} at τ_{max}

$$s_z(\tau_{max}) = s_z(\frac{w_b}{g}) = s_{max} = \frac{w_b^2}{2g}. \qquad (4.47)$$

The time-parameter τ_e of the re-attachment point of $s_z(\tau_e) = 0$ is also uniquely determined as

$$\tau_e = \frac{2w_b}{g}, \qquad (4.48)$$

yielding the compact time-parameter interval $\tau \in [0, \tau_e]$.

Thus, the second stage of the iteration process is reduced to the first component $s_x(\tau)$ of (4.40), where $u(x)$ determines by the parameterized mapping T between τ and x as defined in (4.36).

$$\dot{x} = u^{(n)} \quad , \text{with} \quad x(\tau = 0) = x_m. \qquad (4.49)$$

The solution of (4.49) is uniquely determined

$$s_x^{(n)}(\tau) = T(\tau) = x^{(n)}(\tau) = x_m + \int\limits_0^\tau u^{(n)}(x^{(n)}(\tilde{\tau})) \, d\tilde{\tau}. \qquad (4.50)$$

Since $u^{(n)} > 0$ we can invert T and obtain

$$\tau(x) = T^{-1}(x). \qquad (4.51)$$

Inserting (4.51) in (4.46) yields

$$s(x) = s_z(\tau(x)) = s_z(T^{-1}(x)) = w_b T^{-1}(x) - \frac{1}{2}g(T^{-1}(x))^2. \qquad (4.52)$$

Thus, the design of $s(x)$ is scaled in the x-dimension by the mapping T determined by the velocity $u(x)$. The reason why the process converges is obviously the fact, that this scaling of the separation line $s(x)$ influences the solution of the stationary SWE only moderately that convergence is enabled.

Remark 4.11 *We have tested the iteration process for several values of w_b, and obtained always convergence within the first iteration steps. Instead of proofing convergence we apply the numerical results for $s(x)$ to compute solutions for the extended SWE, and compare them to the empirical design approach.*

Flow Problem *Curb*

The initial condition w_0 of the flow problem *curb* depends on u_{SWE}, and is thus also involved in the iteration process. The convergence for $u_0 = 3m/s$ requires some more iteration steps.

If u_0 is chosen too small, there is no convergence for $s(x)$. The first iteration steps produce $s(x)$ as a kind of wall at the curb and then fails. The existence of such a limit $u_0 > u^*$ has already been observed in the NSE solutions and in the analytical Euler solutions.

4.2.5 Results with Physical Design Approach

Figure 4.12: Results of the physical design approach for $s(x)$ (green line) with stationary SWE water level H (red line) and NSE velocities in the background for the flow problem *curb* with inflow velocities $u_0 = 3m/s$

Figure 4.13: Comparison of design of $s(x)$ and the water levels (Benchmark dashed black): empirical (blue), physical (green) and physical with S_{p_c} (red) for the flow problem *manhole* with inflow velocities $w_b = 1m/s$ (left) $w_b = 2m/s$ (middle) and $w_b = 3m/s$ (right)

The results of the physical design approach are illustrated in Figures 4.14 (three figures for three inflow velocities) and 4.12 for the flow problem *manhole* and *curb* respectively.
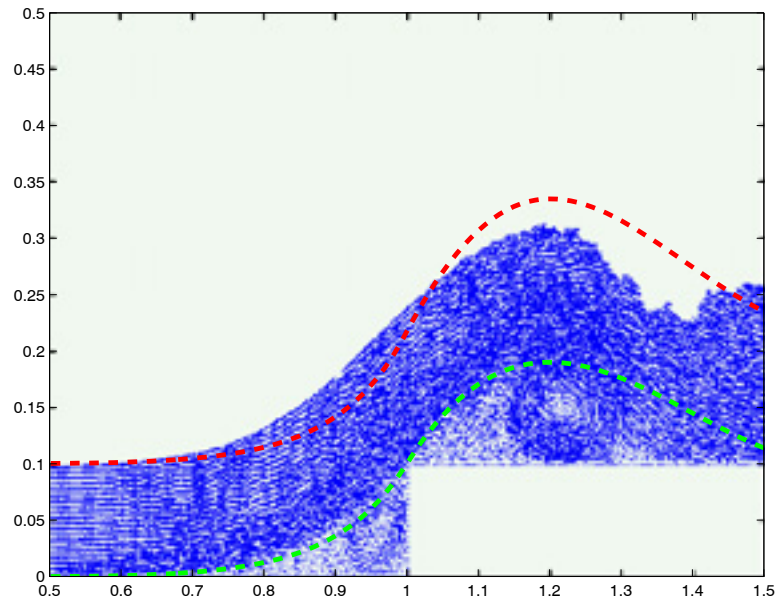
Figure 4.14: Results of the physical design approach for $s(x)$ (green line) with stationary SWE water level H (red line) and NSE velocities in the background fo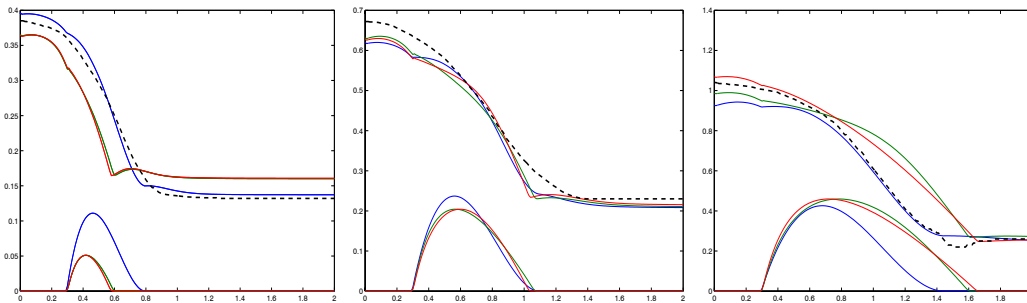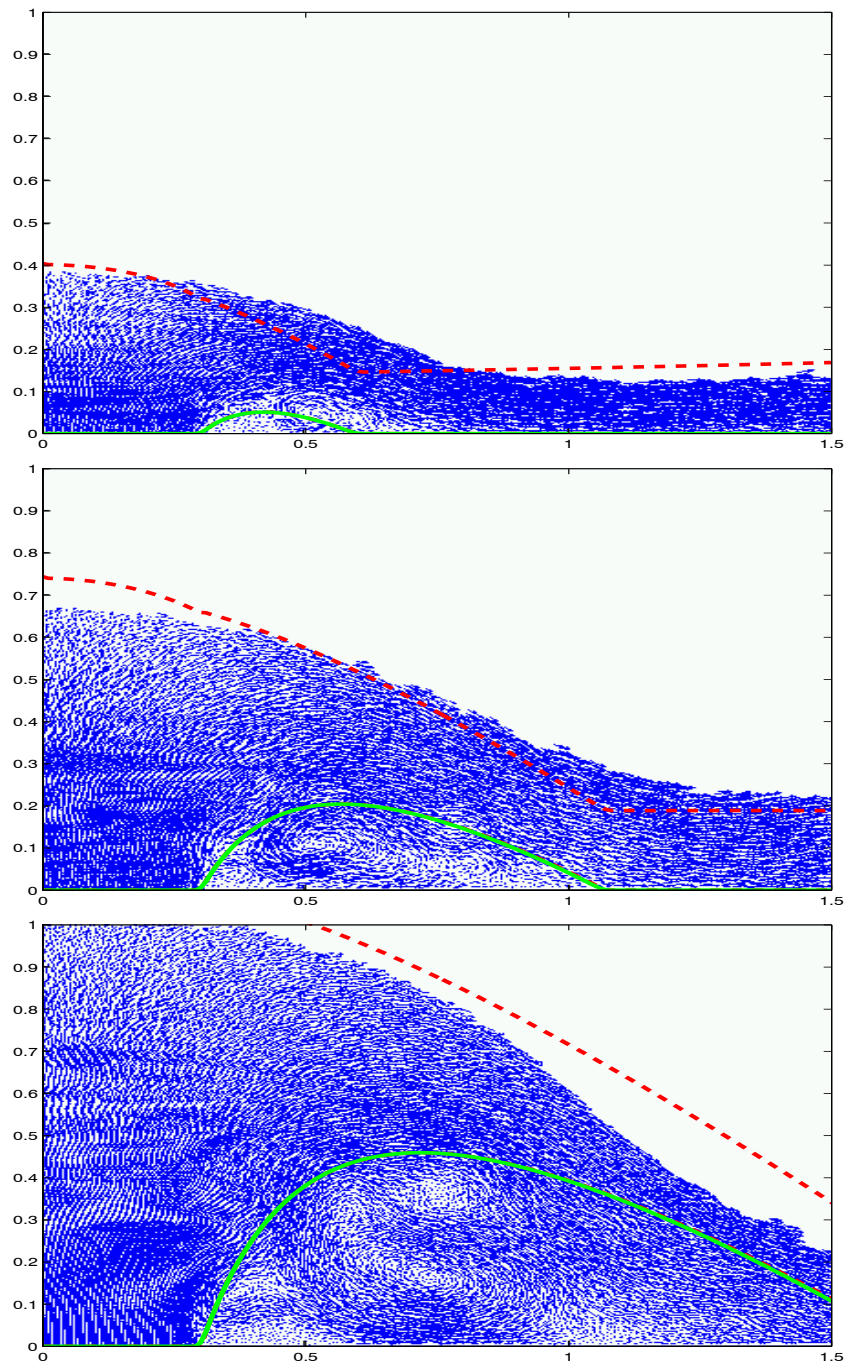r the flow problem *manhole* with different inflow velocities (from top to bottom: $w_b = 1m/s$, $w_b = 2m/s$, and $w_b = 3m/s$)

The computed separation line $s(x)$ is plotted in green and the resulting water level from the stationary SWE-solution above the separated vortex region is plotted in red. The NSE velocity vectors, illustrated as arrows in the background, allow an assessment of the separation qualities of $s(x)$.

The water levels are closer to the benchmarks, but the differences are generally higher than with the empirical design.

4.2.6   Forces on the Water Particle

For the flow problem *curb*, the physical and empirical designs of $s(x)$ are close to each other for $u_0 = 3m/s$. For the flow problem *manhole* these designs of $s(x)$ and the appropriate water levels H are compared to the benchmark solution in Figure 4.13.

The designs are close together for $w_b = 2m/s$. But for $w_b = 1m/s$ the vortex region from the physical design is estimated too small (almost a factor of 2) and for $w_b = 3m/s$ it is slightly too big. The reason for these differences is the neglect of some forces in the approximation of the stationary equations of motion (4.27) where only the gravity force $f = -g$ is included. Consideration of additional forces for the water particle on the trajectory $s(x)$ yields modified designs of the trajectories and thus of $s(x)$.
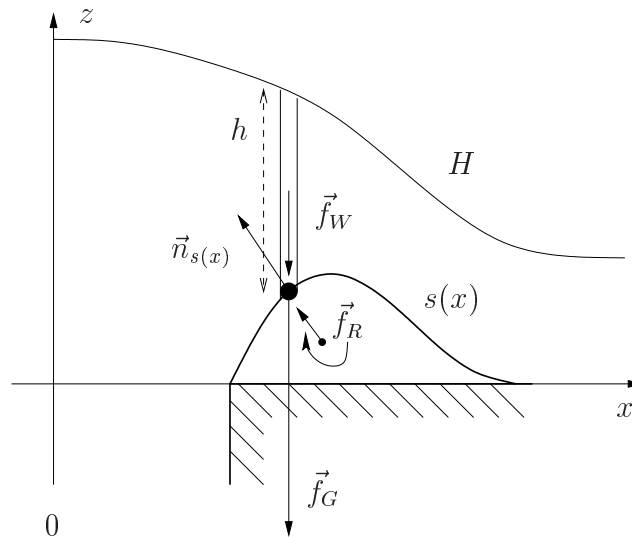
Figure 4.15: Sketch of forces acting on the water particle on the trajectory $s(x)$

Considering forces per unit mass (i.e. accelerations), the sizes of the z-component f of the force $\vec{f}$ are estimated. Figure 4.15 illustrates these forces.

- The water particle flows in the earth gravity field. The pertaining earth acceleration $f_G = -g$ is already included in the equation for $\dot{w}$ in (4.27).

- The water column with the height $h(x) = H(x) - s(x)$ causes a force due to pressure on the particle. The force $f_W = -gh$ acts in the same direction as the gravity force f_G.

- The pressure correction quantified in the next chapter also effect an additional force and yields a correction of $f_W = -(g + \tilde{g})h$ with $\tilde{g}$ from (5.37).

- The rotating water motion in the vortex region causes a centrifugal force $f_R = v^2/r$ in normal direction $\vec{n}_{s(x)}$. v is given by the flow velocity and r by the size of the vortex region.

For the small outflow velocity w_b, the rotation of the vortex produces a force enlarging the designed vortex (e.g. for $w_b = 1m/s$, where the design is too small). For high outflow velocities, the force of the water column above the vortex region and its dynamics down-sizes the designed vortex (e.g. for $w_b = 3m/s$, where the design is slightly too large).

Even if these considerations are reasonable, the iteration process with the additional forces did not lead to convergence.

4.3   Considerations of In-Stationary Flow

The dimensions of the vortex region depend on the main flow above, in particular on the vertical inflow velocity w_b for the flow problem *manhole* and the horizontal velocity u_0 for the flow problem *curb*. In the application to flood problems in urban areas it is to be expected that these values are varying in time. In-stationary flow behavior with varying w_b respectively u_0 changes the size of the separated vortex region over time.

Thus, the stationary consideration of the previous sections is extended to in-stationary flow behavior. Assuming only slight changes of the main flow allows to consider the flow as quasi-stationary and to apply the designed vortex regions for the actual flow values from the stationary consideration. Thus, the in-stationary approach for the Extension *Vortex Separation* involves a time dependent bottom $s(x, t)$ for the main flow. Changes of the dimensions of the vortex region are realized by an exchange of water with the main flow, obviously influencing the main flow.

4.3.1   Dependencies of the Vortex Regions on the Flow Behavior

The design of the vortex region for the flow problem *manhole* depends on the vertical inflow velocity w_b as illustrated in Figure 4.16. The size of the vortex region increases with the inflow velocity w_b, consistent with expectations and the NSE results.

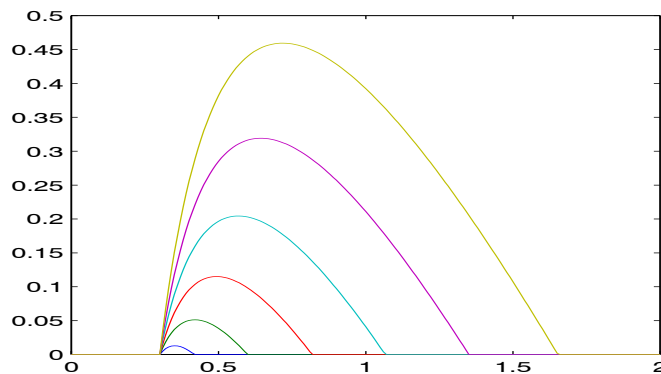Figure 4.16: Dependency of $s(x)$ for different vertical inflow velocities w_b for the flow problem *manhole* ($w_b = 0.5m/s$ (blue line close to the bottom), $1m/s$ (green line), $1.5m/s$, $2m/s$, $2.5m/s$, $3m/s$ (yellow line at top of all lines))

The Extension *Vortex Separation* for the flow problem *curb* is applicable only for high Fr-numbers in super-critical flow cases. The designs of the vor-

tex region for the inflow velocities $u_0 = 3m/s, 4m/s$ and $5m/s$ are illustrated in Figure 4.17. The slope $s'(0)$ of the separation line at the the curb is decreasing with the inflow velocity u_0 and the distances of the separation and re-attachment points to the curb are increasing also, and thus also the size of the vortex region.
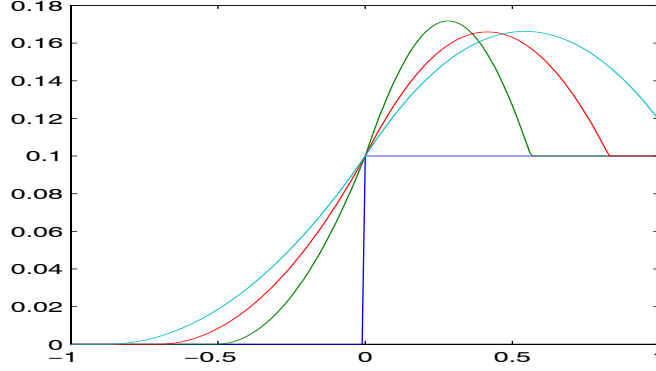
Figure 4.17: Dependency of $s(x)$ for different horizontal inflow velocities u_0 for the flow problem *curb* ($u_0 = 3m/s$ (green), $4m/s$ (red) and $5m/s$ (cyan))

The dependency of $s(x)$ on the flow parameters w_b and u_0 is denoted with s_{w_b} and s_{u_0}. The stationary designs are applied for quasi-stationary design approaches. According to the actual value of $w_b(t)$ and $u_0(t)$, the design of $s(x)$ is updated, denoted as:

$$\begin{aligned} s(x,t) &= s_{w_b(t)}(x) \quad \text{, flow problem } \textit{manhole} \\ s(x,t) &= s_{u_0(t)}(x) \quad \text{, flow problem } \textit{curb} \end{aligned} \tag{4.53}$$

4.3.2 Effects of In-Stationary $s(x,t)$ on the Equations of Motion

The classical SWE approach is derived for a fixed bottom $z_b(t,x,y) = z_b(x,y)$ not varying in time. Thus, all terms with time derivatives of the bottom $\partial z_b/\partial t$ are canceled in the derivation. Due to the Extension *Vortex Separation*, the bottom $s(x,t)$ for the SWE depends on the flow behavior as illustrated above. The time-dependent flow behavior changes the bottom denoted by $s(x,t)$, also varying in time (4.53).

Mass conservation law

The kinematic boundary condition at the bottom presented in (2.11) without neglect of the temporal derivative of the bottom z_b reads

$$w_b = \frac{\partial z_b}{\partial t} + u_b \frac{\partial z_b}{\partial x} + v_b \frac{\partial z_b}{\partial y} + q,$$

where q from (2.6) is the vertical inflow velocity. In addition to this external inflow q, there is an internal flow q_s over the bottom caused by the motion of $s(x,t)$.

Since $s(x,t)$ is the bottom for the SWE flow, it replaces z_b yielding

$$w_b = \frac{\partial s(x,t)}{\partial t} + u_b \frac{\partial s(x,t)}{\partial x} + q_m + q_s \tag{4.54}$$

in 1D. The term $q_m + q_s$ describes the in- or outflow of water generated by the free-slip condition. q_m is applied to real inflows e.g. from a manhole and represents q from (2.6). In addition to this term, q_s describes the exchange flow between the main flow and the vortex region. Thus, it is the flow velocity over the moving separation line $s(x,t)$ and given by

$$q_s = -\frac{\partial s(x,t)}{\partial t}, \tag{4.55}$$

since an exchange of water between vortex region and main flow is assumed. If the solid bottom z_b varies in time, $q_s = 0$ since there is no water exchange.

The continuity equation reads

$$\frac{\partial H}{\partial t} + \frac{\partial \bar{u}h}{\partial x} = \frac{\partial s(x,t)}{\partial t} + q_m + q_s = q_m = q, \tag{4.56}$$

finally reduced to the known form (2.72) due to (4.55).

A further change due to $\partial s(x,t)/\partial t \neq 0$ within the derivation of the mass conservation law of the 1D-SWE (2.72) is that

$$\frac{\partial H}{\partial t} = \frac{\partial (h + s(x,t))}{\partial t} = \frac{\partial h}{\partial t} + \frac{\partial s(x,t)}{\partial t}.$$

Applying h instead of H yields

$$\frac{\partial h}{\partial t} + \frac{\partial \bar{u}h}{\partial x} = q_m + q_s = q - \frac{\partial s(x,t)}{\partial t}. \tag{4.57}$$

The different effects of the moving bottom (solid or water region) are illustrated in Figure 4.18 for the simplified case of a water column at rest in an open box. The left hand side represents the initial situation at t_0 with water level $H(t_0)$ and the right hand side the changed situation at t_1. A change of

the solid bottom $z_b(t_1)$ increases the water level $H(t_1)$ (top figure). In contrast, the separation of a water region does not change the water level $H(t_1)$ (bottom figure) since the conservation of mass is given by the sum of water in the separated region and the domain above.

Thus, changing $s(x,t)$ in time realized by exchanges of water with the main flow does not affect the mass conservation as long as $s(x) < H(x)$ is assured.

Figure 4.18: Sketch for the effects of a changing bottom over time (left hand side t_0, right hand side t_1) for the simplified case of a water column at rest in an open box. Top: a solid bottom change affects the water level H. Bottom: separating a water region by $s(x)$ does not effect the water level H

Momentum conservation law

Similar considerations for the momentum conservation law yields no change in the horizontal momentum equation due to the time dependency of $s(x,t)$ in contrast to the integration of the mass conservation. In the integration of the horizontal momentum equation, $u_b\,\partial z_b/\partial t$ occurs twice: as a positive term from the transport theorem

$$\int_{z_b}^{H} \frac{\partial}{\partial t}u\,dz = \frac{\partial}{\partial t}\int_{z_b}^{H} u\,dz - u_H\frac{\partial H}{\partial t} + u_b\frac{\partial z_b}{\partial t} \qquad (4.58)$$

and as a negative term when inserting the kinematic boundary conditions into

the lower boundary value of the depth integration of $\partial uw/\partial z$

$$\int_{z_b}^{H} \frac{\partial uw}{\partial z}\, dz = uw|_{z_b}^{H} = u_H w_H - u_b w_b = u_H\left(\frac{\partial H}{\partial t} + u_H \frac{\partial H}{\partial x}\right) - u_b\left(\frac{\partial z_b}{\partial t} + u_b \frac{\partial z_b}{\partial x}\right).$$

(4.59)

Due to the different signs, the additional terms $\partial z_b/\partial t$ cancel. Thus, the change of the solid bottom level does not affect the horizontal momentum as illustrated in the top sketches from Figure 4.19.
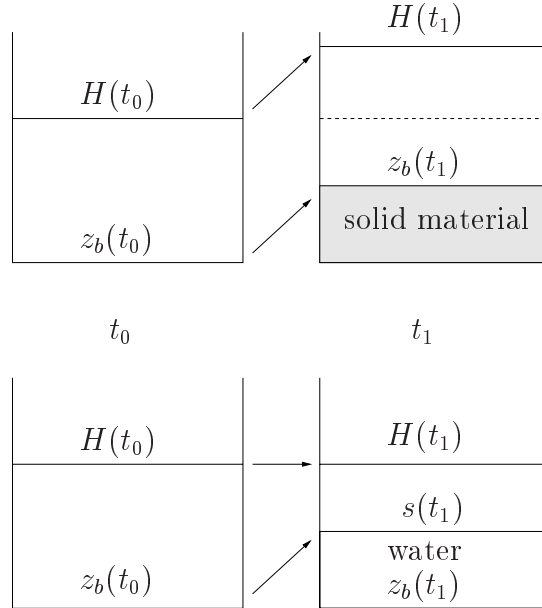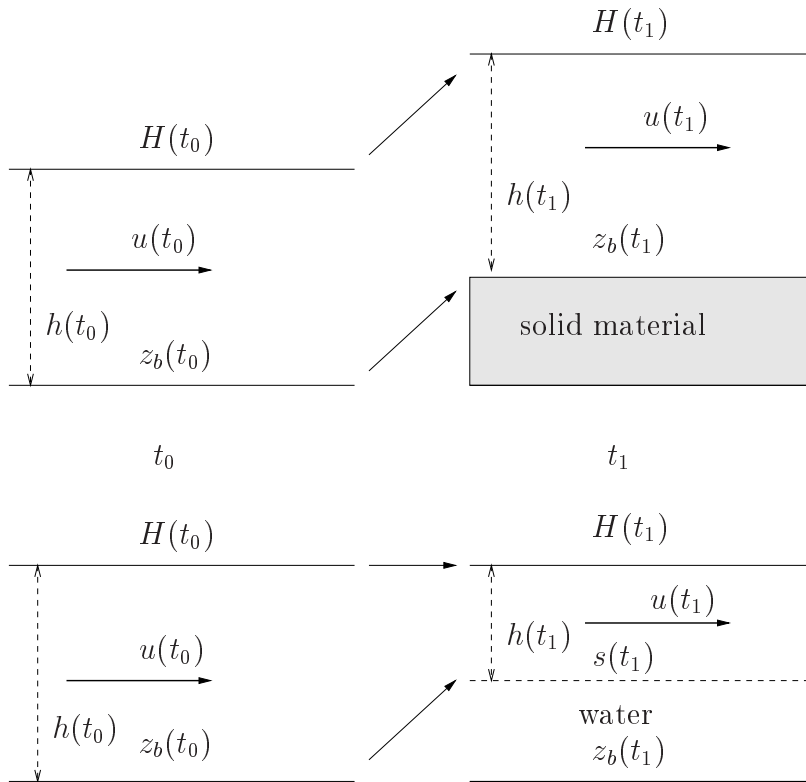

Figure 4.19: Sketch for the effects of a changing bottom over time (left hand side t_0, right hand side t_1) for the simplified case of a homogeneous water flow with initial horizontal velocity $u(t_0)$. Top: a solid bottom change does not affect the horizontal momentum $u(t_0)h(t_0) = u(t_1)h(t_1)$. Bottom: separating a water region by $s(x,t)$ does affect the horizontal momentum $u(t_0)h(t_0) \neq u(t_1)h(t_1)$.

Remark 4.12 *This does not mean that a change of the solid bottom can not influence the horizontal momentum at all. A lift of the solid bottom in a small interval entails a lift of the water level H due to changes in the mass*

conservation as described above. Even if this lift has no direct effect on the momentum equation, the changed water level entails a horizontal moment as well.

The bottom sketches in Figure 4.19 show the effects of the temporal change of the vortex separation line on the momentum uh. Since the change of $s(x,t)$ is not assumed to change the horizontal velocity u, we assume

$$u(t_0) = u(t_1) \tag{4.60}$$

Since the vortex contains a circulating motion, this assumption is reasonable. The moving water column is thus simply cut or added with the continuous velocity u. The assumption (4.60) yields the source term

$$-u\frac{\partial s(x,t)}{\partial t} \tag{4.61}$$

in the horizontal momentum equation, describing exactly the mentioned process of cutting and adding the moving water column. This yields the 1D-SWE for a moving bottom as a separated vortex layer $s(x,t) = f(w_b(t), u_0(t))$.

$$\frac{\partial}{\partial t}\begin{pmatrix} H \\ uh \end{pmatrix} + \frac{\partial}{\partial x}\begin{pmatrix} uh \\ u^2h + \frac{1}{2}gh^2 \end{pmatrix} = \begin{pmatrix} q \\ gh(-\frac{\partial s(x,t)}{\partial x} - S_{fx}) - u\frac{\partial s(x,t)}{\partial t} \end{pmatrix}. \tag{4.62}$$

4.3.3   Effects of Traveling Vortices

The assumption of a completely stationary separated vortex region is not valid. In particular for the flow problem *curb*, the NSE calculations are not stationary. Changes of the vortex region are caused by vortex motions yielding fluctuations in $s(x,t)$. The NSE solution includes separation of vortices that travel with the main flow. The size of these vortices is reduced until they are finally dissolved due to viscous friction as illustrated in Figure 4.20.

The time-dependent design of $s(x,t)$ can be adapted on the vortex motion in order to include these effects. Since a given vortex motion influences the design of $s(x,t)$, the computation of the SWE flow has to be coupled with a vortex flow model.

This inclusion requires very high computational effort. Furthermore, we are not interested in the resolution of every single vortex but in the reliable description of the average flow behavior. Thus, we neglect the motion of the separated vortices and rebuild only the large vortex areas in the flow domain.
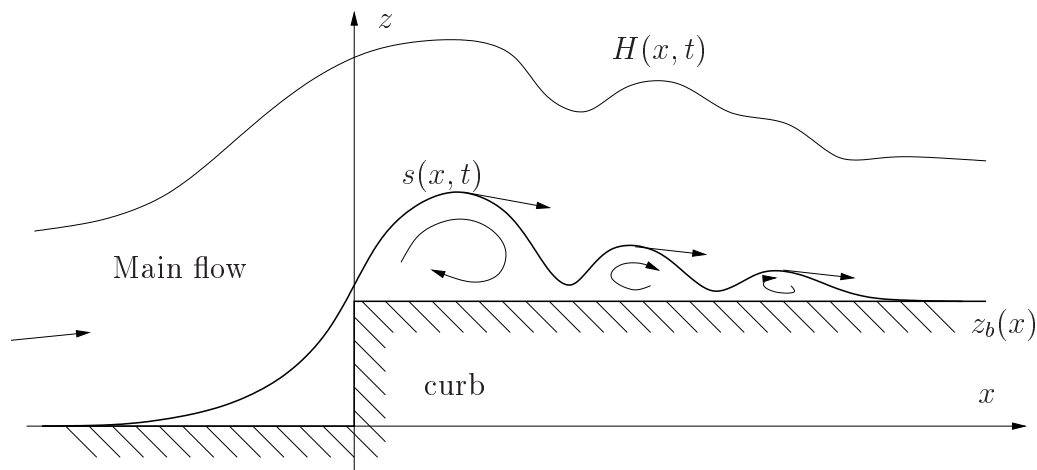
Figure 4.20: Separated vortices influencing the design of the interface $s(x,t)$

4.4 Friction Approach for Extended SWE
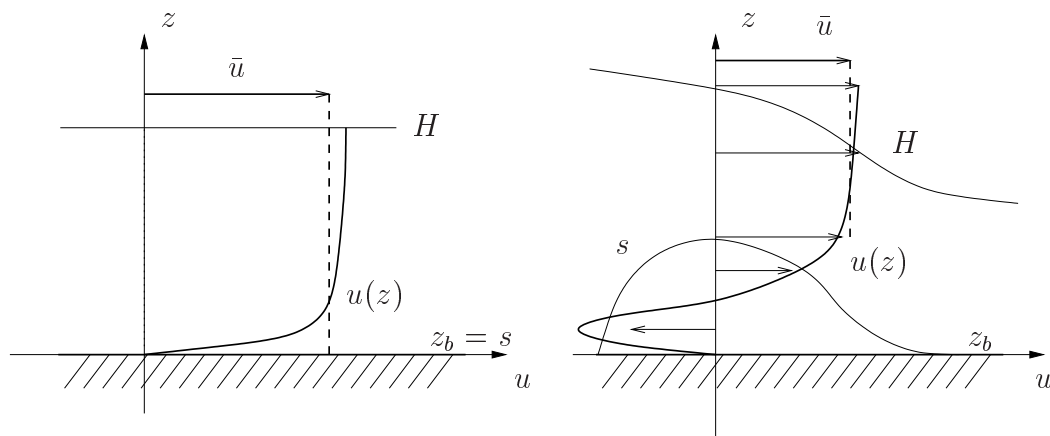
Figure 4.21: Sketch for extensions of friction approach for the flow over a separated vortex region. Comparison of $u(z)$ for fixed bottom z_b and vortex region $s(x)$

The Extension *Vortex Separation* affects the friction approach of the SWE of Section 2.4.3 as illustrated in Figure 4.21. In contrast to the classical SWE (left hand side), the main flow is not flowing over a solid bottom with bottom friction due to a viscous bottom layer but over a vortex region of water (right hand side). Since the vortex region contains a circulating flow, $\frac{\partial u(z)}{\partial z}$ at the separation line $s(x,t)$ is not as dominant as in the classical SWE case. Hence, the assumption for the dominant bottom friction term S_{bx} is not fulfilled and

the considerations have to be extended.

Friction forces are not the dominant forces in the free surface flow of water considered for floods in urban areas. This is in particular evident in Figure 3.7, where the analytical in-viscid Euler solution is in agreement with the numerical NSE solution.

Thus, the high effort to consider every part x of the vortex region separately and to derive a friction formulation depending on $s(x, t)$ will cause only small effects. Instead, we propose to consider the vortex region within only one friction approach, that contains the integrated considerations.

The vortex motion has to be kept against the viscous and bottom friction. The size of the horizontal velocity of the vortex motion illustrated in Figure 4.21 above the viscous bottom layer is almost equal to the horizontal flow velocity u. Assuming the dominance of this bottom friction effects for the whole friction approach, it is reasonable to apply a similar friction approach on the separated vortex region as on the solid bottom. Since we seek for extensions of the classical SWE as close as possible to the classical ones, we apply the same friction approach. Within modifications of the friction parameter n, differences could be captured if required.

The agreement of the analytical in-viscid solutions and the numerical viscid NSE results, e.g. Figure 3.7 demonstrates the low importance of the friction approaches for the considered flow problems.

Chapter 5

Extension *Pressure Correction*

The zeroth order equations of the asymptotic expansion of the Euler Equations of Section 2.4.1 yield a zero vertical velocity $w^{(0)} = 0$ and horizontal flow velocities $u^{(0)}$ and $v^{(0)}$ that are constant over the water depth $h^{(0)}$. The first order equations of this expansion yield the hydrostatic pressure distribution $p^{(0)} = p_{hy}$ and the frictionless 2D-SWE formulated in zeroth order terms $h^{(0)}$, $u^{(0)}$ and $v^{(0)}$. The 2D-SWE are also derived -independently of the asymptotic expansion- in Section 2.4.2 from the 3D-Euler Equations by assuming hydrostatic pressure by depth-integration.

Both formulations (2.53)-(2.55) and (2.70) of the frictionless 2D-SWE can be transferred into each others if the zeroth order expansion terms of the velocity are identified with the depth-averaged velocity as already discussed in Section 2.4. The hydrostatic pressure distribution is also common in both formulations.

We first demonstrate the relations between vertical velocity and pressure distribution and derive the Extension *Pressure Correction* by approximating vertical velocities and elaborating their contribution to the pressure distribution into the SWE.

5.1   Hydrostatic Pressure vs Vertical Velocity

Theorem 5.1 demonstrates the equivalence of the hydrostatic pressure distribution and the neglect of the material derivative of the vertical velocity $\dot{w}$ for the in-viscid case.

Theorem 5.1 *The assumption of a hydrostatic pressure distribution (2.48) is equivalent to the assumption of vanishing material derivative of the vertical velocity $\dot{w} = 0$ for in-viscid, incompressible fluids.*

Proof. Inserting the hydrostatic pressure distribution p_{hy} from (2.48) into the vertical momentum equation of the Euler Equations (2.4) yields $\dot{w} = 0$.

Inserting the assumption $\dot{w} = 0$ in the z-momentum equation of the Euler Equations yields:

$$0 = \dot{w} = -\frac{1}{\rho}\frac{\partial}{\partial z}p - g \qquad (5.1)$$

Since g is a constant, (5.1) can be integrated yielding

$$p(z) \;=\; p_H + \int_H^z -\rho g \; dz \qquad (5.2)$$

$$p_{hy}(z) \;=\; p_H + \rho g(H - z), \qquad (5.3)$$

with the constant pressure $p(H) = p_H$ at the free surface as assumed in Section 2.3.1 and thus identical to (2.48). ∎

Vertical velocity of NSE benchmark solution

Figure 5.1 illustrates the size of the vertical velocities of the NSE benchmark solution for the flow problem *manhole* with the vertical inflow velocity $w_b = 2m/s$ in the colored plot of the flow domain.
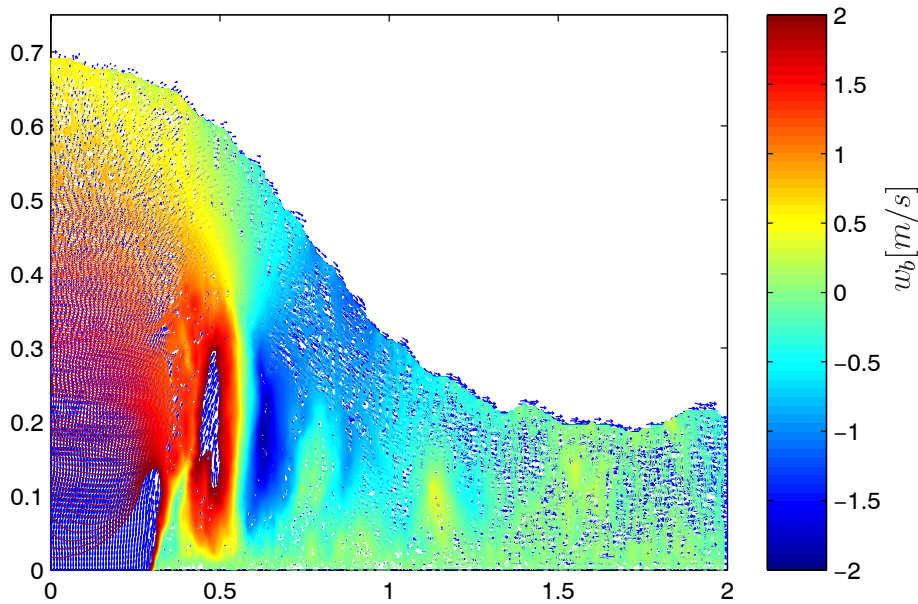

Figure 5.1: Size of vertical velocity from the NSE-benchmark solution for the flow problem *manhole* with $w_b = 2m/s$

High positive values with upward flow direction are colored in red at and above the manhole. Negative values with flow direction downward are colored in blue and occur above the decreasing part of the vortex region. Far away from the manhole the values of w are almost 0.

Remark 5.2 *Since the vortex region is separated from the main flow by the Extension* Vortex Separation *of Chapter 4, its extreme vertical velocity values in Figure 5.1 are not discussed.*

The sizes of the vertical velocity w are comparable to those of the horizontal velocity u. High variations of w cause high values of $\dot{w}$ in the vicinity of the manhole. Such not vanishing values of $\dot{w} \neq 0$ are in particular evident for the flow over the separated vortex region. The physical design approach of Section 4.2 includes serious changes ($\dot{w} = -g$) of the vertical velocity w for water particles traveling on the separating trajectory. This fact is in contradiction to the assumption $\dot{w} = 0$ and following Theorem 5.1 also in contradiction to the hydrostatic pressure assumption.

Since the hydrostatic pressure assumption is the base for the derivation of the classical SWE, the Extension *Pressure Correction* modifies the pressure distribution by incorporating vertical velocities.

We first approximate vertical velocities via linear interpolation between the vertical velocities at the free surface and the bottom involved in the kinematic boundary condition. Secondly we demonstrate that this approximation is identical to the first order expansion term $w^{(1)}$ of the vertical velocity from the asymptotic expansion.

5.2   Approximation of Vertical Velocity w

5.2.1 w_H and w_b from Kinematic Boundary Conditions

Vertical velocities at the free surface and the bottom occur in the kinematic boundary conditions involved in both derivations of the classical SWE in Section 2.4.2. We repeat (2.11) for the 2D-Euler Equations (neglect of y-direction) also illustrated in Figure 5.2 for the stationary flow case:

$$w_H = \frac{\partial H}{\partial t} + u_H \frac{\partial H}{\partial x}, \tag{5.4}$$

$$w_b = \frac{\partial z_b}{\partial t} + u_b \frac{\partial z_b}{\partial x}. \tag{5.5}$$

The bottom elevation z_b for the flow problems is given not only by the fixed topography but also by the Extension *Vortex Separation* that may depend on time. Thus (5.5) is extended by $\partial z_b / \partial t$.

Assumptions for u_H and u_b
The horizontal flow velocity u_H and u_b are required to compute w_H and w_b from (5.4) and (5.5). The SWE derived by depth-integration consider $u = \bar{u}$
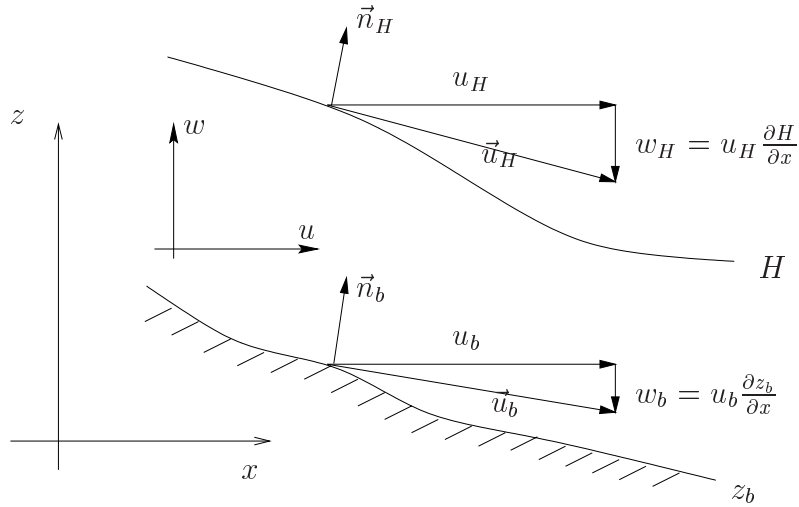
Figure 5.2: Kinematic boundary conditions for stationary 2D-Euler flow

as a depth-averaged velocity $\bar{u} = \frac{1}{h} \int_{z_b}^{H} u \, dz$ without further information about its vertical distribution.

No-slip conditions are assumed as dynamic boundary conditions at the bottom as already remarked in the Sections 2.3.5 and 2.4.3 for the viscous NSE flow. Due to the small viscosity of water ($\nu \approx 10^{-6} \frac{m^2}{s}$) the viscous bottom layer denoted with δz is small. This results from considerations of typical sizes of bottom layers for low-viscid flow but also from the NSE benchmark calculations and their agreement to the in-viscid analytical solution from Chapter 3.
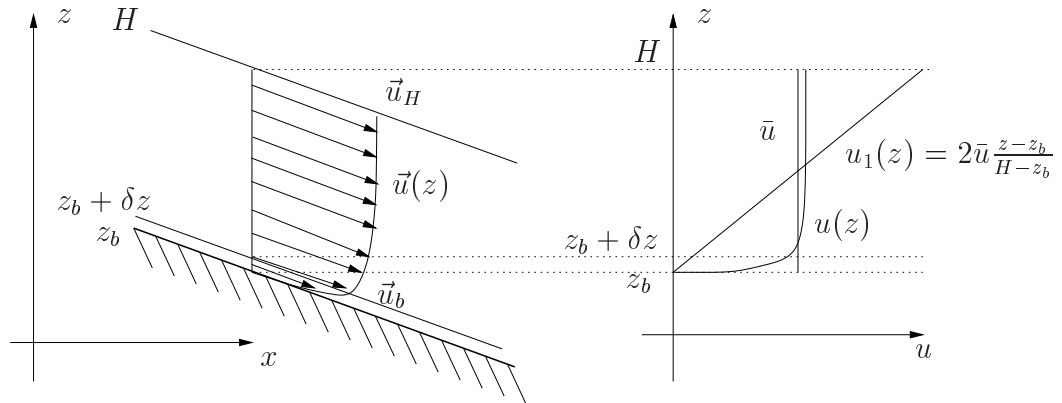
Figure 5.3: Sketch of the vertical distribution of the velocity $\vec{u}(z)$ in a cross section with a small bottom layer of size δz (left hand side) and distribution of the horizontal velocity component $u(z)$ with the depth-average $\bar{u}$ in comparison to a linear distribution $u_1(z)$ with $u|_{z=z_b} = 0$ and $u|_{z=H} = 2\bar{u}$ (right hand side)

Figure 5.3 illustrates a typical vertical distribution of the velocity vector $\vec{u}(z)$ at the left with a small bottom layer and an almost homogeneous distribution above that small bottom layer. This holds in particular for the horizontal velocity component $u(z)$ of the NSE flow at the right. The horizontal velocity u above the small viscous bottom layer at $z = z_b + \delta z$ is almost equal to the average over the cross section $u|_{z=z_b+\delta z} \approx \bar{u}$. Thus, we set

$$u_H = u_b = \bar{u} = u. \tag{5.6}$$

**Remark 5.3** *The assumption $u_H = u_b = \bar{u} = u$ has even more eligibility for the flow over the vortex region. The bottom is not a fixed ground but a water layer with vortex motion inside. The physical design of the vortex region is obtained by setting $u = u_{SWE}$ for the water particles traveling on that path.*

Furthermore it is reasonable to apply $w_b = w(z_b + \delta z)$ as vertical velocity close to the bottom. Assuming a constant size of the viscous bottom layer δz yields

$$w_b = w(z_b + \delta z) = u(z_b + \delta z)\frac{\partial(z_b + \delta z)}{\partial x} = \bar{u}\frac{\partial z_b}{\partial x}. \tag{5.7}$$

Remark 5.4 *The linear distribution $u_1(z) = 2\bar{u}\frac{z-z_b}{H-z_b}$ resulting as the linear profile, that assumes $u_b = 0$ and $\bar{u} = \int_{z_b}^{H} u_1(z)\,dz$ is illustrated in Figure 5.3. The differences to $u(z)$ in particular at the surface and above the bottom layer are obvious. Thus, it is more reasonable to approximate $u(z) \approx \bar{u}$.*

Inserting the depth-averaged horizontal velocity u in (5.4) and (5.5), the vertical velocity at the surface w_H and at the bottom w_b can be computed for the SWE solution:

$$w_H = \frac{\partial H}{\partial t} + u\,\frac{\partial H}{\partial x} \tag{5.8}$$

$$w_b = \frac{\partial z_b}{\partial t} + u\,\frac{\partial z_b}{\partial x} \tag{5.9}$$

The flow problem *manhole* involves inflow terms $q(x)$ in the continuity equation (2.62) given as the vertical inflow velocity normal to the plane ground. The estimation of the vertical velocity at the bottom w_b is replaced by

$$w_b(x) = q(x) \tag{5.10}$$

in the interval of the manhole.

5.2.2   Approximation of Vertical Distribution $w(z)$

Departing from the vertical velocity w_H (5.8) at the surface and w_b (5.9) at the bottom, the vertical distribution $w(z)$ is approximated. Since the SWE approach considers even the dominant horizontal velocity u as an average over the depth $\bar{u}$, it seems to be reasonable to assume likewise a depth-averaged vertical velocity $\bar{w} = w_0$ in a zeroth order approximation

$$w(x,z) = \bar{w}(x) = w_0(x) = \frac{w_H(x) + w_b(x)}{2}. \qquad (5.11)$$

$w_0(x)$ is chosen as the average of the vertical velocities at the surface w_H and the bottom w_b.
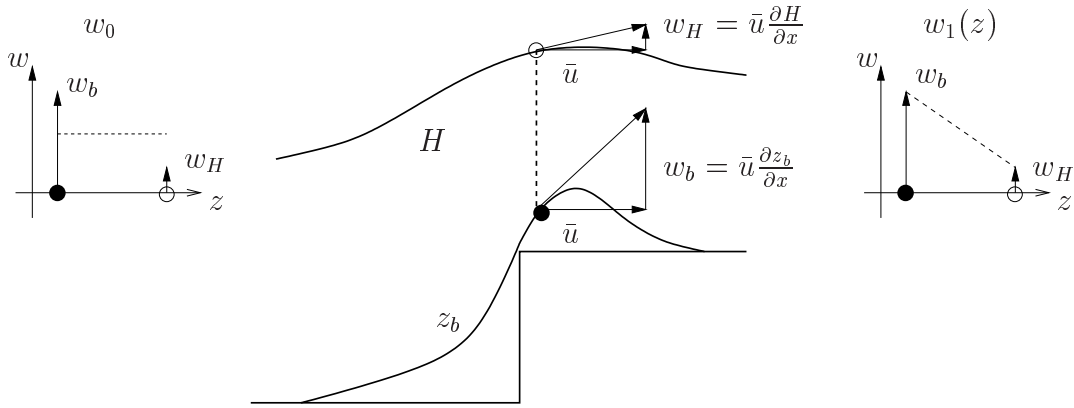
Figure 5.4: Zeroth order approximation $w_0(z)$ and first order approximation $w_1(z)$ of vertical distribution $w(z)$

Figure 5.4 illustrates this zeroth order approximation w_0 on the left hand side. On the right hand side, a first order approximation of the vertical distribution $w(z)$ is assumed by a linear interpolation between w_H and w_b

$$w(x,z) = w_1(x,z) = \frac{z - z_b}{h} w_H(x) + (1 - \frac{z - z_b}{h}) w_b(x). \qquad (5.12)$$

Within this first order approximation, the vertical velocity gradient

$$\frac{\partial w_1}{\partial z} = \frac{w_H - w_b}{h} \qquad (5.13)$$

is generally not zero. Rewriting w_1 in terms of w_0 and $\partial w_1/\partial z$ yields

$$w_1(x,z) = w_0(x) + \frac{\partial w_1}{\partial z}(x)(z - (z_b + \frac{h}{2})). \qquad (5.14)$$

Since w_0 is constant over the water depth we denote it as zeroth order approximation of $w(z)$. According to that we call the linear interpolation first

order approximation w_1. The order describes the degree of vertical resolution of the vertical velocity $w(z)$.

We restrict this presentation to the zeroth order $w_0(x)$ and first order approximation $w_1(x, z)$. Higher order approximations of the vertical velocities w, e.g. quadratic, are not considered in this thesis, since their derivation would require additional assumptions. Furthermore, it seems to be sufficient to apply w_0 and w_1 recalling that even the horizontal flow velocity is approximated as zeroth order approximation over the water depth.

Both approximations $w_0(x)$ and $w_1(x, z)$ are based only on the vertical velocities at the surface w_H and the bottom w_b. Thus, we estimate them explicitly from the solution of the SWE

$$
\begin{aligned}
w_0(x) &= \frac{w_H(x) + w_b(x)}{2} \\
&= \frac{1}{2}\left[\frac{\partial H(x)}{\partial t} + \frac{\partial z_b(x)}{\partial t} + u(x)\left(\frac{\partial H(x)}{\partial x} + \frac{\partial z_b(x)}{\partial x}\right)\right], \quad (5.15) \\
w_1(x, z) &= w_0(x) + \frac{w_H(x) - w_b(x)}{h(x)}\left(z - \left(z_b(x) + \frac{h(x)}{2}\right)\right) \\
&= \frac{1}{2}\left[\frac{\partial H(x)}{\partial t} + \frac{\partial z_b(x)}{\partial t} + u(x)\left(\frac{\partial H(x)}{\partial x} + \frac{\partial z_b(x)}{\partial x}\right)\right] \\
&\quad + \left[\frac{\partial H(x)}{\partial t} - \frac{\partial z_b(x)}{\partial t} + u(x)\left(\frac{\partial H(x)}{\partial x} - \frac{\partial z_b(x)}{\partial x}\right)\right] \\
&\quad \cdot \frac{z - \left(z_b(x) + \frac{h(x)}{2}\right)}{h(x)}. \quad (5.16)
\end{aligned}
$$

If $x \in [0, x_m]$ belongs to the interval of the manhole with prescribed vertical inflow velocity $w_b(x) = q$, we obtain:

$$
\begin{aligned}
w_0(x) &= \frac{1}{2}\left[\frac{\partial H(x)}{\partial t} + u(x)\frac{\partial H(x)}{\partial x} + q(x)\right] \quad (5.17) \\
w_1(x, z) &= \frac{1}{2}\left[\frac{\partial H(x)}{\partial t} + u(x)\frac{\partial H(x)}{\partial x} + q(x)\right] \\
&\quad + \left[\frac{\partial H(x)}{\partial t} + u(x)\frac{\partial H(x)}{\partial x} - q(x)\right] \\
&\quad \cdot \frac{z - \left(z_b + \frac{h}{2}\right)}{h(x)}. \quad (5.18)
\end{aligned}
$$

Remark 5.5 *In 2D, $v(x)$ and the y-derivatives of $H(x, y)$ and $z_b(x, y)$ are involved additionally as presented in Chapter 6.*

Remark 5.6 *We usually avoid a notation at great length and do not write the time dependency of the variables $u(x, t)$, $H(x, t)$, $z_b(x, t)$ and $w(x, t)$ explicitly. That does not mean we consider stationary solutions only.*

5.2.3   Comparison of Approximation and Asymptotic Expansion

We recall (2.40) and (2.52) from Section 2.4.1 for the 2D-Euler case

$$w^{(0)} \;=\; 0, \tag{5.19}$$

$$w^{(1)}(z) \;=\; -\frac{\partial u^{(0)}}{\partial x}\, z + \frac{\partial(u^{(0)} z_b)}{\partial x}, \tag{5.20}$$

and show that w_1 constructed in (5.16) is identical to $w^{(1)}$ from (5.20) if we assume $u^{(0)} = \bar{u} = 1/h \int_{z_b}^{H} u\, dz$.

Lemma 5.7 w_0 *is the depth-average of* $w_1(z)$, *i.e.* $w_0 = \bar{w}_0 = \bar{w}_1$

Proof. $\bar{w}_1 \;=\; \frac{1}{h}\int_{z_b}^{H} w_1\, dz \;=\; \frac{1}{h}\int_{z_b}^{H} w_0\, dz + \frac{1}{h}\int_{z_b}^{H} \frac{\partial w}{\partial z}(x)(z - (z_b + \frac{h}{2}))\, dz \;=\; \bar{w}_0 + \frac{\partial w}{\partial z}0 = \bar{w}_0 = w_0$ ∎

Theorem 5.8 *The linear approximation* w_1 *from (5.16) is identical to the first order expansion term of the asymptotic expansion* $w^{(1)}$ *from (5.20)*

$$w_1(x, z) = w^{(1)}(x, z). \tag{5.21}$$

$w_0(x)$ *from (5.15) is the depth-average of* $w^{(1)}(x, z)$

$$w_0(x) = \frac{1}{h(x)} \int_{z_b}^{H} w^{(1)}(x, z) = \frac{1}{h(x)} \int_{z_b}^{H} w_1(x, z). \tag{5.22}$$

Proof. The first order equation of the asymptotic expansion of the continuity equation of the 2D-Euler Equation reads

$$\frac{\partial w^{(1)}}{\partial z} = -\frac{\partial u^{(0)}}{\partial x}. \tag{5.23}$$

The first order boundary conditions for $w^{(1)}$ are identical to the kinematic boundary conditions from (5.4) and (5.5):

$$w^{(1)}|_{z=H} \;=\; \frac{\partial H^{(0)}}{\partial t} + u^{(0)}\frac{\partial H^{(0)}}{\partial x} \tag{5.24}$$

$$w^{(1)}|_{z=z_b} \;=\; \frac{\partial z_b}{\partial t} + u^{(0)}\frac{\partial z_b}{\partial x}. \tag{5.25}$$

(5.23) together with the given value of $w^{(1)}(z_b)$ at the bottom in (5.25) yields identical to (5.20)

$$w^{(1)}(z) = \frac{\partial w^{(1)}}{\partial z}(z - z_b) + w^{(1)}(z_b) = -\frac{\partial u^{(0)}}{\partial x}(z - z_b) + u^{(0)}\frac{\partial z_b}{\partial x}. \tag{5.26}$$

We demonstrate that (5.23) is fulfilled by $\partial w_1/\partial z$ from (5.13):

$$\frac{\partial w_1}{\partial z} = \frac{w_H - w_b}{h} = \frac{w^{(1)}|_{z=H} - w^{(1)}|_{z=z_b}}{h^{(0)}} \tag{5.27}$$

due to the identity of the boundary conditions, yielding

$$\frac{\partial w_1}{\partial z} = \frac{\frac{\partial H^{(0)}}{\partial t} + u^{(0)}\frac{\partial H^{(0)}}{\partial x} - u^{(0)}\frac{\partial z_b}{\partial x}}{h^{(0)}}. \tag{5.28}$$

Applying the mass conservation law

$$\frac{\partial H^{(0)}}{\partial t} + \frac{\partial u^{(0)} h^{(0)}}{\partial x} = 0 \tag{5.29}$$

yields

$$\begin{aligned}
\frac{\partial w_1}{\partial z} &= \frac{-\frac{\partial u^{(0)} h^{(0)}}{\partial x} + u^{(0)}\frac{\partial h^{(0)} + z_b}{\partial x} - u^{(0)}\frac{\partial z_b}{\partial x}}{h^{(0)}} \\
&= -\frac{\partial u^{(0)}}{\partial x} = \frac{\partial w^{(1)}}{\partial z}.
\end{aligned} \tag{5.30}$$

¿From (5.30) together with the identity of the boundary conditions, we conclude that w_1 in (5.16) is identical to the first order expansion term $w^{(1)}$

$$w_1(x, z) = w^{(1)}(x, z). \tag{5.31}$$

w_0 in (5.15) represents the depth-average of w_1 due to Lemma 5.7 and thus also the depth-average of $w^{(1)}$

$$w_0 = \frac{1}{h^{(0)}} \int_{z_b}^{H^{(0)}} w^{(1)}(z) \, dz. \tag{5.32}$$

∎

The difference between the approximation of $w(z)$ from above and the asymptotic expansion is that the zeroth order approximation $w_0 \neq 0$ instead of $w^{(0)} = 0$. The fact that $w^{(0)} = 0$ in the asymptotic expansion yields simplifications in the resulting equations of motion, in particular in the pressure distribution $p(z)$.

5.2.4 Vertical Velocity w_0 for the Flow Problems

Figures 5.5 and 5.6 illustrate the stationary SWE solution with the Extension *Vortex Separation* for the flow problems *manhole* (up for different values of q) and *curb* (left). The vertical velocities $w_0(x)$ are computed for these stationary SWE solutions and compared to the depth-averaged vertical velocities of the according NSE benchmark solutions. The averaging of w was not performed over the whole water depth but the vortex regions of the NSE solutions are excluded.

Flow Problem *Manhole*

We consider the stationary solution for the flow problem *manhole* in Figure 5.5 for different vertical inflow velocities $w_b = 1m/s$ (left), $w_b = 2m/s$ (middle) and $w_b = 3m/s$ (right). The comparisons of w_0 to the depth-averaged vertical velocities $\bar{w}$ from the NSE benchmark solution are amazingly good.

Figure 5.5: Up: bottom (green line) and free surface elevation (red line) from SWE with Extension *Vortex Separation*. Down: Comparison of vertical velocity w_0 (green smooth line) with the depth-averaged vertical velocity from the NSE benchmark solution (blue fidget line) for the flow problem *manhole* for the vertical inflow velocities $w_b = 1m/s$ (left) $w_b = 2m/s$ (middle) and $w_b = 3m/s$ (right)

Explanation 5.9 *The plotted values for w_0 are computed from the SWE-solution with (5.11). The depth-averaged NSE results are plotted for compar-*

ison only. Taking the simplifications in the derivation of (5.11) into account, the qualitative and quantitative agreements are amazingly good.

Obviously, we obtain $w_0(x = 0) = 1/2 \, w_b$ at the left boundary. That is because the water level above the manhole is almost constant and the horizontal velocity u is small yielding $w_H = u \, \partial H / \partial x \approx 0$. w_0 decreases since $w_H < 0$ due to the decreasing $\partial H / \partial x < 0$ and the increasing $u > 0$. At the top of the vortex region we have $w_b = 0$ and due to $w_H < 0$ we obtain $w_0 < 0$ for that point already. w_0 reaches a minimum and then approaches the value 0 far away from the manhole.

Flow Problem *Curb*

Similar to the flow problem *manhole*, the comparison result of w_0 to the depth-averaged vertical velocities from the NSE benchmark solution in the Figure 5.6 reproduces the principal flow behavior. Due to separating vortices in the NSE solution, that were partly cut out of the averaging process according to the design of the vortex region, oscillations in the depth avaraged NSE results occur.
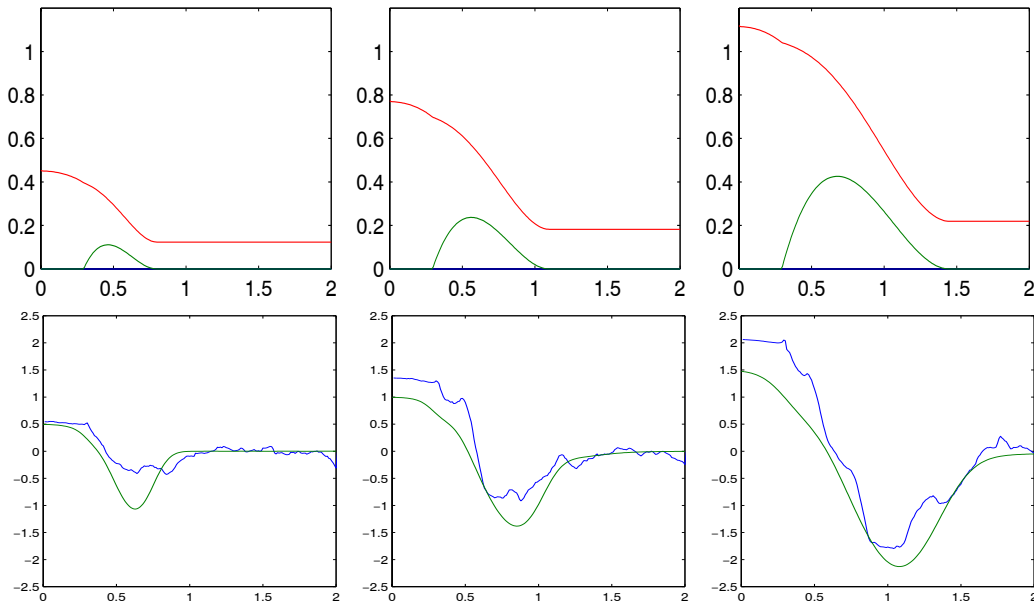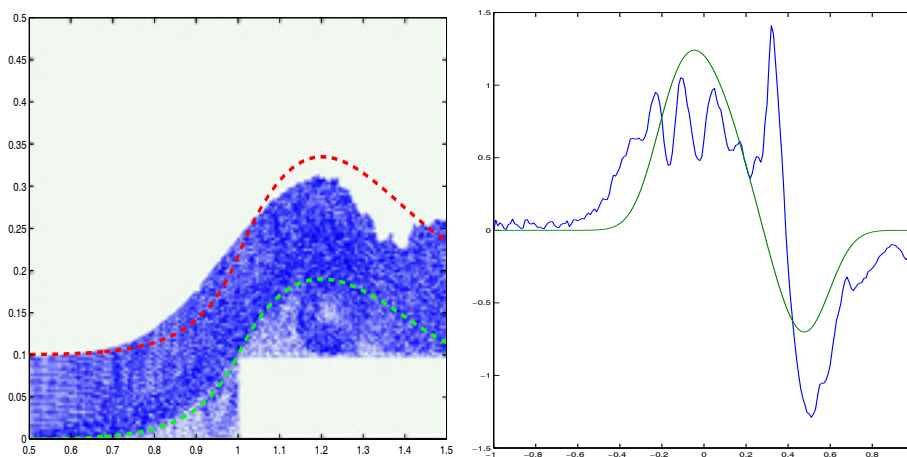

Figure 5.6: Left: bottom and free surface elevation from SWE with Extension *Vortex Separation*. Right: Comparison of vertical velocity w_0 (green smooth line) with the depth-averaged vertical velocity from the NSE benchmark solution (blue fidget line) for the flow problem *curb* for the inflow velocity $u_0 = 3m/s$

Some dm in front of the curb, the vertical velocity $w_0 = 0$. This holds also some dm behind the curb. In between we observe an increase of vertical velocity to a maximum at the curb and then a decrease with a negative minimum value located in the decreasing part of the vortex region before w_0 approaches 0.

5.3 Pressure Correction p_c

Both derivations of the SWE from the Sections 2.4.1 and 2.4.2 are based on a hydrostatic pressure distribution p_{hy} (2.48). Following Theorem 5.1, this assumption is equivalent to the assumption of vanishing material derivatives of the vertical velocity $\dot{w} = 0$ in the in-viscid case. The approximation of the vertical velocities w_0 and w_1 from the previous section allows also the evaluation of $\dot{w}$, assuming that w is smooth enough. Thus, we correct the pressure distribution $p(z)$ by adding a pressure correction term p_c involving $\dot{w}$.

The z-momentum equation (5.1) of the 2D-Euler Equations (2.4) of Section 2.3.4 reads

$$\dot{w} = \frac{dw}{dt} = \frac{\partial}{\partial t}w + \left(u\frac{\partial}{\partial x} + w\frac{\partial}{\partial z}\right)w = -\frac{1}{\rho}\frac{\partial}{\partial z}p - g. \qquad (5.33)$$

$\dot{w}$ can be evaluated due to the approximation of w from the previous section. This yields an ODE for the pressure with known right hand side

$$\frac{\partial p}{\partial z} = -\rho g - \rho\left(\frac{\partial w}{\partial t} + u\frac{\partial w}{\partial x} + w\frac{\partial w}{\partial z}\right) = -\rho(g + \dot{w}). \qquad (5.34)$$

We integrate (5.34) from the free surface H to z and obtain

$$p(z) = p_H + \rho g(H - z) + \rho\dot{w}(H - z). \qquad (5.35)$$

$p_c(z) = \rho\dot{w}(H - z)$ is an additional term correcting the hydrostatic pressure distribution p_{hy} and is thus denoted as pressure correction $p_{correction} = p_c$ in the pressure distribution

$$p(z) = p_{hydrostatic} + p_{correction} = p_{hy} + p_c. \qquad (5.36)$$

Since the dimension of $\dot{w}$ is m/s^2, the dimension of an acceleration,

$$\dot{w} = \frac{\partial w}{\partial t} + u\frac{\partial w}{\partial x} + w\frac{\partial w}{\partial z} = g_c = \tilde{g} \qquad (5.37)$$

can be interpreted as a correction of the gravity acceleration $\tilde{g}$ due to changes of w. The pressure distribution reads:

$$p(z) = p_H + \rho(g + \tilde{g})(H - z). \qquad (5.38)$$

The acceleration correction $\tilde{g}$ is not constant, but depends at least on x and generally also on z.

5.3.1 Pressure Correction for Zeroth Order Approximation w_0

For the zeroth order approximation $w = w_0(x)$, the vertical derivative of w_0 is zero $\partial w_0/\partial z = 0$ since w_0 is constant over the water depth.

$$\tilde{g} = \dot{w} = \frac{\partial w}{\partial t} + u\frac{\partial w}{\partial x} \tag{5.39}$$

is thus simplified and (5.35) reads

$$p(z) = p_{hy}(z) + p_c(z) = p_H + \rho g(H - z) + \rho(\frac{\partial w}{\partial t} + u\frac{\partial w}{\partial x})(H - z). \tag{5.40}$$

Only in this zeroth order approximation, $\tilde{g}(x)$ does not depend on z. The pressure correction term for the zeroth order approximation of w_0 is

$$p_c(z) = \rho\tilde{g}(H - z) = \rho(\frac{\partial w}{\partial t} + u\frac{\partial w}{\partial x})(H - z). \tag{5.41}$$

5.3.2 Pressure Correction for First Order Approximation w_1

For the first order approximation $w_1(x, z)$, we obtain a quadratic pressure distribution. We recall (5.14)

$$w_1(x, z) = w_0(x) + \frac{\partial w_1}{\partial z}(x)(z - (z_b + \frac{h}{2}))$$

and integrate (5.39) from the free surface H to z

$$\int_H^z \frac{\partial p}{\partial z} \, dz = \int_H^z -\rho g - \rho(\frac{\partial w}{\partial t} + u\frac{\partial w}{\partial x} + w\frac{\partial w}{\partial z}) \, dz \tag{5.42}$$

to obtain

$$p(z) = p_H + \rho(g + \tilde{g}^1)(H - z) + \rho\frac{1}{2}((\frac{\partial w_1}{\partial z})^2 + u\frac{\partial^2 w_1}{\partial z\partial x})(H^2 - z^2) \tag{5.43}$$

with

$$\tilde{g}^1 = \frac{\partial w_1}{\partial t} + u\frac{\partial w_0}{\partial x} - u\frac{\partial}{\partial x}(\frac{\partial w_1}{\partial z}(z_b + \frac{h}{2})) + w_0\frac{\partial w_1}{\partial z} - (\frac{\partial w_1}{\partial z})^2(z_b + \frac{h}{2}). \tag{5.44}$$

The pressure correction term of the first order approximation w_1 reads

$$p_c^1(z) = \rho\tilde{g}^1(H - z) + \rho\frac{1}{2}((\frac{\partial w_1}{\partial z})^2 + u\frac{\partial^2 w_1}{\partial z\partial x}). \tag{5.45}$$

5.4   Impact of Pressure Correction p_c on SWE: S_{p_c}

We recall the derivation of the SWE by depth-integration of the Euler Equations where we assumed a hydrostatic pressure distribution (2.48). Integrating the equations over the water depth yields the SWE with depth-averaged horizontal velocities. The forces due to pressure gradients are involved in the momentum equation of the 1D-SWE (2.72) as depth-integrated hydrostatic pressure gradient term

$$\int\limits_{z_b}^{H} -\frac{1}{\rho}\frac{\partial p}{\partial x}\ dz = -gh\frac{\partial H}{\partial x} = -gh\frac{\partial h + z_b}{\partial x} = \frac{\partial}{\partial x}(-\frac{1}{2}gh^2) - gh\frac{\partial z_b}{\partial x}$$

from (2.68). The approximated vertical velocity w modifies the hydrostatic pressure distribution $p(z)$ by the pressure correction term p_c. This term also entails a depth-integrated pressure gradient term

$$S_{p_c} = \int\limits_{z_b}^{H} -\frac{1}{\rho}\frac{\partial p_c}{\partial x}\ dz. \tag{5.46}$$

Correcting the assumption of hydrostatic pressure by involving the pressure correction term p_c into the basic assumption of the SWE-derivation yields S_{p_c}, the depth integrated pressure correction, as an additional term on the right hand side of the SWE.

5.4.1   Calculation of S_{p_c} for Zeroth Order Approximation w_0

The zeroth order approximation w_0 results in the pressure distribution $p(z) = p_H + \rho(g + \tilde{g})(H - z)$ with pressure correction $p_c(z) = \rho\tilde{g}(H - z)$. The pressure correction gradient reads

$$\begin{aligned}
-\frac{1}{\rho}\frac{\partial}{\partial x}p_c &= -\frac{\partial}{\partial x}\left(\tilde{g}(H - z)\right) \\
&= \frac{\partial\tilde{g}}{\partial x}z - \frac{\partial}{\partial x}(\tilde{g}H) \tag{5.47}
\end{aligned}$$

where $\partial\tilde{g}/\partial x$ is the partial derivative of $\tilde{g}(x)$ with respect to x, where $\tilde{g}$ is assumed to be smooth enough for the derivation.

To obtain the additional term S_{p_c} for the momentum equation of the SWE, the pressure gradient is integrated over the water depth h

$$
\begin{aligned}
S_{p_c} = \int_{z_b}^{H} -\frac{1}{\rho}\frac{\partial}{\partial x}p_c \, dz \;\; &= \;\; \int_{z_b}^{H} \frac{\partial \tilde{g}}{\partial x}z - \frac{\partial}{\partial x}(\tilde{g}H) \, dz \\
&= \;\; \frac{\partial \tilde{g}}{\partial x}\frac{z^2}{2}\Big|_{z_b}^{H} - \tilde{g}\frac{\partial(h+z_b)}{\partial x}z\Big|_{z_b}^{H} \\
&= \;\; \frac{1}{2}\frac{\partial \tilde{g}}{\partial x}h(H+z_b) - \frac{\partial}{\partial x}(\tilde{g}h)h - \frac{\partial}{\partial x}(\tilde{g}z_b)h \\
&= \;\; -\frac{\partial}{\partial x}(\frac{1}{2}\tilde{g}h^2) + \tilde{g}hS_{bx}.
\end{aligned}
\tag{5.48}
$$

5.4.2 Calculation of $S_{p_c^1}$ for First Order Approximation w_1

The first order approximation w_1 entails the pressure correction term

$$
p_c^1(z) = \rho\tilde{g}^1(H-z) + \frac{1}{2}(\frac{\partial w_1}{\partial z})^2 + u\frac{\partial^2 w_1}{\partial z\partial x}(H^2 - z^2).
$$

Its pressure gradient reads

$$
\begin{aligned}
-\frac{1}{\rho}\frac{\partial}{\partial x}p_c^1 \;\; &= \;\; -\frac{\partial}{\partial x}\left(\tilde{g}^1(H-z)\right) - \frac{\partial}{\partial x}\left(\frac{1}{2}((\frac{\partial w_1}{\partial z})^2 + u\frac{\partial^2 w_1}{\partial z\partial x})(H^2 - z^2)\right) \\
&= \;\; \frac{\partial \tilde{g}^1}{\partial x}z - \frac{\partial}{\partial x}(\tilde{g}^1 H) - (\frac{1}{2}\frac{\partial}{\partial x}(\frac{\partial w_1}{\partial z})^2 + u\frac{\partial^2 w_1}{\partial z\partial x}H^2) \\
&\quad + \frac{1}{2}\frac{\partial}{\partial x}((\frac{\partial w_1}{\partial z})^2 + u\frac{\partial^2 w_1}{\partial z\partial x})z^2
\end{aligned}
\tag{5.49}
$$

where $\frac{\partial \tilde{g}^1}{\partial x}$ is the partial derivative of $\tilde{g}^1(x)$ with respect to x, where again $\tilde{g}^1$ is assumed to be smooth enough for the derivation.

$S_{p_c^1}$ is obtained by integration over the water depth h

$$
\begin{aligned}
S_{p_c^1} \;\; &= \;\; \int_{z_b}^{H} -\frac{1}{\rho}\frac{\partial}{\partial x}p_c^1 \, dz = \int_{z_b}^{H} \frac{\partial \tilde{g}^1}{\partial x}z - \frac{\partial}{\partial x}(\tilde{g}^1 H) \, dz \\
&\quad - \int_{z_b}^{H} (\frac{1}{2}\frac{\partial}{\partial x}(\frac{\partial w_1}{\partial z})^2 + u\frac{\partial^2 w_1}{\partial z\partial x}H^2) - (\frac{1}{2})\frac{\partial}{\partial x}((\frac{\partial w_1}{\partial z})^2 + u\frac{\partial^2 w_1}{\partial z\partial x})z^2 \, dz \\
&= \;\; -\frac{\partial}{\partial x}(\frac{1}{2}\tilde{g}^1 h^2) + \tilde{g}^1 hS_{bx} - \frac{\partial}{\partial x}(\frac{1}{2}((\frac{\partial w_1}{\partial z})^2 + u\frac{\partial^2 w_1}{\partial z\partial x})H^2)h \\
&\quad - \frac{\partial}{\partial x}(\frac{1}{6}((\frac{\partial w_1}{\partial z})^2 + u\frac{\partial^2 w_1}{\partial z\partial x}))(H^3 - z_b^3).
\end{aligned}
\tag{5.50}
$$

5.4.3 Structure of S_{p_c}

The source term S_{p_c} from (5.48) for the zeroth order approximation w_0 and in particular $S_{p_c^1}$ from (5.50) for the first order approximation w_1 are complicated and contain various derivatives. Since w depends on $\frac{\partial H}{\partial x}$ and $\tilde{g}$ depends on $\frac{\partial w}{\partial x}$, the term $\frac{\partial \tilde{g}}{\partial x}$ contains third order x-derivatives of H. Even considering the most simple case with a stationary solution $\frac{\partial}{\partial t} = 0$ and a plane bottom ($z_b = 0 \Rightarrow H = h$) indicates the complexity of S_{p_c}.

For this simplified case, the zeroth order approximation w_0 for the velocity reads

$$w_0 = \frac{w_H + w_b}{2} = \frac{1}{2}w_H = \frac{1}{2}u\frac{\partial h}{\partial x}h.$$

The acceleration correction $\tilde{g}$ reads

$$\tilde{g} = \dot{w} = u\frac{\partial w}{\partial x} = u\frac{\partial}{\partial x}\left(\frac{1}{2}u\frac{\partial h}{\partial x}\right) = \frac{1}{2}\left(u\frac{\partial u}{\partial x}\frac{\partial h}{\partial x} + u^2\frac{\partial^2 h}{\partial x^2}\right).$$

For the structure of S_{p_c} from (5.48), we obtain

$$
\begin{aligned}
S_{p_c} &= -\frac{\partial}{\partial x}\left(\frac{1}{2}\tilde{g}h^2\right) \\
&= -\frac{1}{2}\frac{\partial}{\partial x}\left(\frac{1}{2}\left(u\frac{\partial u}{\partial x}\frac{\partial h}{\partial x} + u^2\frac{\partial^2 h}{\partial x^2}\right)h^2\right) \\
&= -\frac{1}{4}\left(2u\frac{\partial u}{\partial x}h\frac{\partial h}{\partial x}\frac{\partial h}{\partial x} + 2u^2 h\frac{\partial h}{\partial x}\frac{\partial^2 h}{\partial x^2} + \frac{\partial u}{\partial x}\frac{\partial u}{\partial x}h^2\frac{\partial h}{\partial x} \right. \\
&\qquad \left. + u\frac{\partial^2 u}{\partial x^2}h^2\frac{\partial h}{\partial x} + 3u\frac{\partial u}{\partial x}h^2\frac{\partial^2 h}{\partial x^2} + u^2 h^2\frac{\partial^3 h}{\partial x^3}\right). \tag{5.51}
\end{aligned}
$$

This term contains x-derivatives of u up to 2^{nd}order and of h up to 3^{rd}order and various mixtures of them. Considered for real applications with time dependence and with varying bottom elevation $z_b(x) \neq const$, the structure of S_{p_c} in (5.51) becomes even more complicated. That is even worse for the first order approximation w_1 in $S_{p_c^1}$.

Since for general flow cases it is difficult to decide which terms in (5.51) are small compared to others, it is difficult to extract dominant terms and neglect others.

5.4.4 Inclusion of S_{p_c} in SWE

The inclusion of S_{p_c} in the x-momentum equation of SWE (2.72) changes the nonlinear first order PDE system into a highly nonlinear third order PDE system. Usually, the numerical solution of third order PDE requires the special

treatment of the highest order derivative. The numerical solution scheme applied in this thesis to solve the SWE (see Section 2.5.2) cannot be applied to that problem.

In Section 3.3 we have formulated the aim to develop extension based on the SWE and their numerical solution scheme (3.13). Instead of substituting the numerical solution scheme by another technique, we apply a splitting scheme and evaluate S_{p_c} at the end of a time step from the applied numerical solution scheme and treat S_{p_c} as a further source term.

Recognizing the danger of losing well-posedness of the problem due to that procedure, a regularization method is applied within the evaluation of S_{p_c} as presented in Section 5.5. The extended SWE read

$$\frac{\partial}{\partial t}\begin{pmatrix} h \\ uh \end{pmatrix} + \frac{\partial}{\partial x}\begin{pmatrix} uh \\ u^2 h + \frac{1}{2}gh^2 \end{pmatrix} = \begin{pmatrix} q \\ ghS_{bx} - ghS_{fx} + S_{p_c}. \end{pmatrix} \qquad (5.52)$$

Replacing S_{p_c} with $S_{p_c^1}$ yields the formulation for the first order approximation in analogy to (5.52).

Remark 5.10 $S_{p_c} = -\frac{\partial}{\partial x}(\frac{1}{2}\tilde{g}h^2) + \tilde{g}hS_{bx}$ *is similar to the pressure gradient term of the hydrostatic pressure distribution* $-\frac{\partial}{\partial x}(\frac{1}{2}gh^2) + ghS_{bx}$. *This term in the classical SWE is split into two terms: the conservative part* $-\frac{\partial}{\partial x}(\frac{1}{2}gh^2)$ *is inserted in the flux function and* $-gh\frac{\partial z_b}{\partial x} = ghS_{bx}$ *is applied as a source term on the right hand side of the SWE. In contrast to this procedure,* S_{p_c} *and* $S_{p_c^1}$ *are involved as pure source terms into the SWE. Although that* S_{p_c} *has the same structure, it is not considered as a conservative term following (3.13).*

Remark 5.11 *(5.52) represents the formulation of the SWE with the Extension* Pressure Correction *caused by approximations of vertical velocities w as zeroth order* w_0 *or first order* w_1 *approximations. The classical SWE approach assumes hydrostatic pressure, for the in-viscid case equivalent to* $\dot{w} = 0$ *due to Theorem 5.1. Then,* $\tilde{g}$ *and* S_{p_c} *vanish reducing (5.52) to the classical SWE (2.72).*

5.5   Regularization

Applying a splitting scheme to include S_{p_c} into the SWE entails the danger of losing well-posedness of the problem as discussed in the previous section. Thus, regularization methods are applied.

Furthermore, the approach of the Extension *Pressure Correction* p_c assumes smooth solutions where all derivatives exist and can be computed. The source term S_{p_c} contains third order x-derivatives of H requiring $H \in C^3$. For real flow problems $H \notin C^1$ may occur for some applications. We extend the approach to functions that do not have the desired regularity, e.g in case of weak solutions.

Even water levels $H \in C^\infty$ may cause problems, since various differentiations are involved in the computation of the term and differentiation is an ill-posed problem. Appendix A.5 provides an introduction to ill-posed problems.
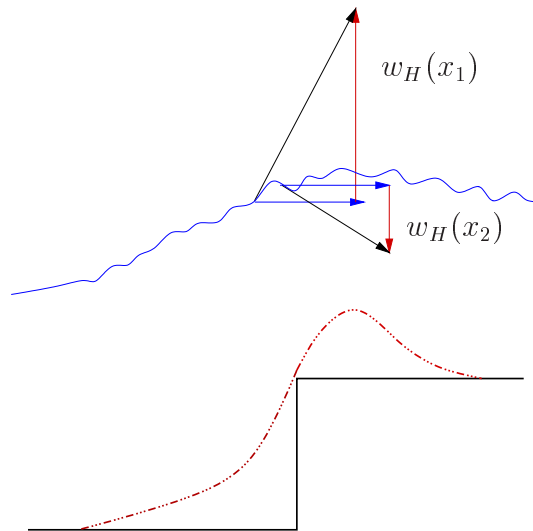
Figure 5.7: Problems with the estimation of vertical velocities $w(x)$

5.5.1   Differentiation as an Ill-posed Problem

The demand for regularization methods is demonstrated by a typical problem: It is possible that small waves occur in the water level $H(x)$, e.g. due to the inclusion of the additional source term S_{p_c} in the momentum equation. Assuming that these surface waves are represented by a sinus function with a small amplitude ($\epsilon \ll 1$) and a high frequency $\frac{n}{\epsilon}$ with large $n \gg 1$ disturbing

the water level $H_0(x)$, we obtain

$$H(x) = H_0(x) + \epsilon \ \sin(\frac{n}{\epsilon}x). \qquad (5.53)$$

The differences between H and H_0 are small and limited by ϵ:

$$\max_{x \in \Omega} |H - (H_0)| = \epsilon \qquad (5.54)$$

Since $w_H = f(H_x)$, the x-derivative of H is required for the estimation of the vertical velocity, yielding

$$\frac{\partial H}{\partial x} = \frac{\partial H_0}{\partial x} + n \ \cos(\frac{n}{\epsilon}x), \qquad (5.55)$$

which involves a large error

$$\max_{x \in \Omega} |\frac{\partial H}{\partial x} - \frac{\partial H_0}{\partial x}| = n. \qquad (5.56)$$

Figure 5.7 shows the problem: In front of the curb the average vertical velocity is positive since the water is lifted over the curb. The estimation of vertical velocity at the surface w_H results in highly oscillatory data due to the effects of the disturbing waves. w_0 derived as a zeroth order approximation of $\bar{w}$, yields also an oscillating function with positive and negative values despite the positivity of the vertical velocity in front of the curb.

Remark 5.12 *Continuing the calculations and estimating e.g. $\tilde{g}$ as depending on $\frac{\partial w}{\partial x}$, yields the inclusion of $\frac{\partial^2 H_0}{\partial x^2} - \frac{n^2}{\epsilon} \sin(\frac{n}{\epsilon}x))$ and thus even poorer results in particular for $\frac{\partial \tilde{g}}{\partial x}$.*

Similar problems occur in case of weak solutions e.g. for the dam break problem. Weak solutions are only integrable and generally $\notin C^1$, at times $\notin C^0$. They fulfill only the integral form of the equation and generally not the differential form, since the derivatives do not exist everywhere. The numerical differentiation of such functions yields not reliable results and special treatments are required (e.g. ENO-schemes [19]).

Furthermore it is possible that even if the SWE solution is regular enough to compute the pressure correction gradient term S_{p_c}, its impact on the SWE produces less regular solutions or oscillations. The applicability of the Extension *Pressure Correction* depends on the stability and robustness of the numerical differentiation. Näf [31] did struggle with similar problems.

5.5.2 Mollification Methods

The presented consideration of the vertical velocities w, the dynamical pressure p_c and the source term S_{p_c} and their estimations are approximations. We can neither expect that these approximations can resolve local phenomena as small surface waves nor are we interested in these small scale phenomena.

To obtain a stable and robust estimation of the vertical velocities we smooth H, z_b and u appropriately to make them more regular in order to enable the calculation of the derivatives involved in (5.48) and (5.50).

Following [29], mollification methods can solve the problems we have presented in the previous section. They smooth functions $\notin C^1$ into functions $\in C^\infty$ and smooth effects of disturbances.

Definition 5.13 *For any locally integrable function* $f : \mathbb{R}^n \supseteq \Omega \to \mathbb{R}$, *the mollifier* J_δ *is defined by*

$$J_\delta f(x) = \int\limits_{\mathbb{R}^n} m_\delta(x - y) f(y) dy \qquad (5.57)$$

with the nonnegative function $m_\delta : \mathbb{R}^n \to \mathbb{R}$ *given for any* $\delta > 0$ *such that*

1. $m_\delta \in C^\infty(\mathbb{R}^n)$,

2. $m_\delta(x) = 0$ *for* $||x|| \geq \delta$ *and* $m_\delta(x) \geq 0$ *for* $||x|| < \delta$,

3. $\int_{\mathbb{R}^n} m_\delta(x) \, dx = 1$.

For example, m_δ can be the function

$$m_\delta(x) = \begin{cases} C \ \exp[-\frac{1}{\delta - ||x||^2}], & for \quad ||x|| < \delta, \\ 0, & for \quad ||x|| \geq \delta, \end{cases} \qquad (5.58)$$

where C is a suitable constant chosen such that $\int_{\mathbb{R}^n} m_\delta(x) \, dx = 1$. We may also choose a Gaussian curve $m_\delta = \tilde{C} \ \exp(-\delta ||x||^2)$ for m_δ instead of (5.58).

Remark 5.14 *If* $f \in L^p(\mathbb{R}^n)$, $J_\delta f(x) = (m_\delta * f)(x)$ *is the convolution of* f *and* m_δ.

Theorem 5.15 *Let* $f : \mathbb{R}^n \supseteq \Omega \to \mathbb{R}$ *be a locally integrable function. Then* $J_\delta f \in C^\infty(\Omega)$

Proof. [29], p.219 ∎

Choice of m_δ and δ

The mollifier J_δ depends on the choice of the smoothing function m_δ and in particular on the choice of δ. δ is the parameter to control the strength of the mollification process. In the limit $\delta \to 0$ there is no mollification at all and for a $f \in L^p(\mathbb{R}^n)$ it can be shown ([29], p.220) that $lim_{\delta \to 0} ||J_\delta f - f||_{p,\Omega} = 0$

In the other limit $\delta \to \infty$, f is smoothed to a constant function everywhere.

The right choice of $\delta > 0$ is the truly crucial point in the theory of regularization. Chosen too low, the problems remain, and chosen too large, important information of the function f is lost.

We proceed with this problem practically: Since we can not expect to involve the source term S_{p_c} from (5.48) without mollification, we choose δ as minimal as we can to receive a stable numerical procedure.

5.5.3 Other Regularization Methods

Beside the applied mollification method we have also tested other methods of regularization:

- low pass filter method included in a Fourier analysis and

- spline approximation.

In particular we tested the low pass filter method: The function is resolved in its frequencies by a Fourier analysis. The low pass filter cuts all frequencies higher than a selected frequency, that can be understood as the regularization parameter. The smoothed function is reconstructed out of the reduced frequencies by an inverse Fourier transformation. One reason for testing this method is that we are interested in derivatives of smoothed functions. An advantage of the Fourier analysis is that a function developed in a Fourier base can be derivated easily by shifting coefficients only. Numerical tests for this regularization method gave bad results with so-called Gibbs phenomenon (oscillations) at the boundaries. For periodic data, the method approved very good results instead. Since the vertical velocity can not be expected to be periodic, this method cannot be applied.

A similar procedure is the singular value decomposition of the considered operator and cutting the spectrum of the operator. Due to the bad results with the Fourier method, this procedure was not implemented.

A further way to smooth the function is to use spline approximations and to minimize the sum of the approximation errors and a variation punishing functional. This procedure (even if parts of the numerics are given in libraries as NAG) is very costly and did not result in as good results as operating the

mollifiers.

Thus, compared to other methods implemented and tested, the mollifier method is chosen since best results were obtained. Furthermore, its implementation is easy to include into the numerical solution scheme of the SWE.

5.5.4 Application to S_{p_c}

The mollification method is applied several times in the computation of S_{p_c} in (5.48). The first time for the calculation of the vertical velocities at the free surface w_H and at the bottom w_b. Here the mollification of H and z_b yields smooth derivatives. Furthermore, the horizontal flow velocity u is mollified. In addition to these required mollifications, each derivation process is prepared by a mollification in order to ensure smooth solutions.

Remark 5.16 *Since the mollification method is applied several times, each mollification can be controlled by a separate mollification parameter δ. Due to restricted research time, no numerical exploration of what might be the best strategy for the best solution was performed. We applied the same δ yielding suitable solutions.*

5.6 Results with Extension *Pressure Correction*

Since the first order approximation term $S_{p_c^1}$ required an enormous effort of regularization increasing the computational effort enormously, we decided to present only the solutions with the zeroth order approximations.

5.6.1 Flow Problem *Manhole*

The introduction of the separated vortex regions has increased the height of the water column above the manhole even over the height of the NSE. This height is decreased by the additional source term included by the Extension *Pressure Correction* yielding satisfying agreements between the NSE benchmark solution and the extended SWE results illustrated in Figure 5.8.

Figure 5.9 compares the SWE-solutions with and without Extension *Pressure Correction* and illustrates the effects of the source term S_{p_c}. The integral of $S_{p_c}(x)$ over parts of the domain is not zero. At the inflow interval and the increasing part of the vortex the water is accelerated yielding a decrease in the

water level. At the decreasing part of the vortex, the flow has a negative acceleration. The vertical momentum of the in-flowing water from the manhole is included via S_{p_c} in contrast to the classical SWE.
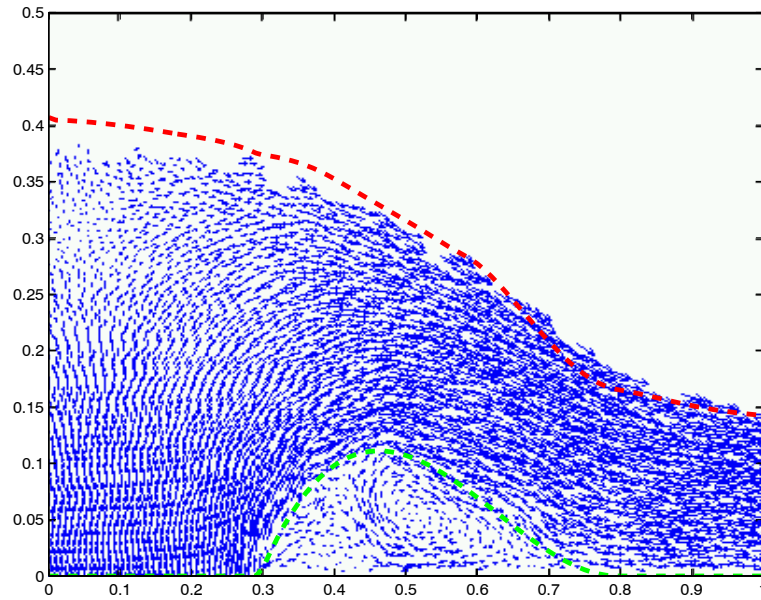

Figure 5.8: Water and ground level (vortex region) for the flow problem *manhole* with Extension *Vortex Separation* and Extension *Pressure Correction* compared to the NSE benchmark solution for $w_b = 1m/s$
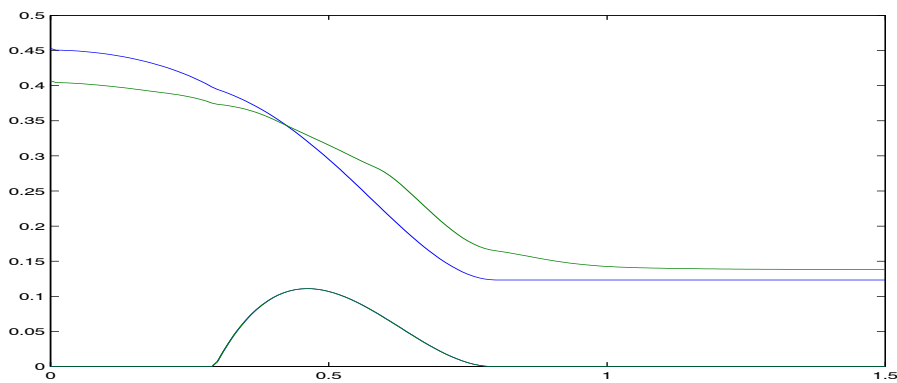

Figure 5.9: Comparison of SWE-solutions for the flow problem *manhole* with and without Extension *Pressure Correction*
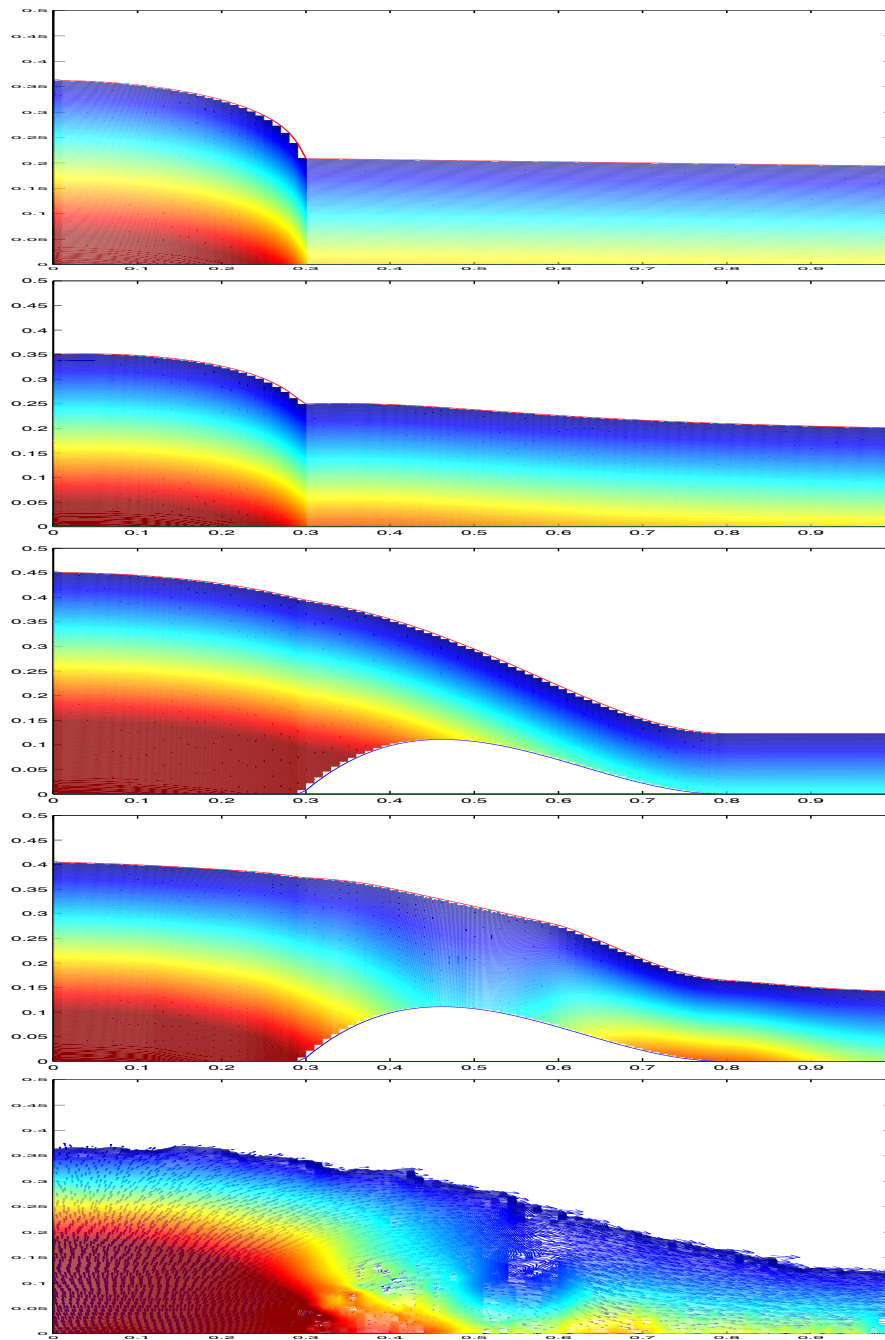
Figure 5.10: Comparison of pressure distribution as colored plots with values from 0 in blue to high value in red for different model approaches of flow problem *manhole* ($w_b = 1m/s$). ¿From top to bottom: classical SWE, SWE+Extension *Pressure Correction*, SWE+Extension *Vortex Separation*, SWE+Extension *Vortex Separation*+ Extension *Pressure Correction*, NSE-benchmark solution

The effects of the extensions are illustrated in Figure 5.10 comparing the pressure distributions as colored plots for the following model approaches

1. classical SWE,
2. SWE + Extension *Pressure Correction*,
3. SWE + Extension *Vortex Separation*,
4. SWE + Extension *Vortex Separation* + Extension *Pressure Correction*,
5. NSE-benchmark solution

The pressure is presented in all plots by the same color levels from blue for zero over green, yellow to red for high pressures.

There are two possibilities to assess the results: First by comparing the water levels given by the upper boundary of the colored domain and second by comparing the colors in the flow domain. The result with the classical SWE is far away from the NSE benchmark solution that is in good agreement with the extended SWE (SWE + Extension *Vortex Separation* + Extension *Pressure Correction*).
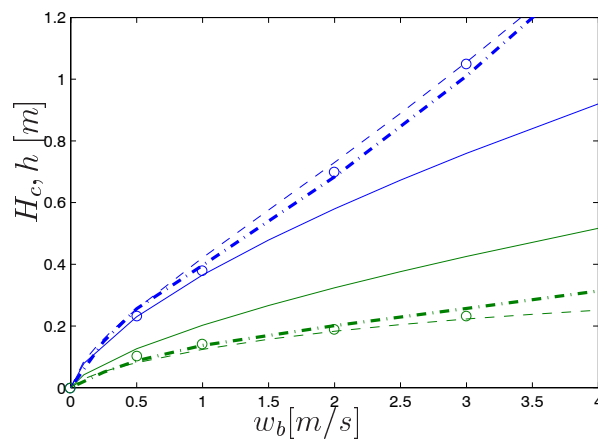

Figure 5.11: Comparison of dependencies of H_c (blue) and h (green) on the inflow velocity w_b from analytical considerations (dashed line), from classical SWE (solid line), from extended SWE (dashed-dotted) and from the NSE benchmark solutions (circles)

Figure 5.11 includes the results of the extended SWE into Figure 3.7, and presents the dependencies of the water column hight H_c and outflow hight h_o from the vertical inflow velocity w_b for the analytical solution, the NSE benchmark solution, the classical SWE and the extended SWE (SWE+Extension *Vortex Separation*+ Extension *Pressure Correction*). It is obvious that the results of the extended SWE are in much better agreement to the analytical considerations and the NSE benchmark results than the classical ones.

5.6.2   Flow Problem *Curb*

The introduction of the separated vortex regions increases the water level in front of the curb and decreases it at top of the vortex region yielding satisfying agreements between the NSE benchmark solution and the extended SWE results illustrated in Figure 5.12.
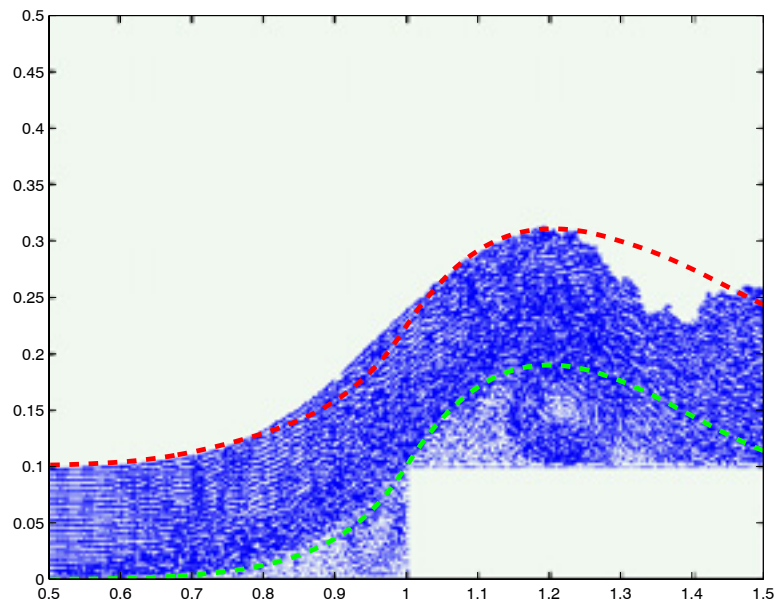

Figure 5.12: Water and ground level (vortex region) for the flow problem *curb* with Extension *Vortex Separation* and Extension *Pressure Correction* compared to the NSE benchmark solution for $u_0 = 3m/s$
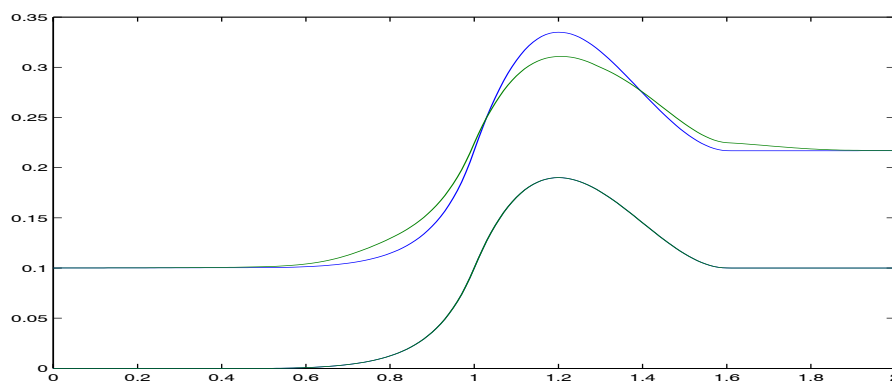

Figure 5.13: Comparison of SWE-solutions for the flow problem *curb* with and without Extension *Pressure Correction*

Figure 5.13 compares the SWE-solutions with and without Extension *Pressure Correction* and illustrates the effects of the source term S_{p_c}. The integral of $S_{p_c}(x)$ over the domain is zero. Thus, the effects of the Extension *Pressure Correction* are restricted to the local flow behavior. Nevertheless, the local differences in 2D may influence the global flow behavior as well.

The success of the extensions is also visible in the comparison of the pressure distributions: Figure 5.14 illustrates the pressure distribution as colored plots for the following model approaches

1. classical SWE,

2. SWE + Extension *Pressure Correction*,

3. SWE + Extension *Vortex Separation*,

4. SWE + Extension *Vortex Separation* + Extension *Pressure Correction*,

5. NSE-benchmark solution.

The pressure is presented by the color where the same color levels (from blue for zero over green, yellow to red for high pressure) are applied for all plots.

As for the flow problem *manhole*, there are two possibilities to assess the results: First by comparing the water level given by the upper boundary of the colored domain and second by comparing the colors in the flow domain. The results with the classical SWE are rather far away from the NSE benchmark solution that agrees with the extended SWE (SWE + Extension *Vortex Separation* + Extension *Pressure Correction*).

The water level is also rebuilt reasonably with the extended SWE (SWE + Extension *Vortex Separation* + Extension *Pressure Correction*). This success shows the potential of the extensions to model the real flow behavior (i.e. NSE benchmark solution) reliably within reduced computational effort. The CPU times of the SWE are almost doubled due to the effort of the mollification method, but remain still only fractions of the NSE effort.

Remark 5.17 *The real flow behavior from the NSE solutions for the flow problem* curb *is dynamic as explained in the presentation of the Extension* Vortex Separation. *Thus, the emphasis of the success of the Extension* Pressure Correction *is set on the flow problem* manhole.
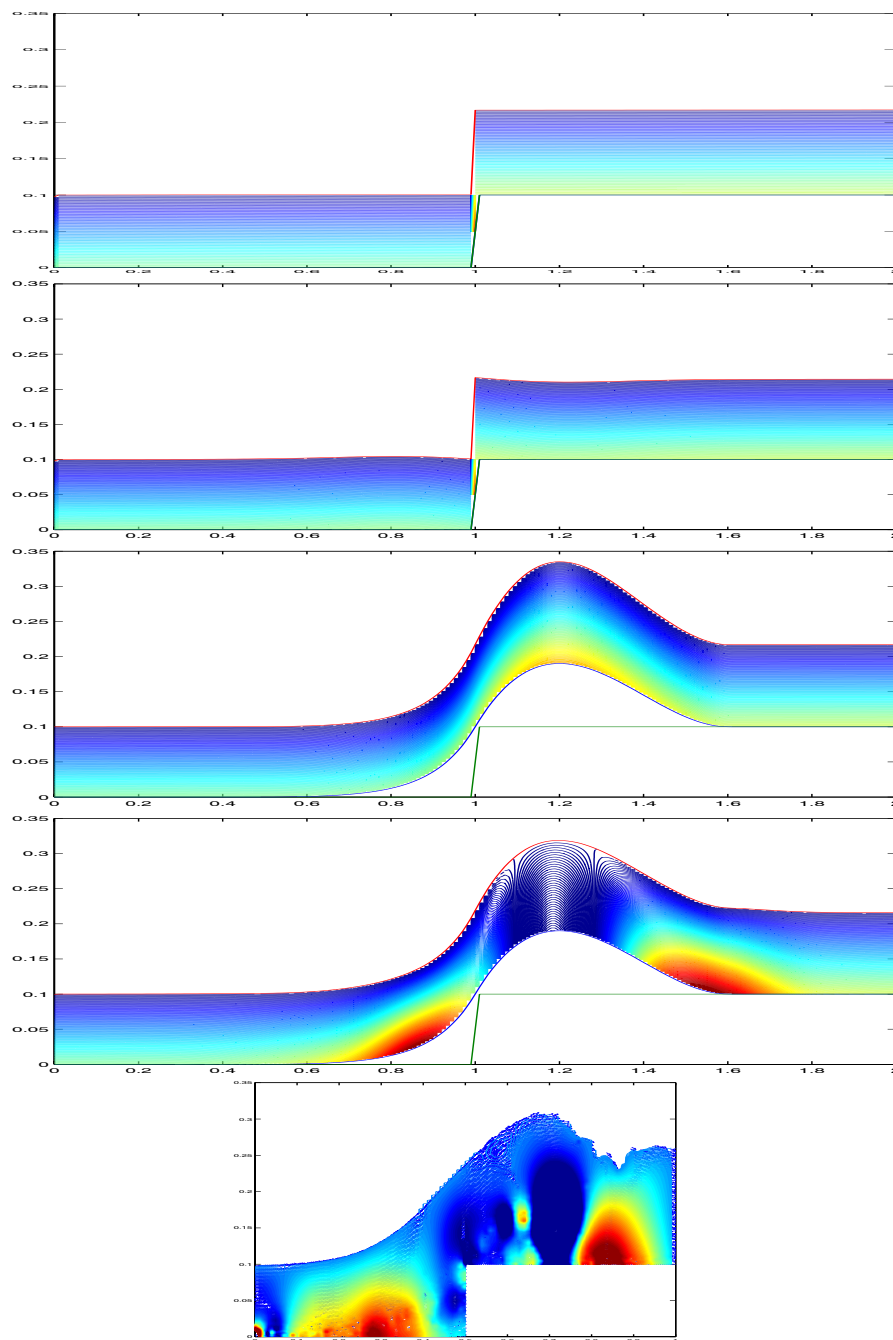
Figure 5.14: Comparison of pressure distribution as colored plots with values from 0 in blue to high values in red for different model approaches of flow problem *curb* ($u_0 = 3m/s$). ¿From top to bottom: classical SWE, SWE+Extension *Pressure Correction*, SWE+Extension *Vortex Separation*, SWE+Extension *Vortex Separation*+ Extension *Pressure Correction*, NSE-benchmark solution

5.6.3   Avalanche Modeling

As presented in [24], the SWE are also applied for simulation of avalanches. The friction approach is modified, but the main flow behaviors are similar. The picture on the left side of Figure 5.15 illustrates an avalanche flowing down a hill.
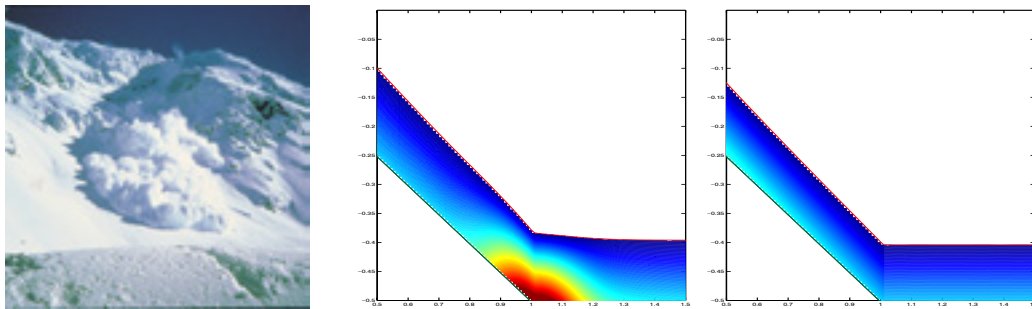

Figure 5.15: Example of an avalanche (left hand side), pressure distribution of test calculation with pressure correction (middle) and without Extension *Pressure Correction* (i.e. classical SWE with pure hydrostatic pressure, right hand side)

A critical situation in the flow process of an avalanche is its arrival from a hill at a flat region in the valley, e.g. the boundary of a village. The flow behavior in that critical region determines how much momentum from the hill is transferred into the valley and how far the avalanche can flow. Thus, the reliable simulation of this flow process is essential for a precise forecast of the avalanche danger for the valley.

At this critical point, the slope decreases from a high value to almost zero. In order to estimate the effects of the Extension *Pressure Correction* for the flow behavior of avalanches, the results of the classical SWE and the extended SWE are compared for such a typical flow situation in Figure 5.15. The pressure distributions are presented in the colored plots with the same color levels as in Figure 3.13.

In the classical SWE, no increase of the pressure is observed as obvious in the extended SWE solution. Since the flow velocity is re-oriented in that point, high pressure values are expectable according to the solution of the extended SWE. Such differences become crucial in particular when erosion models are involved that are coupled to the pressure as an important physical parameter of that process.

Chapter 6

Extensions in 2D

In Figure 2.2, we have given an overview over model approaches for the free surface flow of water. The approaches on the left hand side describe the flow behavior in 3D and those on the right hand side are restricted to 2D-profiles. In Chapter 3 we have compared the numerical results of 2D-NSE, 1D-SWE and stationary analytical solutions for 2D-Euler Equations. Due to the described discrepancy of 1D-SWE to the 2D-NSE/2D-Euler results (see Section 3.3), we have developed the Extensions *Vortex Separation* and *Pressure Correction* in the Chapters 4 and 5 respectively. Thus, we could decrease the discrepancies and rebuild the flow behavior more realistically.

This chapter starts with a presentation of the flow problems in 3D and their solution with the classical 2D-SWE. We advance the derivations of the Extension *Vortex Separation* of Chapter 4 and the Extension *Pressure Correction* of Chapter 5 into 2D and compare their results to the classical ones.

6.1 Results with Classical 2D-SWE

We recall the introduction of the flow problems in Section 1.2. Figure 1.4 illustrates the 2D-profile of the 3D flow problems presented in Figure 1.3. We first emphasize the differences between the 2D-profile flow problem before we present the numerical solution of the 3D-problem.

The 2D-SWE (2.70) are solved numerically with the scheme briefly presented in Section 2.5.2. The discretizations grid of the finite volume scheme is rectangular, in our case chosen quadratic with $dx = dy = 0.05m$.

6.1.1 Flow Problem *Manhole*

Figure 3.1 in Section 3.1 sketches the considered 2D-profile flow problem. In fact, this flow problem does not describe exactly the 3D outflow of water from

a manhole. Despite the real 3D flow problem is cylinder-symmetrical, we have considered the 2D-profile flow problem without appropriate source terms describing the decreasing flux uh with increasing distance to the center of the manhole as included in in the cylinder symmetric form of the 1D-SWE (2.77).
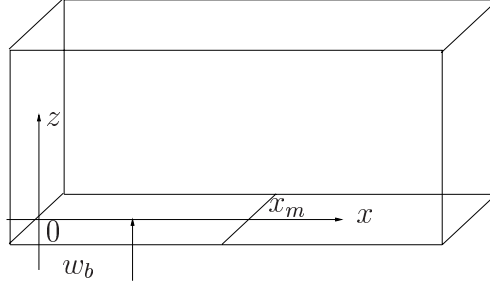

Figure 6.1: Sketch of the flow problem *manhole* as a 2D-profile without consideration of the cylinder-symmetric source terms as inflow from a rectangular area into a bordered rectangular channel

In fact, the consideration of the flow problem without the source terms describes the inflow from a rectangular manhole into a channel as illustrated in Figure 6.1.1. We have decided to apply the classical 1D-SWE (2.72) without the cylinder-symmetric source terms since it is more practical to compare uniform stationary solutions without decreasing flux.

For the 3D flow problem, we assume a free outflow at the borders of the computational domain $\Omega = [-2m, 2m] \times [-2m, 2m]$ and set a source term for the vertical inflow velocity $q = w_b$ in the area of the manhole. This area A_m is bordered by a circle with radius $x_m = 0.3m$ around the center of the manhole in $x_0 = (0, 0)$. We discretize A_m in the quadratic computational grid by the union of all grid cells with midpoint distance to the center low or equal to x_m.

Figure 6.2 illustrates the stationary 2D-SWE-solution of the flow problem *manhole* with vertical inflow velocity $w_b = 2m/s$. The principle flow behavior is similar to the 1D case: A water column is rising above the manhole and water is distributed over the street.

Figure 6.3 compares a cut through the 2D-SWE results (blue line) with the computed 1D cylinder-symmetric results (green line) showing almost identical results. The red line above these lines illustrates the 1D-SWE results of Chapter 3 also with $w_b = 2m/s$.

The water column H_c with 2D-SWE is lower as in the 1D case. The water level H far away from the center of the manhole does not remain constant but decreases with the distance to the center of the manhole. This is due to the neglect of the cylinder-symmetric source terms.
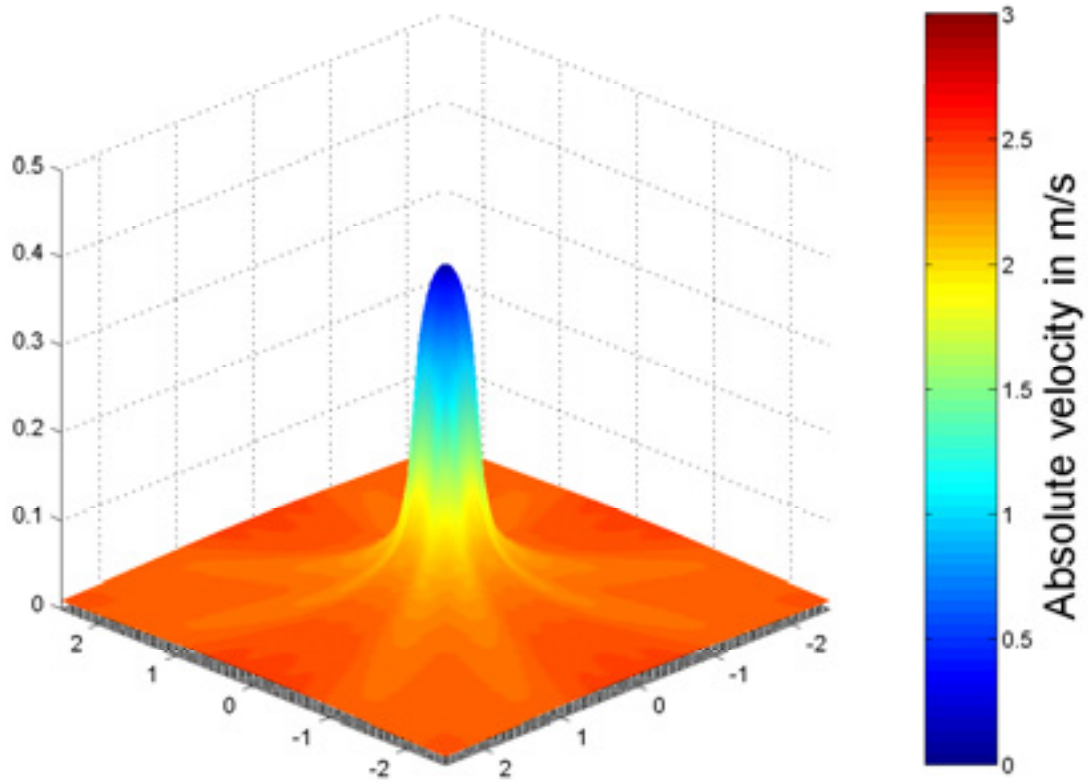
Figure 6.2: SWE results as water levels $H(x, y)$ with colored absolute velocities in the steady state solution
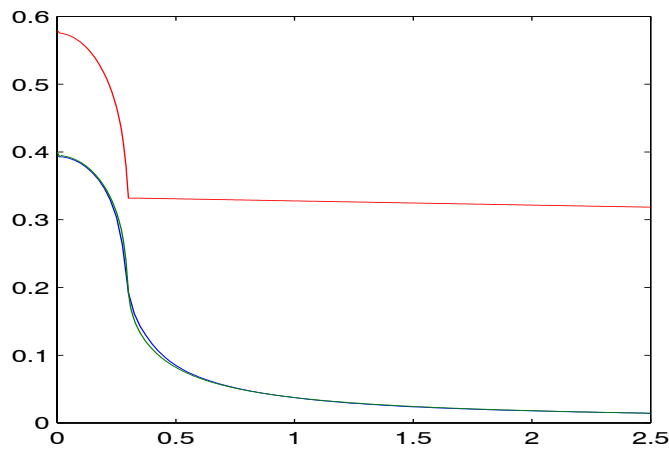

Figure 6.3: Comparison of a cut through the 2D-SWE results (blue line) with the 1D cylinder-symmetrical results (green line) and the 1D-SWE results of Chapter 3 for $w_b = 2m/s$

The applicability of the numerical solution scheme is demonstrated in Figure 6.4 by comparing its solution for a circular dam break problem to a published solution presented in [27]. The initial condition of the circular dam break are chosen as

$$H\left(t=0, x, y\right) = \begin{cases} h_i = 1.0m & , \sqrt{x^2 + y^2} \leq 0.3m \\ h_o = 0.1m & , \ else. \end{cases} \tag{6.1}$$

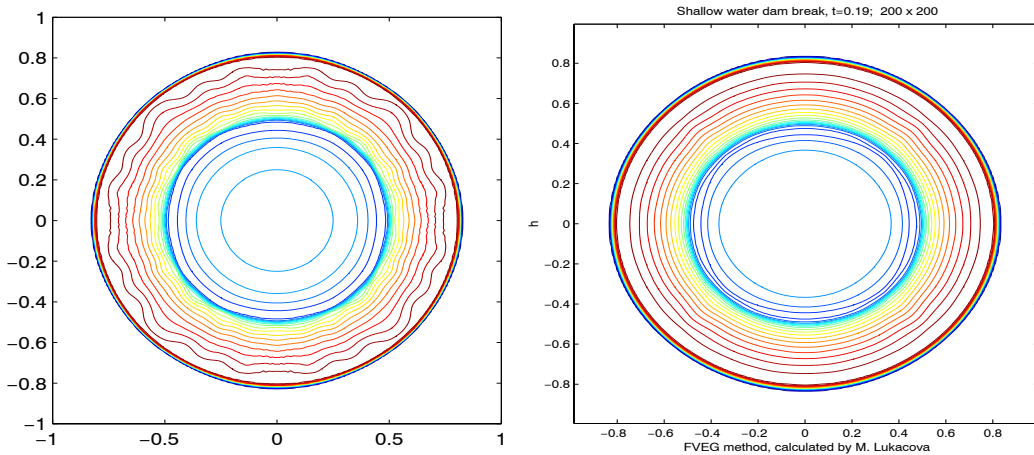Our numerical solutions are in agreement with those from literature.

Figure 6.4: Comparison of contour plot of water levels of a circular dam break ($h_i = 1.0m$ for $x < 0.3m$, $h_0 = 0.1m$ else at t=0s). Left: numerical 2D-SWE solution at $t = 0.19s$, right: analog solution from [27]

6.1.2   Flow Problem *Curb*

Considering the flow problem *curb* as a 2D-profile as done in Section 3.2 does not offers the possibility to include flow transversal to the profile. The inflowing water -even if reflected in the sub-critical flow case- is finally forced over the curb. This simulates in fact the flow over a step in a bordered channel as illustrated in Figure 6.5.

Similar to the neglect of cylinder-symmetric source terms in the flow problem *manhole*, we choose this physically modifying simplifications in order to concentrate on the flow problem and to restrict the difficulties.

Figure 6.6 illustrates the real 3D application of water flow over a curb. In contrast to the 2D-profile problem, water flows in both horizontal directions and only a part of the water floods the sidewalk. The other part is reflected and flows transversal to the former flow direction. If the height h_i and the
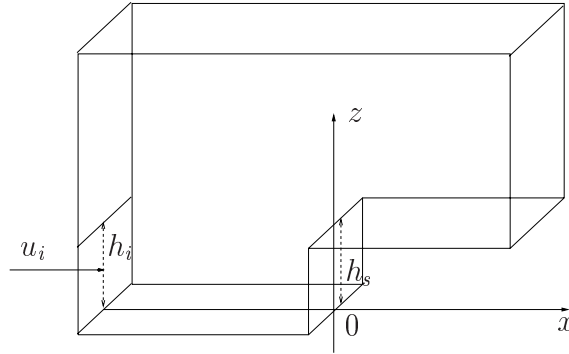
Figure 6.5: Sketch for illustration of the 2D-cut for the flow problem *curb*

momentum $u_i h_i$ of the water flowing towards the curb are too low, there is no flow over the curb at all.
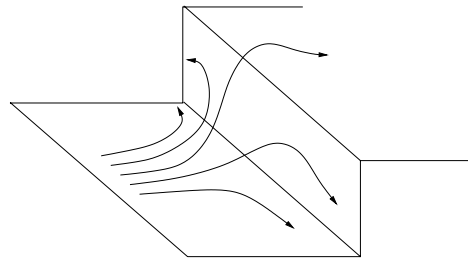
Figure 6.6: Sketch of the flow over a curb in a real 3D application

Instead of considering the flow problem *curb* isolated from the flow problems *manhole* as done for the 1D-SWE, we couple both problems in 2D. Figure 6.7 illustrates the bottom elevation z_b of the flow problem curb in 2D, where the manhole is assumed to be located at the center of the street. We define $\Omega = [-5m, 5m] \times [-5m, 5m]$ and set a source term for the vertical inflow velocity $q = w_b$ in the area of the manhole. This area A_m is bordered by a circle with radius $x_m = 0.3m$ around the center of the manhole in $x_0 = (0, 0)$. The curb with the step-size $h_s = 0.1m$ is located at $x = 3m$ and $x = -3m$. Thus we receive the bottom elevation

$$z_b(x, y) = \begin{cases} 0.0m & , -3m < x < 3m \\ h_s = 0.1m & , else. \end{cases} \tag{6.2}$$

Similarly to the 1D case, the curb is not modeled as a step of infinite slope but as a jump in between one computational grid cell on the x-dimension.
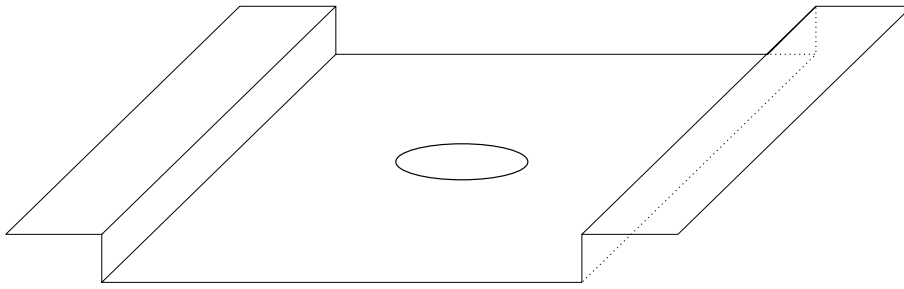
Figure 6.7: Bottom structure of the flow problem *curb* in 3D as the topography of the street with sidewalks and the manhole in the middle of the street

Figure 6.8 illustrates the stationary results where the sidewalks are flooded. In contrast to the 1D flow problem, where all the water is finally forced to flow over the curb, a fraction of the water flows over the curb and the other fraction is flowing below the level of the sidewalk on the street transversal to the curb as already sketched in Figure 6.6.
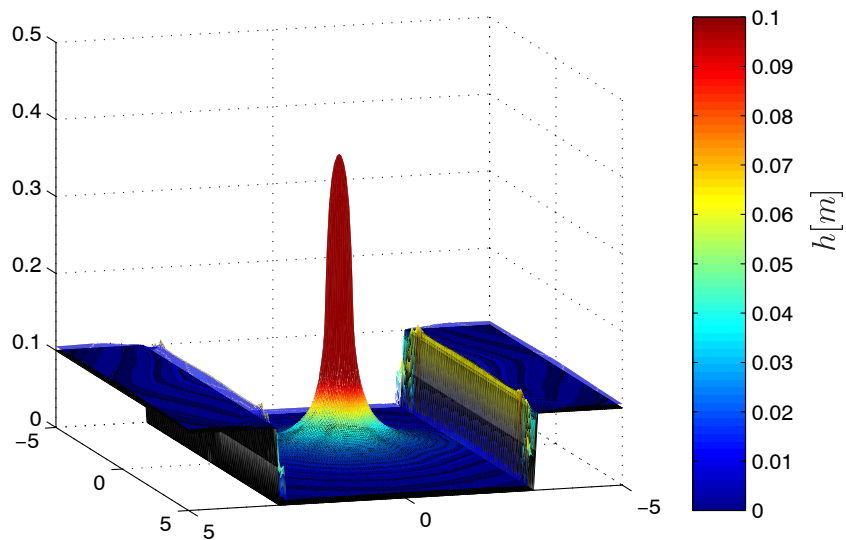
Figure 6.8: SWE results as colored water depths $h(x, y)$ in the stationary solution with flooding of the sidewalks

6.2   Extension *Vortex Separation* in 2D

The Extension *Vortex Separation* separates vortex regions at the bottom as
dead zones defining the new bottom for the main flow above. This approach
is also applicable for 3D flow problems modeled with 2D-SWE. In Chapter
4, a physical design approach of the separation line $s(x)$ for extensions of
the 1D-SWE is presented. The 1D separation line is extended to a function
$s(x, y)$ in 2D with vortex regions below that function above the ground $z_b(x, y)$.

The physical design approach in Chapter 4 is directly applicable to the flow
problem *manhole*. We consider the problem in cylinder-symmetry reduced in
1D and exchange the horizontal flow velocity u_{SWE} by the radial one. Figure
6.9 illustrates the resulting vortex region for the flow problem *manhole* for
$w_b = 2m/s$.
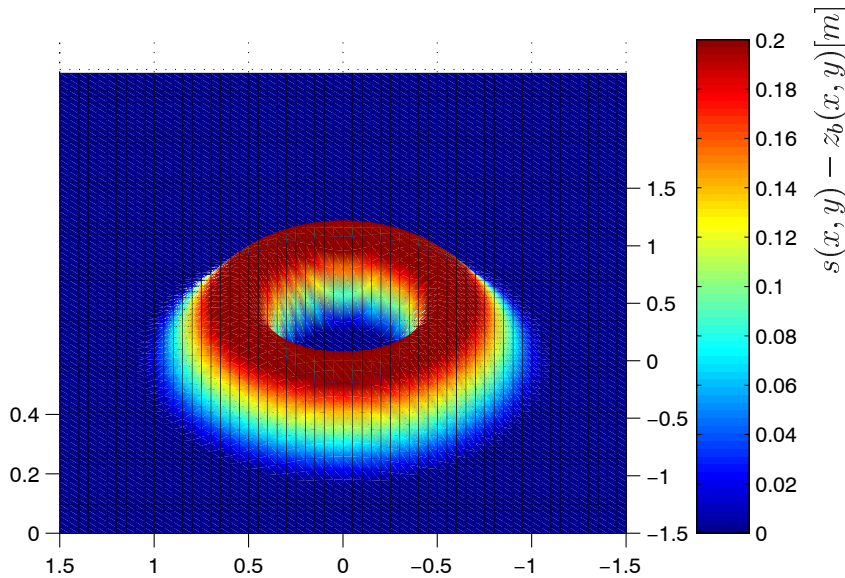
Figure 6.9: Example of the Extension *Vortex Separation* for the flow problem
manhole with 2D-SWE

The physical design approach for the vortex region from 1D can also be
applied to the flow problem *curb* in 2D. Figure 6.2 illustrates how to advance
the Extension *Vortex Separation* from 1D to 2D. We consider the 2D-problem
as a union of 1D-problems oriented perpendicular to the curb and decompose
the velocity vector into a normal component $\vec{u}_n$ and a tangential component
$\vec{u}_t$. The normal component $\vec{u}_n$ determines the design of the vortex region as
done in 1D.

The design of the separated vortex region depends on the 2D-distribution
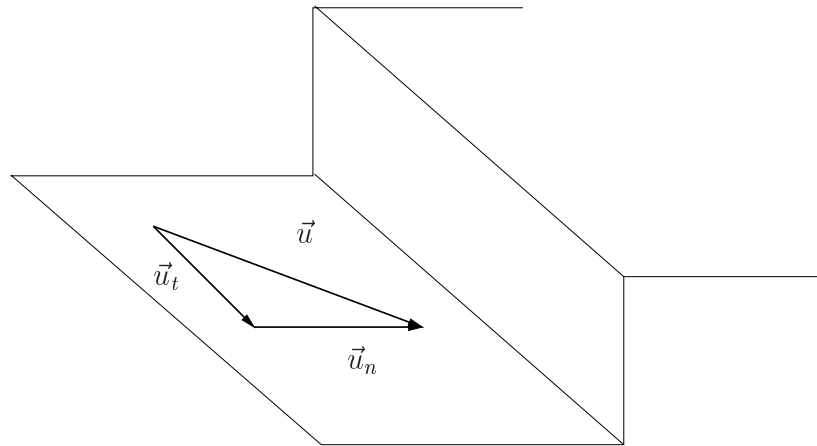
Figure 6.10: Consideration of the normal component $\vec{u}_n$ to advance the Extension *Vortex Separation* for the flow problem *curb* from 1D into 2D

of the velocity in front of the curb. Due to the coupling of the flow problems we obtain a cylinder-symmetric flow from the manhole determing the normal component in front of the curb. Figure 6.11 illustrates an example for the vortex region at the curb in 2D.

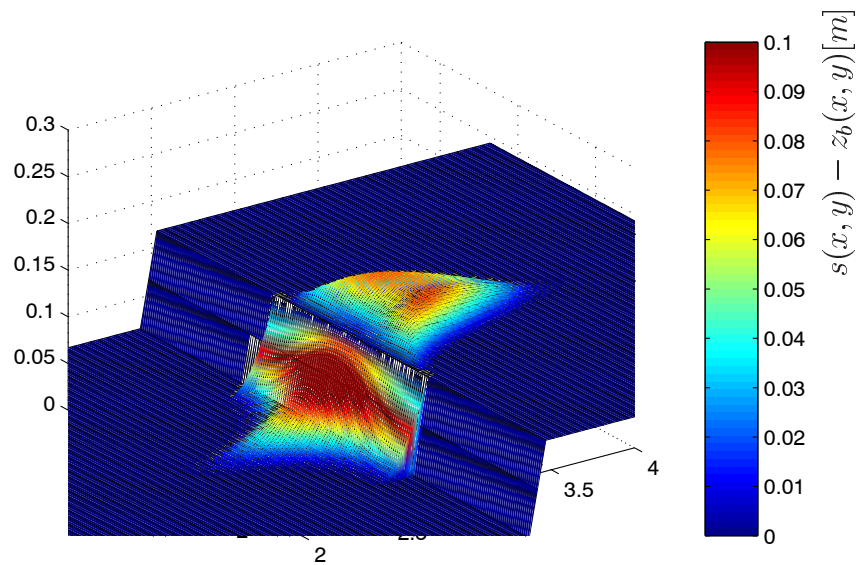Figure 6.11: Example of the Extension *Vortex Separation* for the flow problem *curb* with 2D-SWE

6.3 Extension *Pressure Correction* in 2D

The Extension *Pressure Correction* derived in Chapter 5 for the 1D-SWE is also applicable to the 2D-SWE. The most important steps of its derivation in 2D are presented below.

6.3.1 Approximation of Vertical Velocities w

Vertical Velocity w_H at the Surface and w_b at the Bottom

Following Section 5.2, the vertical velocities $w(x, y)$ are approximated by the kinematic boundary conditions. At the surface H and the bottom z_b, no penetration of water into the ground and the air is assumed. The equations (2.10) and (2.11) extended for a time dependent bottom $z_b(t, x, y)$ read

$$w_H = \frac{\partial H}{\partial t} + u_H \frac{\partial H}{\partial x} + v_H \frac{\partial H}{\partial y},$$
$$w_b = \frac{\partial z_b}{\partial t} + u_b \frac{\partial z_b}{\partial x} + v_b \frac{\partial z_b}{\partial y} + q.$$

As was done for u in (5.6) and illustrated in Figure 5.3, we assume also $v_H = v_b = \bar{v} = v$. This yields

$$w_H = \frac{\partial H}{\partial t} + u \frac{\partial H}{\partial x} + v \frac{\partial H}{\partial y}, \tag{6.3}$$

$$w_b = \frac{\partial z_b}{\partial t} + u \frac{\partial z_b}{\partial x} + v \frac{\partial z_b}{\partial y} \tag{6.4}$$

for the vertical velocities at the free surface (6.3) and at the bottom (6.4). Identical to (5.10),

$$w_b(x, y) = q(x, y) \tag{6.5}$$

is assumed as the prescribed vertical inflow velocity at the bottom in the area of the manhole.

Vertical Distribution $w(z)$

Departing from the estimation of the vertical velocity w at the surface w_H (6.3) and the bottom w_b (6.4) the vertical distribution $w(z)$ is approximated as zeroth order approximation w_0.

$$w(x, y, z) = \bar{w}(x, y) = w_0(x, y) = \frac{w_H(x, y) + w_b(x, y)}{2}. \tag{6.6}$$

$w_0(x, x)$ is chosen as the average of the vertical velocities at the surface w_H and the bottom w_b estimated in (6.3) and (6.4) in analogy to the approach in

1D.

Vertical Velocities w_0 for the Flow Problem *Manhole*

The vertical velocities $w_0(x, y)$ for the flow problem *manhole* is illustrated in Figure 6.12 for $w_b = 2m/s$. The 2D distribution is in agreement with the results of the 1D cylinder symmetric computations.
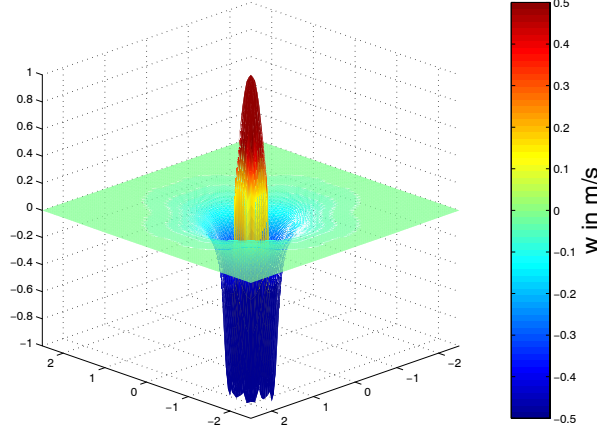
Figure 6.12: Vertical velocity for the 2D flow problem *manhole*

6.3.2   Pressure Correction p_c

In analogy to the 1D-SWE, the approximated vertical velocities entail a correction of the hydrostatic pressure distribution

$$p(z) = p_H + \rho g(H - z) + \rho \tilde{g}(H - z) = p_{hy} + p_c. \tag{6.7}$$

where

$$p_c(z) = \rho \tilde{g}(H - z). \tag{6.8}$$

is the pressure correction. The acceleration correction $\tilde{g}$ reads in 2D:

$$\tilde{g} = \dot{w} = \frac{\partial w}{\partial t} + u\frac{\partial w}{\partial x} + v\frac{\partial w}{\partial y}. \tag{6.9}$$

6.3.3   Impact of Dynamical Pressure p_c on SWE: S_{p_c}

The pressure correction term p_c entails depth-integrated pressure correction gradient terms $S_{p_{cx}}$ and $S_{p_{cy}}$ as additional terms in the x- and y-momentum

equations of the SWE:

$$S_{p_{cx}} = -\frac{\partial}{\partial x}(\frac{1}{2}\tilde{g}h^2) + \tilde{g}hS_{bx}, \tag{6.10}$$

$$S_{p_{cy}} = -\frac{\partial}{\partial y}(\frac{1}{2}\tilde{g}h^2) + \tilde{g}hS_{by}. \tag{6.11}$$

These terms are derived similarly to the 1D case.

The extended 2D-SWE read

$$\frac{\partial}{\partial t}\begin{pmatrix} h \\ uh \\ vh \end{pmatrix} + \frac{\partial}{\partial x}\begin{pmatrix} uh \\ u^2h + \frac{1}{2}gh^2 \\ uvh \end{pmatrix} + \frac{\partial}{\partial y}\begin{pmatrix} vh \\ uvh \\ v^2h + \frac{1}{2}gh^2 \end{pmatrix}$$
$$= \begin{pmatrix} q \\ gh(S_{bx} - S_{fx}) + S_{p_{cx}} \\ gh(S_{by} - S_{fy}) + S_{p_{cy}} \end{pmatrix}. \tag{6.12}$$

Similarly to the 1D case, we apply them within a splitting scheme as source terms.

6.4 Results with Extended 2D-SWE

The Extensions in 2D have been implemented and applied to the flow problem *manhole* and *curb*.

6.4.1 Flow Problem *Manhole*

The flow problem *manhole* is cylinder-symmetric and the results are presented and compared as cuts through the 2D solution. Since no 3D-NSE solution is available, we compare the results of the classical and the extended 2D-SWE in Figure 6.13.

The impact of the included vortex region lifts the height of the water column H_c and increases the momentum and thus the Froude number Fr.

6.4.2 Flow Problem *Curb*

Figure 6.14 demonstrates the applicability of the Extensions in 2D for the flow problem *curb*. The local behavior at the curb influences the global flow behavior yielding different flow paths than in Figure 6.8. The water column is higher and larger and the velocities are also higher. Due to the extensions, the part of water flowing over the curb is increased. Thus, the flood risk for houses connected to the street is also increased.
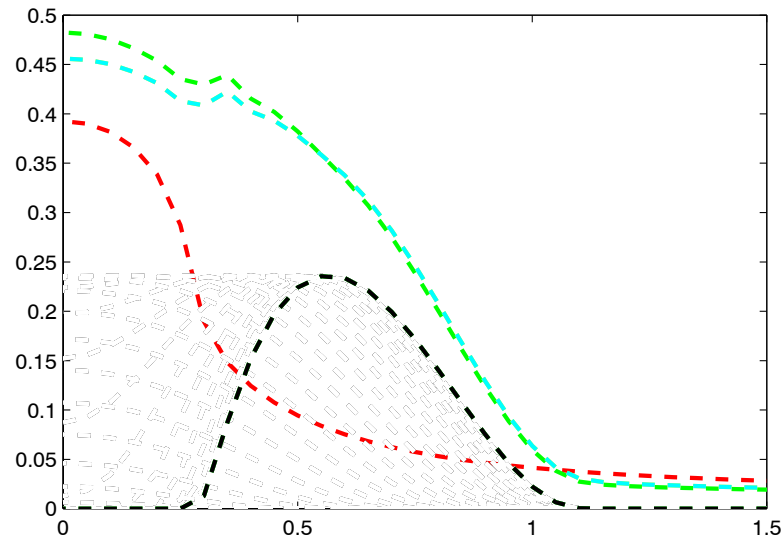
Figure 6.13: Cut through the different 2D solutions for the flow problem *man-hole*. Classical SWE (Water level H in red), SWE+Extension *Vortex Separation* (H green, s black) and SWE+Extension *Vortex Separation* +Extension *Pressure Correction* (H cyan)
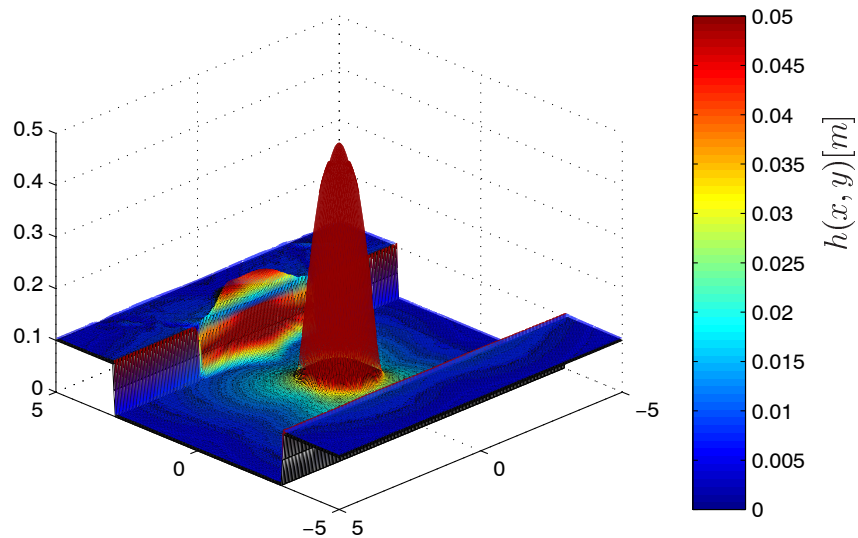

Figure 6.14: Water levels of the 2D flow problem *curb* with Extension *Vortex Separation* and Extension *Pressure Correction*

Chapter 7

Conclusions and Outlook

The accurate simulation of the outflow of water from a manhole and the flow of water over a curb is crucial for the assessment of flood risks in urban areas.

The Navier-Stokes Equations (NSE) describe the free surface flow of water accurately, but their numerical solution requires high CPU times and memory. Therefore, the approach is not applicable practically for the simulation of flood problems in urban areas.

The classical Shallow Water Equations (SWE) require only fractions (factor $< \frac{1}{100}$) of the NSE computational effort. They assume a hydrostatic pressure distribution and depth-averaged horizontal velocities but consider neither vortices in the vertical plane nor vertical velocities.

The comparison of NSE solutions and the SWE results for the special flow problems *manhole* and *curb* shows local as well as global differences. This is due to the fact, that these flow problems involve vortices in the vertical plane and vertical velocities. Thus, the classical SWE approach can not be applied reliably.

Suitable extensions of the SWE have been derived from physical considerations of the NSE flow behavior in order to increase the accuracy and thus also the reliability of the SWE results. The Extension *Vortex Separation* introduces a fluid bottom layer as a separated vortex region. This layer is considered as a dead zone and represents the bottom for the main flow above. For this main flow, vertical velocities are approximated that correct the pressure distribution entailing additional terms in the momentum equation of the SWE within the Extension *Pressure Correction*.

The differences between the NSE and the extended SWE have been decreased and more realistic pressure distributions are obtained yielding more accurate and reliable results. The increase of the computational effort due to the extensions is only moderate.

The design approach of the vortex regions has been done for stationary solutions only. In-stationary flows have been considered quasi stationary. Further attention could be spend on real in-stationary flow behavior.

The extensions of the SWE are usually restricted to the close vicinity of the manhole and the curb respectively. Assuming a further increasement of computer capacities, it would be possible to nest the NSE approach into the SWE flow at these crucial locations. For that purpose, the SWE flow and the NSE flow have to be coupled efficiently.

On the other hand, CPU capacities — even increasing over time — will be always restricted. For large scale applications of floods in parts of a big town within large systems of streets, the 2D-SWE approach requires computational effort of a size that renders it impractical to apply. Thus, there is the demand for development of simplified schemes (e.g. mass balances) applicable practically, and obtaining reliable results.

Appendix A

Mathematical and Physical Details

A.1 Notations

We work in the vector space $\mathbb{R}^3$ and points are denoted as vectors $\vec{x} = (x, y, z)^T$ or $\vec{x} = (x_1, x_2, x_3)^T$. When considering simplified problems in lower dimensions, in particular in $\mathbb{R}^1$ we write only x. Vectors are always written with the vector arrow $\vec{x}$ and tensors of 2nd order are written in bold letters, e. g. $\boldsymbol{\tau}$, $\boldsymbol{R}$, $\boldsymbol{Id}$.

The vector space is equipped with the inner product $\vec{a} \cdot \vec{b} = (a_1, a_2, a_3) \cdot (b_1, b_2, b_3)^T = a_1 b_1 + a_2 b_2 + a_3 b_3$ and the Euclidean norm $||\vec{a}|| = \sqrt{\sum_{i=1}^{3} a_i^2}$.

The vectors $\vec{a}$ and $\vec{b}$ can be multiplied to a tensor of 2nd order $(\vec{a} \otimes \vec{b}) = (a_1, a_2, a_3)^T \cdot (b_1, b_2, b_3)$ with components $(\vec{a} \otimes \vec{b})_{ij} = a_i b_j$. We avoid the summation convention and write summations always explicitly.

Assume that the scalar function $a : \Omega \to \mathbb{R}$ and the vector function $\vec{a} : \Omega \to \mathbb{R}^3$ are differentiable and describe a scalar field and a vector field.

The partial derivative of a with respect to x is denoted as $\partial a / \partial x$ and notation with subscript a_x is avoided. This notation is similar for y, z and the time t.

Remark A.1 *Letter subscripts usually give hints for the location (e. g. $w_H = w|_{z=z_H}$ or h_i for h at the inflow point i), further specification (e. g. $\vec{f}_g$ as gravitational force).*

The differential operator

$$\vec{\nabla} = \begin{pmatrix} \frac{\partial}{\partial x} \\ \frac{\partial}{\partial y} \\ \frac{\partial}{\partial z} \end{pmatrix} \tag{A.1}$$

127

operates as a gradient on the scalar field $a(\vec{x})$ denoted as

$$grad\ a = \vec{\nabla} a = \begin{pmatrix} \frac{\partial a}{\partial x} \\ \frac{\partial a}{\partial y} \\ \frac{\partial a}{\partial z} \end{pmatrix} \tag{A.2}$$

and as a divergence on the vector field $\vec{a}(\vec{x})$ denoted as

$$div\ \vec{a} = \vec{\nabla} \cdot \vec{a} = \frac{\partial a_1}{\partial x} + \frac{\partial a_2}{\partial y} + \frac{\partial a_3}{\partial z}. \tag{A.3}$$

Furthermore, we use the divergence operation not only on vectors within a mapping $\mathbb{R}^3 \times \mathbb{R}^3 \to \mathbb{R}$, but extend it to tensors of 2nd order, in particular for the stress tensor $\boldsymbol{\tau}$ within the mapping $\mathbb{R}^3 \times \mathbb{R}^{3\times3} \to \mathbb{R}^3$. Let $\boldsymbol{\tau} \in \mathbb{R}^{3\times3}$ consist of 3 row vectors $\boldsymbol{\tau} = (\vec{\tau}_1, \vec{\tau}_2, \vec{\tau}_3)$ with $\vec{\tau}_i \in \mathbb{R}^3$, then $div\ \boldsymbol{\tau} = (\vec{\nabla}\cdot\vec{\tau}_1, \vec{\nabla}\cdot\vec{\tau}_2, \vec{\nabla}\cdot\vec{\tau}_3)^T$.

The inner product of $\vec{\nabla}$ with itself is the scalar Laplace operator

$$\Delta = \vec{\nabla} \cdot \vec{\nabla} = (\frac{\partial}{\partial x})^2 + (\frac{\partial}{\partial y})^2 + (\frac{\partial}{\partial z})^2. \tag{A.4}$$

Applied to a vector, Δ has to be applied to every component of the vector, e. g. $\Delta\vec{u} = (\Delta u, \Delta v, \Delta w)^T$.

Beside this inner product, $\vec{\nabla}$ can be used in a vector product with a vector field giving the rotation of the vector field

$$rot\ \vec{a} = \vec{\nabla} \times \vec{a} = \begin{pmatrix} \frac{\partial a_3}{\partial y} - \frac{\partial a_2}{\partial z} \\ \frac{\partial a_1}{\partial z} - \frac{\partial a_3}{\partial x} \\ \frac{\partial a_2}{\partial x} - \frac{\partial a_1}{\partial y} \end{pmatrix}. \tag{A.5}$$

The fluid is considered as a continuum in an open, simply connected fluid domain $\Omega \subset \mathbb{R}^3$ with its boundary $\partial\Omega$. The fluid is moving with the velocity field $\vec{u}$ and the fluid domain is also moving with time $t \in \mathbb{R}_0^+$ and $\Omega = \Omega(t)$ and $\partial\Omega = \partial\Omega(t)$ are time-dependent.

Remark A.2 *We use Euler Coordinates, i. e. considering motion of particles observed from a fixed point and not moving with the particle. Only in Section 2.5.1 we do use the Lagrange Coordinates, since the FPM is a Lagrangian scheme.*

Definition A.3 *We denote $C^0(\mathbb{R})$ as the set of continuous real functions on $\mathbb{R}$, $C^1(\mathbb{R})$ as the set of differentiable real functions on $\mathbb{R}$ and $C_0^1(\mathbb{R})$ as the set of differentiable real functions with compact support.*

Definition A.4 *We denote a real function $f : \mathbb{R} \to \mathbb{R}$ to be smooth when f is differentiable $f \in C^1(\mathbb{R})$.*

The total or material derivative of a differentiable function $f(\vec{x}, t)$, depending on time and space coordinates of a moving water particle in the fluid domain $\Omega(t)$ is given by

$$\dot{f}(\vec{x}, t) = \frac{d}{dt} f(\vec{x}, t) = \frac{\partial}{\partial t} f(\vec{x}, t) + (grad\ f(\vec{x}, t)) \cdot \vec{u}, \qquad (A.6)$$

due to the chain rule of differentiation. $\vec{u}$ is the velocity of the fluid motion. For the material derivative of the velocity vector field $\vec{u}$, (A.6) is valid for every component u, v and w and yields the following three equations written in vector form

$$\dot{\vec{u}}(\vec{x}, t) = \frac{d}{dt} \vec{u}(\vec{x}, t) = \frac{\partial}{\partial t} \vec{u}(\vec{x}, t) + (\vec{u} \cdot grad)\, \vec{u}(\vec{x}, t). \qquad (A.7)$$

Definition A.5 (Historical Remark and Explanation) *As extension to the accentuation* Remark, *we signalize historical contents in what we call* Historical Remark. *Furthermore, an* Explanation *gives important insights and summarizes considerations.*

A.2 Mathematical Formulation of Conservation Laws

Conservation of mass, momentum and energy are the physical properties for the derivation of any set of equations describing fluid flow. The physical principle behind those laws is the assumption, or better the fact due to experience that a quantity (e. g. mass) is neither destroyed nor produced and thus conserved in the fluid domain. Since the fluid domain $\Omega(t)$ is moving with time due to the water flow we introduce the transport theorem for the mathematical description of total derivatives of fluid quantities.

Theorem A.6 (Transport theorem) *Let f be a differentiable, scalar function in the fluid domain $\Omega(t)$*

$$f : \{\cup\, \Omega(t) \times \{t\} | t \in [t_0, t_{max}]\} \to \mathbb{R},$$
$$(\vec{x}, t) \to f(\vec{x}, t)$$

and $\vec{u}$ be the smooth velocity field of the flow. Then the following holds:

$$\frac{d}{dt} \int\limits_{\Omega(t)} f(\vec{x}, t) dV = \int\limits_{\Omega(t)} \left(\frac{\partial}{\partial t} f(\vec{x}, t) + div(f(\vec{x}, t)\ \vec{u}) \right) dV \qquad (A.8)$$

Proof. e. g. [53], page 84. ∎

Remark A.7 *The divergence term in the volume integral can be transferred into a surface integral over the boundary $\partial\Omega(t)$ by applying the divergence theorem.*

In particular, we consider the 1D case of the theorem that follows directly from (A.8).

Corollary A.8 *The domain $\Omega(t)$ is an interval $I(t) = [x_1(t), x_2(t)] \subset \mathbb{R}$ varying differentiable in time with velocities $x_1'(t)$ and $x_2'(t)$. For the differentiable, scalar function $f : \{\cup I(t) \times \{t\} | t \in [t_0, t_{max}]\} \to \mathbb{R}$ the following holds*

$$\frac{d}{dt} \int\limits_{x_1(t)}^{x_2(t)} f(x,t)dx = \int\limits_{x_1(t)}^{x_2(t)} \frac{\partial}{\partial t} f(x,t)dx + f(x_2(t),t)x_2'(t) - f(x_1(t),t)x_1'(t). \quad (A.9)$$

We consider the scalar quantity $\alpha(\vec{x}, t)$ to be conserved within the fluid motion given by the velocity field $\vec{u}(\vec{x})$. Conservation of the quantity α means that the integral over any moved fluid domain $\Omega(t)$ is constant with respect to time t. Thus, we postulate the following relationship for arbitrary fluid domains $\Omega(t)$:

$$0 = \frac{d}{dt} \int\limits_{\Omega(t)} \alpha(\vec{x}, t) \, dV = \int\limits_{\Omega(t)} \left(\frac{\partial}{\partial t} \alpha(\vec{x}, t) + div(\alpha(\vec{x}, t) \, \vec{u}(\vec{x}, t)) \right) dV \quad (A.10)$$

due to the transport theorem (A.8).

Since the integral vanishes for arbitrary fluid domains $\Omega(t)$ the integrand has to be zero and we obtain:

$$\frac{\partial}{\partial t} \alpha(\vec{x}, t) + div(\alpha(\vec{x}, t) \, \vec{u}(\vec{x}, t)) = 0. \quad (A.11)$$

This equation is the standard form of a homogeneous conservation law given in differential form.

A.3 Euler Equations

As an example of a set of conservation laws we present the Euler Equations in 1D by setting the conserved quantity α from (A.11) to the density ρ, the momentum in x direction ρu and the energy E, as done in [26].

Historical Remark A.9 *Leonhard Euler (see Appendix B.1) was the first scientist who derived these equations of motion, that were long time believed to describe every fluid motion correctly and uniformly.*

For the mass conservation we set $\alpha = \rho$ and obtain in 1D:

$$\frac{\partial}{\partial t}\rho(x,t) + \frac{\partial}{\partial x}(\rho(x,t)u(x,t)) = 0 \tag{A.12}$$

(A.12) can be solved in isolation only if the velocity $u(x,t)$ is known a priori or as a function of ρ. Then ρu is a function $flux(\rho)$ and we rewrite (A.12) as

$$\frac{\partial}{\partial t}\rho + \frac{\partial}{\partial x}flux(\rho) = 0 \tag{A.13}$$

where $flux(\rho) = u\rho$ is the flux function of ρ.

The conservative principle is usually extended by introducing additional terms on the right hand side when e. g. the mass conservation is influenced by mass source terms q from inflow boundaries or when the momentum ρu is influenced by forces.

Due to Newton's second law of motion, a force f entails a change of momentum

$$\frac{d}{dt}(\rho u) = f. \tag{A.14}$$

Considering only the pressure gradient force $f = -\frac{\partial}{\partial x}p$ and including this term into the flux term $flux(\rho u)$, the conservation law for the momentum can be written as

$$\frac{\partial}{\partial t}(\rho u) + \frac{\partial}{\partial x}(\rho u^2 + p) = 0 \tag{A.15}$$

Together with the energy conservation (E: energy density, derivation in [26]) the 1D-Euler Equations read

$$\frac{\partial}{\partial t}\begin{pmatrix} \rho \\ \rho u \\ E \end{pmatrix} + \frac{\partial}{\partial x}\begin{pmatrix} \rho u \\ \rho u^2 + p \\ u(E+p) \end{pmatrix} = \vec{0} \tag{A.16}$$

Definition A.10 (Hyperbolicity) *A system of conservation laws*

$$\frac{\partial}{\partial t}\vec{u} + \frac{\partial}{\partial x}\vec{f}(\vec{u}) = \frac{\partial}{\partial t}\vec{u} + \boldsymbol{A}(\vec{u})\frac{\partial}{\partial x}\vec{u} = 0, \tag{A.17}$$
$$\vec{u}(x,0) = \vec{u}_0(x)$$

where $\vec{u}(x,t) : \mathbb{R} \times \mathbb{R} \to \mathbb{R}^m$, $\vec{f}(\vec{u}) : \mathbb{R}^m \to \mathbb{R}^m$ and $\boldsymbol{A}(\vec{u}) \in \mathbb{R}^{m\times m}$ its Jacobian matrix, is called (strictly) hyperbolic if $\boldsymbol{A}(\vec{u})$ is diagonizable with real (distinct) eigenvalues $\lambda_i(\vec{u})$ for all $\vec{u} \in \mathbb{R}^m$.

Remark A.11 *The Euler equations (A.16) are hyperbolic conservation laws.*
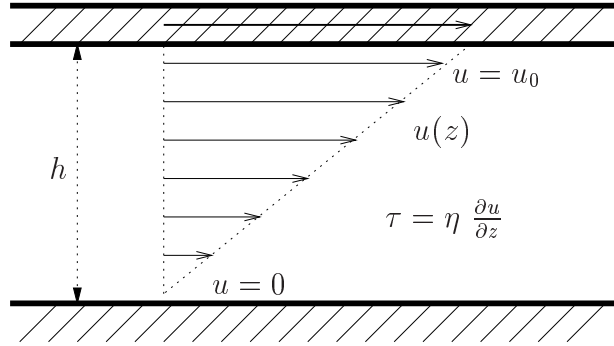
Figure A.1: Viscous friction in the Couette flow

Weak solutions

In the conservation law (A.11), the quantity α needs to be differentiable with respect to time t and to space $\vec{x}$. At times, that property of the solution is not fulfilled, e. g. in case of discontinuous initial conditions of a dam break problem. Furthermore, hyperbolic conservation laws tend to form shocks solutions $\notin C^0$ even for smooth initial conditions. We include generalized solutions with the following

Definition A.12 (weak solution) *A function $u(x,t) \in \mathcal{L}^\infty$ is called a weak solution of*

$$\frac{\partial}{\partial t} u + \frac{\partial}{\partial x} f(u) = 0 \tag{A.18}$$

if the integral of the equation multiplied with any test function $\Phi \in C_0^1$ over space and time is zero:

$$\int\limits_0^\infty \int\limits_\mathbb{R} (\frac{\partial}{\partial t} \Phi \, u + \frac{\partial}{\partial x} \Phi \, f(u)) \; dx \; dt = 0. \tag{A.19}$$

A.4   Viscous Effects

The Euler Equations (B.1) do not consider viscous effects. Due to the neglect of these terms in the equations of motion, experiments and calculations differ when viscous friction of the fluid causes loss of momentum and energy.

A well-known example for such differences is the Couette flow illustrated in Figure A.1: A panel located at the top of a fluid domain is pulled in the horizontal plane with the velocity u_0 over the fluid domain with the fluid depth h.

According to the Euler Equations (A.16), no force has to be expected to initiate the motion of water or to act against the motion of the panel. To the

contrary, experiments show a flow of water caused by the moved panel and a force of the water acting against the steady motion of the panel. This force increases with the velocity of the panel u_0 and decreases with the distance of the panels h. Furthermore the force depends on the fluid between the panels. The physical ability of a fluid to act against a motion of laminar layers is called dynamic viscosity η. Experiments yield the force against the motion per unit surface element of the panel, which is the stress τ in the horizontal direction as illustrated in Figure A.1:

$$\tau = \eta \, \frac{\partial u}{\partial z} \tag{A.20}$$

Remark A.13 *The dynamic viscosity η of water depends on its temperature. At $T = 0°C$ the viscosity is $\eta_{T=0°C} = 179.3 \cdot 10^{-5} Pa\ s$, at $T = 20°C$ we have only 55% of that value with $\eta_{T=20°C} = 100.3 \cdot 10^{-5} Pa\ s$ and at $T = 100°C$ the viscosity η is less then 20% of $\eta_{T=0°C}$. Since we do not consider temperature effects, we assume $\eta = \eta_{T=20°C}$, i. e. $\nu \approx 10^{-6} \frac{m^2}{s}$.*

For general fluid motion with the velocity field $\vec{u}(\vec{x})$ the stress is a tensor of second order.

Definition A.14 *A fluid is called a Newtonian fluid iff*

$$\boldsymbol{\tau}_{ij} = \eta \big(\frac{\partial u_i}{\partial x_j} + \frac{\partial u_j}{\partial x_i} \big). \tag{A.21}$$

Since the stress entails a viscous force $\vec{f}_V$ on the fluid motion, it has to be included in the momentum equations for the viscous NSE. The force $\vec{f}_V$ per unit mass can be evaluated as $\frac{1}{\rho} div\ \boldsymbol{\tau}$. For incompressible Newtonian fluids, this is simplified to

$$\vec{f}_V = \frac{1}{\rho} div\ \boldsymbol{\tau} = \nu \Delta \vec{u} \tag{A.22}$$

due to (A.21) with $\nu = \frac{\eta}{\rho}$ as kinematic viscosity in $\frac{m^2}{s}$.

Definition A.15 (Reynolds-number Re) *Let ν be the kinematic viscosity of the fluid, u be the typical velocity and l be the typical length scale of the flow. The ratio $Re = \frac{ul}{\nu}$ is defined as the dimensionless Reynolds-number to compare the inertia and the viscous friction forces.*

Considering the flow of water in urban areas with typical flow velocities of $u = 1m/s$ and typical water depths of $l = 0.1m$ yields a typical Reynolds-number $Re = \frac{ul}{\nu} = 10^5$. Since this number is very high, the flows are expected to be turbulent.

A.5   Ill-posed Problems

Since differentiation is an ill-posed problem, it has to be handled carefully. We repeat some background from literature [10], [29]

Definition A.16 (Hadamard) *A mathematical problem is said to be well-posed if*

$$\text{For all admissible data, a solution exists.} \tag{A.23}$$

$$\text{For all admissible data, the solution is unique.} \tag{A.24}$$

$$\text{The solution depends continuously on the data.} \tag{A.25}$$

Remark A.17 *A problem that is not well-posed is said to be ill-posed.*

(A.25) is usually the reason for the ill-posedness of problems. For those problems a classification of the ill-posedness depending on the degree of discontinuity of (A.25) exists. We refer to [10].

Appendix B

Historical Remarks

Most theoretical background for this thesis was derived already in the $19th$ century and several parts of the theory, in particular the Navier-Stokes, Euler, Saint-Venant and Reynolds equations, were named in memory of their inventors.

Some historical remarks are given within the thesis, and in this appendix portraits and some dates on those mathematicians are assembled. The sequence is based on the date of birth and has nothing to do with any kind of scientific order. Since several reports about most of those mathematicians and their lives and work are available and well-known, we omit a presentation of their biographies.

Since Adhémar Jean Claude Barré de Saint-Venant derived major theoretical background for the subjects of this thesis, his biography is briefly presented.

The information and portraits were taken from the Internet from articles by J.J. O'Connor and E.F. Robertson [36]. We thank for the permission to present the images and dates and refer to further historical remarks presented there.

B.1   Portraits and Dates

Sir Isaac Newton

Born: 4 Jan 1643 in Woolsthorpe, Lincolnshire, England
Died: 31 March 1727 in London, England

Leonhard Euler

Born: 15 April 1707 in Basel, Switzerland
Died: 18 Sept 1783 in St Petersburg, Russia

Claude Louis Marie Henri Navier

Born: 10 Feb 1785 in Dijon, France
Died: 21 Aug 1836 in Paris, France

Adhémar Jean Claude Barré de Saint-Venant

Born: 23 Aug 1797 in Villiers-en-Bire, Seine-et-Marne, France
Died: 6 Jan 1886 in St Ouen, Loir-et-Cher, France

George Gabriel Stokes

Born: 13 Aug 1819 in Skreen, County Sligo, Ireland
Died: 1 Feb 1903 in Cambridge, Cambridgeshire, England

Osborne Reynolds

Born: 23 Aug 1842 in Belfast, Ireland
Died: 21 Feb 1912 in Watchet, Somerset, England

B.2   Adhémar Jean Claude Barré de Saint-Venant

Jean Claude Saint-Venant was a student at the Ecole Polytechnique, entering the school in 1813 when he was 16 years of age. He graduated in 1816 and spent the next 27 years as a civil engineer. For the first seven of these 27 years Saint-Venant worked for the Service des Poudres et Salptres, then he spent the next 20 years working for the Service des Ponts et Chaussées.

Saint-Venant attended lectures at the College de France and the lecture notes he took in Liouville's 1839-40 class have survived. He taught mathematics at the Ecole des Ponts et Chaussées where he succeeded Coriolis.

Saint-Venant worked mainly on mechanics, elasticity, hydrostatics and hydrodynamics. Perhaps his most remarkable work was that which he published in 1843 in which he gave the correct derivation of the Navier-Stokes equations.

Seven years after Navier's death, Saint-Venant re-derived Navier's equations for a viscous flow, considering the internal viscous stresses, and eschewing completely Navier's molecular approach. That 1843 paper was the first to properly identify the coefficient of viscosity and its role as a multiplying factor for the velocity gradients in the flow. He further identified those products as viscous stresses acting within the fluid because of friction. Saint-Venant got it right and recorded it. Why his name never became associated with those equations is a mystery. Certainly it is a mishap of technical attribution.

We should remark that Stokes, like Saint-Venant, correctly derived the Navier-Stokes equations but he published the results two years after Saint-Venant.

Saint-Venant developed a vector calculus similar to that of Grassmann which he published in 1845. He then entered into a dispute with Grassmann about which of the two had thought of the ideas first. Grassmann had published his results in 1844, but Saint-Venant claimed (and there is little reason to doubt him) that he had first developed these ideas in 1832. Again it would appear that Saint-Venant was unlucky.

In the 1850s Saint-Venant derived solutions for the torsion of non-circular cylinders. He extended Navier's work on the bending of beams, publishing a full account in 1864.

In 1871 he derived the equations for non-steady flow in open channels, named the de Saint-Venant equations.

In 1868 Saint-Venant was elected to succeed Poncelet in the mechanics section of the Académie des Sciences. By this time he was 71 years old, but he continued his research and lived for a further 18 years. At age 86 he translated (with A. Flamant) Clebsch's work on elasticity into French.

Bibliography

[1] M. Abbott (1992) Computational hydraulics, Worcester: Ashgate

[2] M.B. Abd-El-Malek, S.N. Hanna (1989) Approximate solution of a flow over a ramp for large Froude numbers, Journal of Computational and Applied Mathematics, Volume 28, pp. 105-117

[3] C.J. Beffa (1994) Praktische Lösung der tiefengemittelten Flachwassergleichung. Mitteilungen der Versuchsanstalt für Wasserbau, Hydrologie und Glaziologie, ETH Zürich

[4] M. Breuer, W. Rodi (1996) Large-Eddy Simulation of Complex Turbulent Flows of Practical interest. In: Flow Simulation with High-Performance Computers II, ed. E.H. Hirschel, Notes on Numerical Fluid Mechanics, Vol. **52** pp. 258-274, Vieweg Verlag, Braunschweig

[5] I.P. Castro, J.M. Jones (1987) Studies in numerical computations of recirculating flows, International Journal for Numerical Methods in Fluids, Volume 7, pp. 793-823

[6] A.J. Chorin, J.E. Marsden (1979) A mathematical introduction into Fluid Mechanics, Springer, New York

[7] A.J. Chorin, (1968) Numerical solution of the Navier-Stokes equations, J.Math.Comput. Volume 22, pp.745-762

[8] S.C.R. Dennis and F.T. Smith (1980) Steady flow through a channel with symmetrical constriction in form of a step, Proceedings of Royal Society London, A Volume 372, pp. 393-414

[9] W. Dörfler, J. Weiss (2001) A MATLAB-code for potential equations, private communications.

[10] H.W. Engl, M. Hanke and A.Neubauer (2000) Regularization of inverse problems, Kluer Academic Publisher

[11] L. Fraccarollo, E.F. Toro (1995) Experimental and numerical assessment of the shallow-water model for the two dimensional dam break type problems. Journal of Hydraulic Research, Volume 33

[12] U. Ghia, N. Ghia and C.T. Shin (1982) High-Re Solutions for incompressible flow using the Navier-Stokes Equation and a Multigrid Method. Journal of Computational Physics, Volume 48, pp. 387-411

[13] M. Feistauer (1993) Mathematical methods in fluid dynamics, Longman Scientific and Technical, New York

[14] A. Friedman (1982) Variational Principles and free-boundary problems, John Wiley and Sons, Inc.

[15] P. Garcia-Navarro, M.E. Vazquez-Cedon (2000) On numerical treatment of water source terms in the shallow water equations, Computer and Fluids, Volume 29, pp. 951-979

[16] J.F. Gerbeau, B. Perthame (2000) Derivation of viscous Saint-Venant system for laminar shallow water; numerical validation, INRIA Rapport der recherche no. 4084

[17] M. Griebel (1995) Numerische Simulation in der Strömungsmechanik, Vieweg Braunschweig

[18] A. Haasenritter (1999) Risk Analysis for Floods by Simulation of Shallow-Water Flow. Diploma Thesis, FB Mathematik Kaiserslautern

[19] M. Hilden (1996) Vergleich numerischer Verfahren zur Simulation von Fliessgewässern am Beispiel von Elbe, Rhein und Mosel. Diploma Thesis, FB Mathematik Kaiserslautern

[20] M. Hilden, G. Steinebach (1998) ENO-discretizations in MOL- applications: some examples in river hydraulics. Applied Numerical Mathematics, Volume 28, pp. 293-308

[21] M. Hilden (2001) Estimation of flood risks in urban areas - the curb as a challenge for SWE. Mathematics in Industry 1, Progress in Industrial Mathematics at ECMI 2000, Springer, pp. 441-445

[22] A.C. King, M.I.G. Bloor (1987) Free-surface flow over a step, Journal of Fluid Mechanics, Volume 182, pp. 193-208

[23] J. Kuhnert (1999) General Smoothed Particle Hydrodynamics, Dissertation D 386 (Universität Kaiserslautern), Shaker Verlag, Aachen

[24] D. Laigle, M. Naaim (2002) Equations de Saint-Venant pour les fluides gophysiques rhologie complexe exemples d'application aux avalanches et aux coules de boue. JSMA2002, Chambery, France

[25] H. Lamb (1975) Hydrodynamics 6.th Edition, Cambridge University Press

[26] R.J. LeVeque (1992) Numerical Methods for Conservation Laws, Birkhäuser Verlag

[27] M. Lukacova-Medvidova (2001) Genuinely multidimensional evolution Galerkin schemes for the Shallow Water Equations, ENUMATH 2001, Numerical Methods and Advanced Applications, Springer

[28] A.-T. Morel (1997) A genuinely multidimensional high-resolution scheme for the Shallow Water Equations, Diss. ETH No.11959

[29] D.A. Murio (1993) The Mollification Method and the Numerical Solution of Ill-Posed Problems, Wiley Interscience

[30] B. Mohammadi, O. Pironneau (1993) Analysis of the K-epsilon Turbulence Model. Chichester: Wiley

[31] D.R. Näf (1997) Numerische Simulation von Stosswellen in Freispiegelströmungen, Mitteilungen der Versuchsanstalt für Wasserbau, Hydrologie und Glaziologie, ETH Zürich

[32] A.Q.T. Ngo (1999) Numerical Simulation of River Flow Problems based on a Finite Volume Model. Diploma Thesis, FB Mathematik Kaiserslautern

[33] K.-P. Nieschulz, J. Milina, M. Thomas, W. Schilling, T. G. Schmitt (2000) Risk Management in urban drainage systems - simulation and optimization (EUREKA Project E!2255 RISURSIM). In: Toensmann, F., Koch, M. (editors), River Flood Defence, vol. 1. Kassel Reports of Hydraulic Engineering No. 9/2000; ISBN 3-930150-20-4; pages F253-F262.

[34] A. Noussair (2001) Riemann problem with nonlinear resonance effects and well-balanced Godunov scheme for shallow fluid flow past obstacles, SIAM Journal of Numerical Analysis, Volume 39, No. 1, pp. 52-72

[35] M. Nujic (1995) Efficient implementation of non-oscillatory schemes for the computation of free-surface flows, Journal of Hydraulic Research, Volume 33, pp. 101-111

[36] J.J. O'Connor, E.F. Robertson (2002) Biographies of famous mathematicians in the www, http://www-groups.dcs.st-and.ac.uk/ history/BiogIndex.html

[37] A. Plotkin, R.W. Mei (1998) Navier-Stokes solutions for laminar incompressible flows in forward-facing step geometries AIAA Journal, Volume 24, pp. 1106-1111

[38] L. Prandtl (1942) Führer durch die Strömungslehre, Vieweg und Sohn, Braunschweig

[39] D. I. Pullin, J. K. Harvey (1997) Direct simulation calculations of the rarefied flow past a forward-facing step, AIAA Journal, Volume 15, No.1, pp. 124-126

[40] P.G. Saffman (1992) Vortex Dynamics, Cambridge University Press

[41] A.J.C.B. de Saint-Venant (1871) Theorie du mouvement non permanent des eaux, avec application aux crues des rivieres et a l'introduction des marees dans leur lit. C.R. Aca. Sc. Paris, 73, page 147-154

[42] W. Schneider (1978) Mathematische Methoden der Strömungsmechanik, Vieweg Braunschweig

[43] M. Shinbrot (1973) Lectures on Fluid Mechanics, Gordon and Breach, Science Publishers, New York

[44] F.T. Smith (1979) Journal of Fluid Mechanics, Volume 90, pp. 725

[45] G. Steinebach, A.Q.T. Ngo (2001) A method of lines flux-difference splitting finite volume approach for 1d and 2d river flow problems. Godunov methods: theory and applications, edited review, Toro, E.F. (ed.), Kluwer Academic/Plenum Publishers, 863-871

[46] D. Socolescu (2000) On the asymptotic behaviour of solutions with bounded Dirichlet integral to the steady Navier-Stokes equation, Mathematical Problems in Mechanics, C.R.Acad.Sci. Paris, t.330, Serie I, pp.427-432

[47] J.J. Stoker (1957) Water Waves, Interscience Publishers, New York

[48] S. Tiwari, J. Kuhnert (2002) A meshfree method for incompressible fluid flows with incorporated surface tension, to appear in Meshfree and Particle Based Approaches in Computational Mechanics, special issue of the European Journal of Finite Elements

[49] S. Tiwari, J. Kuhnert (2002) Particle method for simulation of free surface flows, ITWM Preprint, Kaiserslautern

[50] S. Tiwari, J. Kuhnert.(2002) Finite pointset method based on projection method for simulations of the incompressible Navier-Stokes equations. To appear in M. Griebel, M. Schweitzer (Eds.), Springer LNCSE: Meshfree Methods for Partial Differential Equations

[51] E. Toro (1999) Rieman solvers and numerical methods for fluid dynamics. Springer, Berlin, Heidelberg, 2nd edition

[52] E. Toro (2001) Shock capturing methods for free-surface flows, Wiley, Chichester

[53] E. Truckenbrodt (1992) Fluidmechanik Band 1, Springer, New York

[54] E. Truckenbrodt (1992) Fluidmechanik Band 2, Springer, New York

[55] O.R. Tutty, T.J. Pedley (1993) Oscillatory flow in a stepped channel, Journal of Fluid Mechanics, Volume 247, pp. 179-204

Curriculum Vitae

31 July 1970	Born in Bendorf
1977 - 1981	Elementary school in Niederwerth
1981 - 1990	Johannes–Gymnasium in Niederlahnstein
26 May 1990	'Abitur' (university entrance exam)
Oct. 1990 - Sep. 1996	Studies of technomathematics at the University of Kaiserslautern with subsidiary subjects technical physics and data processing
Oct. 1993 - Jan. 1994	ECMI-semester in Grenoble (France)
30 Sep. 1996	Diploma in technomathematics
09 Dec. 1997	'First Staatsexamen' for mathematics and physics to be teacher at the 'Gymnasium' (German High School)
Oct. 1996 - Sep. 1999	Scientific employee at the Federal Institute of Hydrology (BfG, Koblenz)
Apr. 1998 - Mai 1998	Research scholarship at the Center for Environmental Research (UFZ, Leipzig-Halle) awarded by the 'Deutsche Mathematiker Vereinigung (DMV)'
Jan. 2000 - Sep. 2001	PhD fellowship of the 'Fraunhofer-Institut für Techno- und Wirtschaftsmathematik (ITWM)', Kaiserslautern
Oct. 2001 - Sep. 2002	PhD fellowship of the DFG-Graduiertenkolleg "Mathematik und Praxis" at the University of Kaiserslautern
since Oct. 2002	Research employee in brake system development at the Robert Bosch GmbH

Wissenschaftlicher Werdegang

31. Juli 1970	Geboren in Bendorf
1977 - 1981	Grundschule in Niederwerth
1981 - 1990	Johannes–Gymnasium in Niederlahnstein
26. Mai 1990	Abitur
Okt. 1990 - Sep. 1996	Studium der Technomathematik an der Universität Kaiserslautern mit Nebenfächern Technische Physik und Datenverarbeitung
Okt. 1993 - Jan. 1994	ECMI-Auslandssemester in Grenoble (Frankreich)
30. Sep. 1996	Diplom in Technomathematik
09. Dez. 1997	1. Staatsexamen Mathematik und Physik für das Lehramt am Gymnasium
Okt. 1996 - Sep. 1999	Wissenschaftlicher Mitarbeiter bei der Bundesanstalt für Gewässerkunde (BfG, Koblenz)
Apr. 1998 - Mai 1998	Zweimonatiger Forschungsaufenthalt beim Umweltforschungszentrum (UFZ, Leipzig-Halle) als Preisträger der Deutschen Mathematiker Vereinigung (DMV)
Jan. 2000 - Sep. 2001	Promotionsstipendiat am Fraunhofer-Institut für Techno- und Wirtschaftsmathematik (ITWM, Kaiserslautern)
Okt. 2001 - Sep. 2002	Promotionsstipendiat im DFG-Graduiertenkolleg "Mathematik und Praxis" an der Universität Kaiserslautern
seit Okt. 2002	Mitarbeiter in der Bremssystementwicklung der Robert Bosch GmbH

Eidesstattliche Erklärung

Hiermit erkläre ich an Eides statt, dass ich die vorliegende Arbeit selbst und nur unter Verwendung der in der Arbeit genannten Hilfen und Literatur angefertigt habe.

Kaiserslautern, 06. Februar 2003